

Halogens and trace elements in subduction zones

Von der Fakultät für Biologie, Chemie and Geowissenschaften
der Universität Bayreuth

zur Erlangung der Würde eines
Doktors der Naturwissenschaften
- Dr. rer. nat. -

genehmigte Dissertation

vorgelegt von

Diego Bernini

aus Pavia (Italien)

Bayreuth, 2011

Table of contents

SUMMARY	5
ZUSAMMENFASSUNG	7
1. INTRODUCTION TO MASS TRANSFER IN SUBDUCTION ZONES	9
1.1. STRUCTURE OF SUBDUCTION ZONES	9
1.2. FLUID PRODUCTION DURING SUBDUCTION	11
1.3. FLUID MIGRATION PATHS IN SUBDUCTION ZONES	13
1.4. PHASE EQUILIBRIA OF H ₂ O-BEARING SYSTEMS AT HIGH TEMPERATURE AND PRESSURE	15
1.5. FLUID COMPOSITION IN SUBDUCTION ZONES	17
1.6. TRACE ELEMENT SIGNATURE OF SUBDUCTION FLUIDS	18
1.7. RESEARCH OBJECTIVES AND THESIS ORGANIZATION	19
1.9. REFERENCES	20
2. PARTITIONING OF HALOGENS BETWEEN MANTLE MINERALS AND AQUEOUS FLUIDS: AN EXPERIMENTAL STUDY	27
2.0. ABSTRACT	27
2.1. INTRODUCTION	28
2.2. EXPERIMENTAL METHODS	29
2.3. RESULTS	32
2.4. DISCUSSION	38
2.4.1. <i>Incorporation mechanisms of halogens in nominally anhydrous silicates</i>	38
2.4.2. <i>The Cl/H₂O ratio of arc magmas and formation of mantle brines</i>	39
2.5. CONCLUSIONS	41
2.6. REFERENCES	42
3. SOLUBILITY OF FLUORINE IN FORSTERITE TO VERY HIGH PRESSURES: A FIRST PRINCIPLES COMPUTATIONAL STUDY	47
3.0. ABSTRACT	47
3.1. INTRODUCTION	48
3.2. CRYSTAL CHEMISTRY OF FLUORINE-BEARING MAGNESIUM SILICATES	48
3.3. COMPUTATIONAL METHOD	50
3.3. RESULTS	52
3.3.1. <i>Pressure-volume relations at static conditions</i>	52
3.3.2. <i>Internal energy and enthalpy at static conditions</i>	55
3.3.3. <i>Thermodynamic mixing properties</i>	56
3.4. DISCUSSION	57
3.4.1. <i>Comparison of the GGA and LDA results</i>	57
3.4.2. <i>Comparison of the pressure-volume properties with experimental results</i>	58
3.4.3. <i>Fluorine solubility in forsterite</i>	58

3.4.4. <i>Geochemical implications</i>	61
3.5. REFERENCES	62
3.6. APPENDIX	66
4. ZIRCON SOLUBILITY IN AQUEOUS FLUIDS AT HIGH TEMPERATURES AND PRESSURES	71
4.0. ABSTRACT	71
4.1. INTRODUCTION	71
4.2. EXPERIMENTAL METHODOLOGY	72
4.3. RESULTS	76
4.4. DISCUSSION	79
4.4.1. <i>Evidence for attainment of equilibrium</i>	79
4.4.2. <i>Thermodynamic model for zircon solubility</i>	80
4.4.3. <i>Effect of additional solute components</i>	81
4.4.5. <i>Comparison with other HFSE</i>	83
4.4.6. <i>Origin of the negative Zr anomalies in arc magmas</i>	84
4.5. CONCLUSIONS.....	87
4.6. REFERENCES	89
5. GENERAL CONCLUSIONS	95
ACKNOWLEDGEMENTS	99

Summary

This thesis concentrates on solubilities and incorporation mechanisms of halogens and trace elements in minerals and aqueous fluids at high temperatures and pressures.

The solubility of fluorine and chlorine in upper mantle minerals (forsterite, enstatite and pyrope) and halogen partitioning between aqueous fluids and these minerals were investigated by piston-cylinder experiments at 1100 °C and 2.6 GPa. Chlorine solubility in forsterite, enstatite and pyrope is below the ppm level, and it is independent of fluid salinity. The fluid-mineral partition coefficient of chlorine is 10^3 - 10^6 , indicating extreme incompatibility of chlorine in nominally anhydrous silicates. The fluorine solubility in enstatite and pyrope is two orders of magnitude higher than for Cl, with no dependence on fluid salinity. Forsterite dissolves 246-267 ppm up to a fluid salinity of 1.6 wt. % F. At higher fluorine contents in the system, forsterite is replaced by the minerals of the humite group, which host fluorine in the hydroxyl site. The fluid-mineral partition coefficient of fluorine ranges from 10^1 to 10^3 . Due to the extreme incompatibility of Cl in a peridotite mineral assemblage, fluid flow from a subducting slab through the mantle wedge will lead to more efficient sequestration of H₂O (when compared to Cl) into minerals, thus inducing a gradual increase in the fluid salinity. Mass balance calculations reveal that rock-fluid ratios of $(1.3-4) \times 10^3$ are required to produce the characteristic Cl/H₂O signature of primitive arc magmas. This indicates that fluid flow from subducting slabs into the melting regions in the overlying mantle is not confined to narrow channels but it is sufficient to pervasively metasomatize the bulk wedge.

Energetics of fluorine incorporation in forsterite and forsterite-humite chemical equilibria were explored in the system Mg₂SiO₄-MgF₂ by first principles computations. The pressure-volume equations of state and ground-state energies were determined for orthorhombic Mg₂SiO₄-Mg₂F₄ solutions, fluorine-bearing end-members of the humite group, and sellaite (MgF₂). Humite group minerals and sellaite are energetically more stable than their equivalent solid solution compounds, hence they can act as buffers of fluorine solubility in forsterite. Compressibility increases systematically with the F content for both solid solution compounds and stable minerals. Nevertheless, end member solids are systematically less compressible than the respective solid solution compounds. The pressure-volume equations of state, internal energies, configurational and excess properties were used to set up a thermodynamic model of fluorine solubility in forsterite buffered by humite-group minerals up to 1900 K and 12 GPa. Humite is the stable F buffer in the investigated pressure and temperature range. The fluorine solubility in forsterite increases with temperature, from 0.01 ppm F at 500 K up to 0.33 wt. % F at 1900 K and 0 GPa.

By contrast, the effect of pressure on the fluorine solubility is small, leading to its minor decrease as pressure rises to 12 GPa. These results demonstrate that partition coefficients of fluorine between forsterite and aqueous fluid (or silicate melt) are expected to increase with increasing temperature and decreasing pressure. When fluids or melts pass through the mantle wedge, fluorine will most efficiently be stored in the high-temperature portions of the wedge, promoting mantle metasomatism beneath the arc, and it will be released when the metasomatized mantle is advected to colder regions or to higher pressures.

The mobility of high field strength elements in aqueous fluids in subduction zones was addressed by in-situ zircon solubility measurements in a hydrothermal diamond anvil cell. The zircon solubilities in aqueous fluids at 865-1025 °C and 6-20 kbar buffered by quartz are very low, ranging from 1.0 to 3.3 ppm Zr, and solubilities weakly increase with temperature and pressure.

Experimental results were fitted to a density model: $\log c = 3.45 - \frac{3803}{T} + 1.52 \log \rho$, where c is the Zr concentration in the fluid (ppm), T is temperature (K) and ρ is the fluid density (g cm^{-3}). Additional experiments have shown that Zr solubility increases with a decrease in silica activity and with the presence of NaCl and albite due to Zr-Cl or alkali-Zr complexing but it still remains very low. Therefore, the low Zr content observed in arc magmas is due to a very low mobility of Zr in aqueous fluid.

Zusammenfassung

Diese Dissertation befasst sich mit Löslichkeit und Aufnahme von Halogenen und Spurenelementen in Mineralen und Fluiden unter hohen Temperaturen und Drücken.

Durch Stempel-Zylinder-Experimente bei einer Temperatur von 1100 °C und einem Druck von 2,6 GPa wurden die Löslichkeit von Fluor und Chlor in Mineralen des oberen Mantels (Forsterit, Enstatit und Pyrop) und die Verteilung von Halogenen zwischen diesen Mineralen und wässrigen Fluiden studiert. Die Chlorklöslichkeit in Forsterit, Enstatit und Pyrop liegt unterhalb der ppm-Grenze und ist vom Salzgehalt des Fluids unabhängig. Der Fluid-Mineral-Verteilungskoeffizient von Chlor beträgt 10^3 - 10^6 , was eine extreme Inkompatibilität von Chlor in wasserfreien Silikaten anzeigt. Die Fluorlöslichkeit in Enstatit und Pyrop ist zwei Größenordnungen größer als jene von Cl und zeigt ebenfalls keine Abhängigkeit vom Salzgehalt des Fluids. Forsterit löst 246-267 ppm F bei einem Gehalt 1,6 wt. % F im Fluid. Bei höheren Fluor-Gehalten wird Forsterit von Mineralen der Humit-Gruppe ersetzt, die Fluor in den Hydroxyl-Gitterplätzen einbauen. Der Fluid-Mineral-Verteilungskoeffizient von Fluor beträgt 10^1 bis 10^3 . Wegen der extremen Inkompatibilität von Cl in Mineralen des oberen Mantels verlieren Fluide bei der Perkolatation von der subduzierten Platte durch den Mantelkeil praktisch kein Cl, während gleichzeitig Wasser durch Einbau in nominal wasserfreie Minerale verloren geht. Dies führt zu einer Erhöhung der Salinität, d.h. des Cl/H₂O-Verhältnisses. Massenbilanz-Berechnungen ergeben, dass Gesteins-Fluid-Verhältnisse von $(1.3-4) \cdot 10^3$ nötig sind, um die charakteristische Cl/H₂O-Signatur primitiver Inselbogen-Magmen zu produzieren. Dies wiederum bedeutet, dass Fluide nicht nur entlang von isolierten Kanälen aus einer subduzierten Platte in die Zone der Schmelzbildung wandern, sondern dass das Fluid durch große Volumina von Gestein diffundiert und chemisches Gleichgewicht mit diesem Nebengestein erreicht wird.

Die Energetik des Fluor-Einbaus in Forsterit sowie Gleichgewichte zwischen Forsterit und Humit wurden im System Mg₂SiO₄-MgF₂ mit Hilfe von ab-initio-Berechnungen untersucht. Die Zustandsgleichungen und Energien des Grundzustandes wurden für orthorhombische Mg₂SiO₄-Mg₂F₄-Mischkristalle, Fluor-haltige Endglieder der Humit-Gruppe und für Sellait (MgF₂) ermittelt. Minerale der Humit-Gruppe und Sellait sind energetisch stabiler als ihre entsprechenden Mischkristalle. Somit stellen sie den stabilen F-Puffer für Forsterit dar. Die Kompressibilität steigt systematisch mit dem F-Gehalt sowohl für die Mischkristalle als auch für die stabilen Minerale. Trotzdem sind die reinen Minerale systematisch weniger kompressibel als ihre entsprechenden Mischkristalle. Die Zustandsgleichungen, internen Energien, konfigurationelle und Exzess-Eigenschaften wurden verwendet, um ein thermodynamisches Modell der

Fluorlöslichkeit in Forsterit bei Bedingungen bis zu 1900 K und 12 GPa zu erstellen, wobei die Löslichkeit durch Minerale der Humit-Gruppe gepuffert wird. Die Fluorlöslichkeit in Forsterit nimmt mit der Temperatur von 0,01 ppm F bei 500 K bis zu 0,33 Gew. % F bei 1900 K und 0 GPa zu. Im Gegensatz dazu sinkt die Löslichkeit bei einer Druckerhöhung bis 12 GPa. Im untersuchten Druck-Temperatur-Bereich stellt Humit einen stabilen Puffer für F dar. Diese Ergebnisse zeigen, dass der Fluor-Verteilungskoeffizient zwischen Forsterit und einem wässrigen Fluid (oder einer silikatischen Schmelze) mit steigender Temperatur und sinkendem Druck zunimmt. Bei Fluiden, die durch den Mantelkeil migrieren, wird Fluor am effektivsten in den Hochtemperatur-Regionen des Keils gespeichert, wodurch eine Metasomatose des Mantels unter dem Inselbogen begünstigt wird. Fluor wird allerdings erst frei gesetzt, wenn der metasomatisch veränderte Mantel entweder in kältere Bereiche oder zu höheren Drücken hin transportiert wird.

Die Mobilität von HFSE-Elementen in wässrigen Fluiden in Subduktionszonen wurde durch in-situ Messungen der Zirkonlöslichkeit in hydrothermalen Diamantstempelzellen ermittelt. Die Löslichkeit von durch Quarz gepuffertem Zirkon bei 865-1025 °C und 6-20 kbar sind mit 1,0 bis 3,3 ppm Zr sehr gering und nehmen mit steigender Temperatur und Druck nur schwach zu. Die Ergebnisse aus den Experimenten wurden durch ein Dichte-Modell beschrieben:

$$\log c = 3.45 - \frac{3803}{T} + 1.52 \log \rho,$$

wobei c die Zr-Konzentration im Fluid (in ppm), T die

Temperatur (K) und ρ die Fluidichte (g cm^{-3}) ist. Weitere Experimente zeigen, dass die Zirkonlöslichkeit mit dem Abnehmen der Aktivität von Kieselsäure und durch die Präsenz von NaCl und Albit wegen der Komplexbildung von Zirkonium mit Chlor oder Alkalien zunimmt, aber trotzdem ziemlich gering bleibt. Folglich ist der geringe Zr-Gehalt in Inselbogen-Magmen auf die sehr geringe Mobilität von Zr in wässrigen Fluiden zurückzuführen.

1. Introduction to mass transfer in subduction zones

1.1. Structure of subduction zones

Convergent plate boundaries are major planetary sites of mass transfer between fluids, silicate magmas and minerals. Based on the type of converging Earth's crust, they are divided into three types: (1) ocean-ocean convergence marked by an island arc, (2) ocean-continent convergence along active continental margins, and (3) continent-continent collision. Island arcs and active continental margins are sites of magmatic activity, which provides important information on geochemical cycle and melting related to subduction.

The subducting slab, which descends into the mantle below island arcs and active continental margins consists of three main parts: (1) oceanic sediments, (2) oceanic crust composed of sea floor basalts, mafic sheeted dikes, gabbros and cumulates, and (3) mantle peridotites, predominantly harzburgites, variably depleted by previous partial melting (Fig. 1-1).

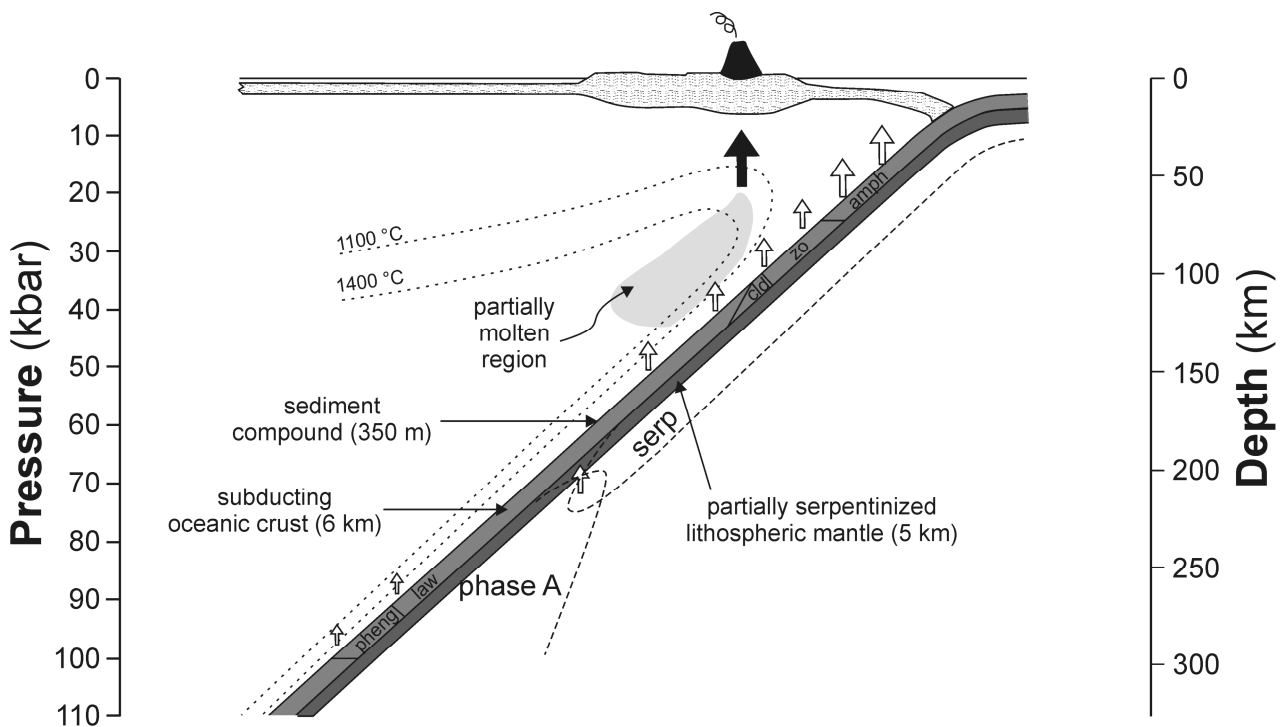


Fig. 1-1. Schematic section of a subduction zone (redrawn and modified from Schmidt and Poli 1998). Stippled lines outline stability fields of hydrous phases in peridotite; dashed lines represents mantle wedge isotherms. Dehydration of oceanic crust and serpentinized peridotite occurs down to a depth of ca. 150-200 km, thus fluids will generally be available above the subducting lithosphere. The light grey region in the mantle wedge will have a significant amount of melt present, produced by fluid-saturated melting. The volcanic front forms where the amount of melt is sufficient to be mechanically extracted and to give rise to arc magmatism. Open arrows indicate rise of fluid, solid arrows mark ascent of melts. Mineral abbreviations are amph - amphibole, cld - chloritoid, law - lawsonite, pheng - phengite, serp - serpentine, and zo - zoisite.

Subduction of the oceanic lithosphere corresponds to a prograde metamorphic path caused by heat conduction from the mantle. Prograde metamorphic reactions occurring in sediment, hydrated oceanic crust and serpentized peridotite are mainly dehydration and decarbonation reactions and progressively lead to anhydrous eclogite and peridotite assemblages. In Fig. 1-1 it is assumed that peridotitic lithosphere will be colder than 600 °C at 6 GPa, therefore serpentine will break down to phase A and aqueous fluid; thus a part of H₂O is released, while the remainder can be subducted to greater depth. In the oceanic crust, temperatures are usually low enough to stabilize lawsonite and phengite to their maximum stability pressure. For very young and hot slabs, dehydration reactions may intersect melting reactions, thus leading to the melting of slab lithologies, or the free fluid phase may escape and pervade the overlying mantle (*cf.* Schmidt and Poli 1998, Hack et al. 2007a,b). Early petrogenetic models advocated partial melting of the subducted slab as source of andesitic magma rising through the mantle wedge (Green and Ringwood 1968, Marsh and Carmichael 1974). Such a process was mainly active in the Earth's early history and the resulting magmas have an adakitic signature, characterized by high La/Yb and high Sr/Y (Kay 1978, Guo et al. 2009, Karsli et al. 2010). In most modern subduction zones, aqueous fluid is released from the slab at subsolidus temperatures and/or supercritical pressures, and it induces hydration and/or partial melting of the peridotitic mantle wedge. As a consequence, magmas generated by hydrous wedge melting will have a significant imprint from both the mantle and the slab components.

Magmas generated in volcanic arc and active continental margins have a calc-alkaline composition. Trace element abundances in primitive oceanic island-arc basalts can be conveniently compared with those of N-type mid-ocean ridge basalts (N-MORB), which represent direct products of partial melting beneath the mid-ocean ridges. The arc basalts are characterized by selective enrichment of incompatible elements of low ionic potential (Sr, K, Rb, Ba) and depletion of elements of high ionic potential (Ta, Nb, Ce, Zr, Hf, Ti, Y) relative to N-type MORBs (Fig. 1-2). The trace element pattern of arc lavas may be interpreted as a composite record of mantle, shallow and deep fluid components (Pearce and Stern 2006; Fig 1-2).

The mantle component has concentrations similar to those of MORB and can be reconstructed by considering elements which are rather immobile in subduction fluids (Nb, Ta, Zr, Hf, Ti, HREE). The second component contains all elements, which may be mobilized in the supercritical fluids or slab melts at high temperatures (Rb, Ba, Sr, K, Th, U, light and middle REE, P, Pb), whereas the selective enrichment in mono- and divalent cations (Rb, Ba, K, Sr, Pb) indicates elements strongly soluble in aqueous fluids at low temperatures (Pearce and Stern 2006).

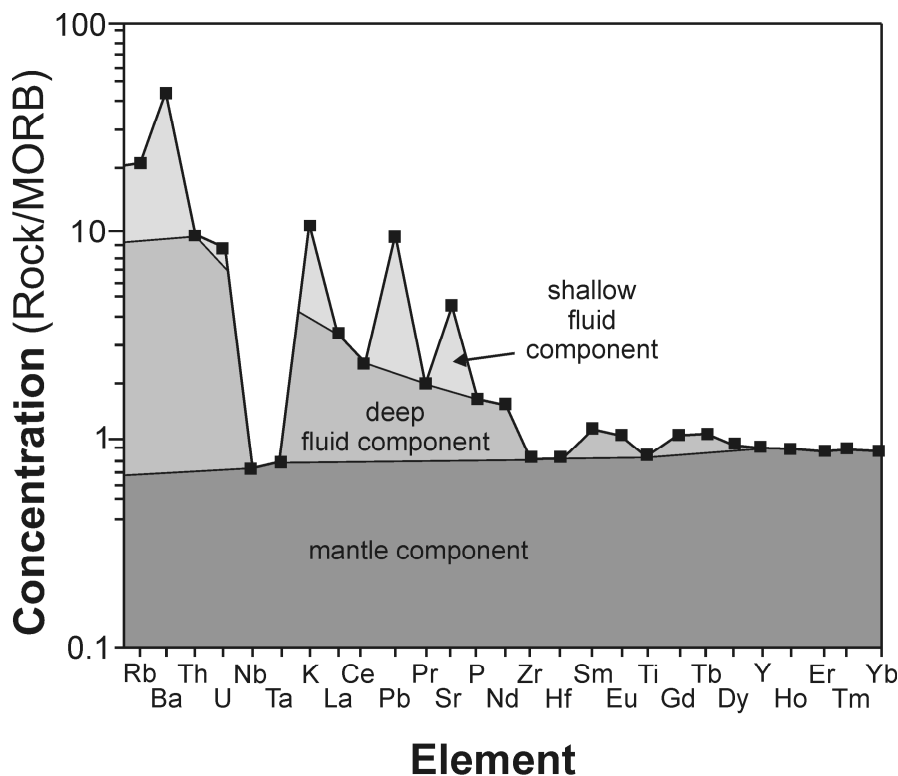


Fig. 1-2. Trace element pattern of arc magmas (modified from Pearce and Stern 2006). This geochemical pattern can be used to highlight the different contributions of mantle, and the deep and shallow subduction fluids (see text for explanation).

However, the interpretation shown in Fig. 1-2 is at best approximately correct, since the solubilities and the partitioning behavior of various trace elements between fluids and minerals are only incompletely known and the systematics of the variation of solubilities with pressure, temperature and fluid composition has hardly been explored. Moreover, early experimental studies suggested that the depletion of elements such as Nb and Ta is a fingerprint of rutile being a stable residual phase in the subducting slab (Brenan et al. 1994, 1995a, b), while more recent work suggest that these elements are inherently immobile in aqueous fluids (Audétat and Keppler 2005, Baier et al. 2008). In more general terms, it is uncertain to what extent the composition of subduction zone fluids is controlled by equilibrium with accessory minerals, such as rutile or zircon, or by equilibrium with ordinary silicates. Another poorly constrained variable is the relative magnitude of the contribution of the subducted slab and of leaching from the mantle wedge above the slab to the trace element budget of arc magmas.

1.2. Fluid production during subduction

During plate convergence, substantial quantities of free or structural water are subducted into the Earth's interior. The total flux of structurally bound water into subduction zones amounts

to $\sim 37 \cdot 10^{18}$ mol H₂O My⁻¹; a major portion ($\sim 20 \cdot 10^{18}$ mol H₂O My⁻¹) is generated by sea floor alteration of oceanic crust at low to moderate temperature (Wallmann 2001).

The dehydration of the subducting slab is a stepwise process but the sliding nature and the overlap of dehydration reactions tends to eliminate sharp dehydration fronts (Schmidt and Poli 1998, Rüpke et al. 2004). First, pore water is release from sediments and altered oceanic crust by compaction at shallow depths (< 20 km). Second, fluids is released from sediments and oceanic crust over the depth interval of 20-100 km, when most of the hydrous phases (e.g., chlorite, talc, amphibole) become unstable. Third, deep fluids (> 100 km) are generated by breakdown of serpentine in the hydrated lithospheric mantle (Fig. 1-1). When dense hydrous magnesium silicates such as phase A become stable, portion of H₂O may be subducted to deeper Earth's interior (Kawamoto 2006).

In detail, oceanic sediments contain pore saline sea water in addition to structurally bound water in clay minerals and other phases. Plank and Langmuir (1998) estimate the average water content of oceanic sediments to be around 7 wt. %. Consequently, the total H₂O budget in a column of sediments 350 m thick is $1.7 \cdot 10^5$ kg·m⁻³ (Rüpke et al. 2004). At a depth of ~50 km sediments have already lost more than 50 % H₂O and by ~100 km they contain *ca.* 25 % of their initial H₂O content. The dehydration of sediments is also promoted by temperature, which is higher at the slab surface than in its interior (Pasquale *et al.* 2005, van Keken *et al.* 2002).

The water content of oceanic crust is generally elevated by seafloor hydrothermal processes. The H₂O concentration in the uppermost oceanic crust (altered basalts) is estimated to range between 1.3 and 2.8 wt. %, whereas in the deep oceanic crust (altered gabbros) it is between 0.2 and 1.5 and 0.2 wt. % (Staudigel et al. 1989, Kerrick and Connolly 2001, Rüpke et al. 2004). This variation is a combined results of the degree of alteration and its temperature (Ito et al. 1983, Wallmann 2001). Assuming that the first kilometer of the subducted crustal column is strongly altered and contains 2.7 wt. % H₂O, the underlying less hydrated 2-km-thick layer contains 1 wt. % H₂O, and the gabbroic portions is not hydrated, the amount of water stored is 2.83 kg·m⁻³.

Most of the water budget of the oceanic crust (~92 %) is lost at depth between ~100 and 200 km. The water is produced by breakdown of chlorite, glaucophane and epidote. Their dehydration reactions occur near 550 °C, whereas the only phase, which is stable to much higher temperatures and pressures (up to 800 °C and 7 GPa), is lawsonite. This mineral controls the deep release of water from the oceanic crust and the sediments (Schmidt and Poli 1998, Rüpke et al. 2004, Kerrick and Connolly 2001).

The degree of hydration of the lithospheric mantle below the oceanic crust is not well constrained. In addition to hydration by sea floor hydrothermal activity, brittle fracturing and faulting at the trench bend provides pathways for deep water infiltration (Schmidt and Poli 1998, Ranero et al. 2003). There are, however, no reliable estimates of the distribution and abundance of favorable hydration sites locations or the degree of mantle serpentinization. Reduction of seismic P-wave velocities has been observed and interpreted as qualitative indication of mantle serpentinization (Berhorst et al. 2003, Sallares and Ranero 2003). Serpentinized lithospheric mantle releases aqueous fluid at depth from 120 to 200 km (Rüpke et al. 2004), when it intersects the upper stability limit of serpentine at *ca.* 600 °C (Rüpke et al. 2004). The only plausible candidate for subduction of H₂O to the Earth's deeper interior is the phase A. Nevertheless there might be a gap between the occurrence of phase-A and the breakdown of serpentine. The intersection of the stability fields of serpentine and phase-A occurs at 600 °C and 6.0 GPa (Rüpke et al. 2004). For an old and cold plate, the stability field of serpentine is extended to higher pressure and may overlap with that of phase-A. In this way, serpentine dehydrates only partially to form the phase-A and the chemically bound water becomes subducted to the deeper mantle (Schmidt and Poli 1998, Rüpke et al. 2004, Kawamoto 2006).

The outflux of water from magmatic arc to the atmosphere is estimated to be $\sim 22.5 \cdot 10^{18}$ mol H₂O My⁻¹; the greatest contribution ($\sim 20 \cdot 10^{18}$ mol H₂O My⁻¹) comes from the subducting slab, whereas mantle degassing is of minor importance ($\sim 2.5 \cdot 10^{18}$ mol H₂O My⁻¹). By contrast, *ca.* $17 \cdot 10^{18}$ mol H₂O My⁻¹ are not released into the arc region but are subducted into the mantle (Wallmann, 2001).

1.3. Fluid migration paths in subduction zones

Once produced, the aqueous-carbonic fluids have low density, thus are extremely buoyant and immediately move upwards to the mantle wedge. During convergent motion, the slab and overlying mantle become mechanically coupled (corner flow), causing overlying mantle material to be dragged down. This mechanism continuously provides a fresh supply of volatile-poor mantle for the uptake of rising fluid (Manning 2004). Despite the efficiency of this process some slab derived fluid may travel great distances before reacting out (Mastsumoto et al., 2003). Slab-derived fluids migrate along temperature-pressure paths that are rather unusual for geodynamic processes (Fig. 1-3).

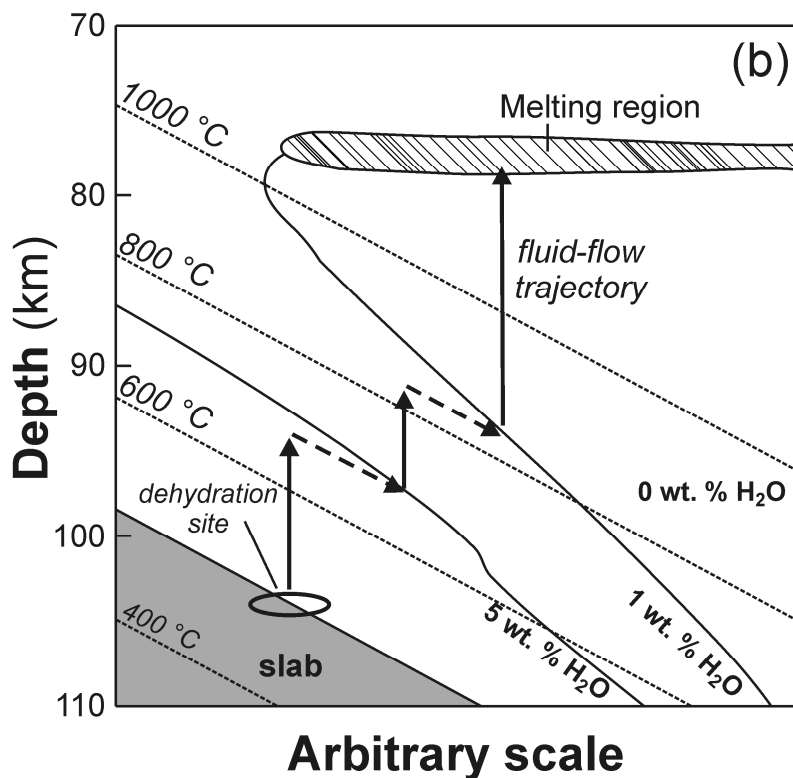
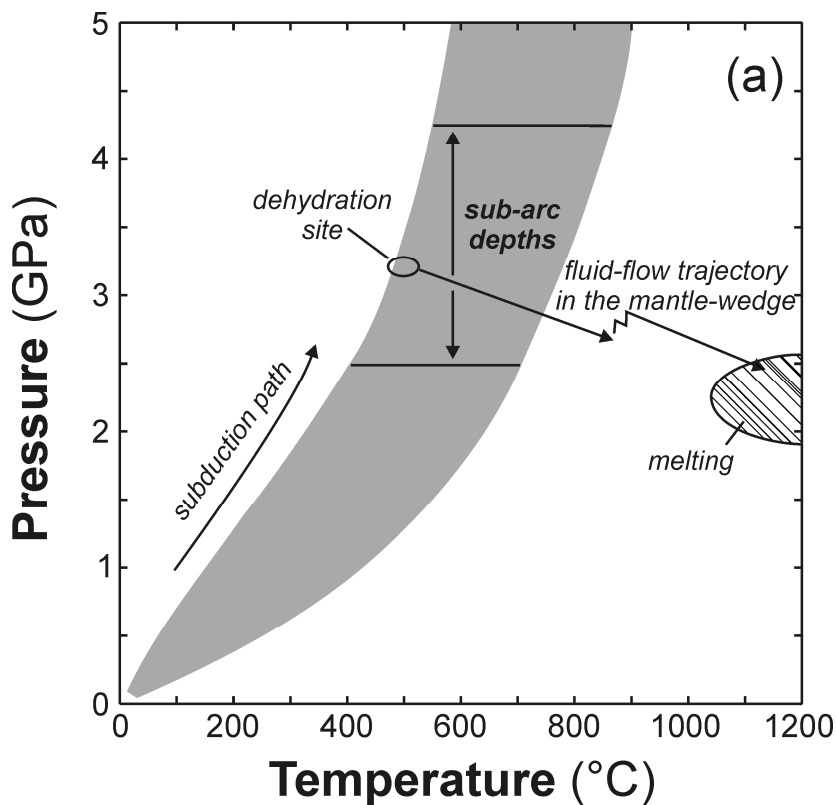


Fig. 1-3. Fluid flow trajectory in a subduction zone (modified from Manning 2004): (a) pressure-temperature diagram showing a range of representative geotherms at the slab-mantle interface (in gray), illustrated by the northwestern and southeastern Japanese arcs (Peacock and Wang 1999); the coolest geotherm is in agreement with lawamori (1998); (b) flow path of a slab-derived fluid, with isopleths of the H₂O concentration in the mantle (wt. % H₂O, solid curves). Isotherms are indicated by dashed curves. The fluid migrates into the mantle wedge (solid arrows). After multiple dehydration steps, the fluid enters a region where it is in equilibrium with anhydrous minerals, which allows for greater migration distances.

The fluid path illustrated involves a temperature increase from ~500 °C at 3.2 GPa (~100 km depth), to ~1150 °C at 2.4 GPa (~ 80 km depth) (Iawamori 1998, Peacock and Wang 1999, Manning 2004). The increase by 650 °C over ~20 km, that is, 32.5 °C km⁻¹, probably represents a maximum gradient attainable because the model refers to a cold subducting slab. Water density in subduction zone fluids ranges from 1.4 g cm⁻³ at sub-arc conditions (~500 °C and 3.2 GPa) to 1.0 g cm⁻³ at the thermal maximum of the mantle wedge (~1150 °C and 2.4 GPa) (Wiryana et al. 1998, Withers et al. 2000, Wagner and Pruss 2002, Churakov and Gottschalk 2003, Abramson and Brown 2004, Manning 2004). With increasing temperature, the short-range-ordered, tetrahedral packing of H₂O molecules become progressively disordered, and dissociation of neutral species and ion complexes increases (Marshall and Franck 1981).

Fluid flow in the mantle wedge may involve pervasive distributed flow, channeled flow, or a combination of both (Davies 1999, Dobson et al. 2002, Hacker et al. 2003, Mibe et al. 2002). Because of the interaction of fluid with the surrounding rocks while approaching equilibrium, the flow regime has different effects on the evolution of the fluid chemical composition. The effective rock-to-fluid ratio is significantly lower in the channelized flow regime, and its chemistry, when reaching the partially molten region of the mantle wedge, is much less changed from its initial state. Quantifying the flow regime is essential for constraining the relative contributions of the subducted slab and of scavenging of trace elements from the mantle wedge to the trace element budget of arc magmas. Time scales of UóThóRa disequilibria in arc magmas and plausible distances of fluid flow imply flow rates between 2.5 and 100 m yr⁻¹, which is consistent with both channelized and pervasive flow (Yokoyama et al. 2002, Mastsumoto et al. 2003).

1.4. Phase equilibria of H₂O-bearing systems at high temperature and pressure

Interpretation of subduction zone fluids and their role in melt generation fundamentally depends on the mineral-melt-fluid equilibria and critical phenomena between fluids and melts at elevated temperatures and pressures (Stalder and Ulmer 2001, Kessel et al. 2005, Hack et al. 2007a). Two-component mineral-H₂O systems of geological interest exhibit two distinct types of behavior depending on the relationship between the critical and vapor-pressure curves in the pressure-temperature space (Hack et al. 2007a; Fig. 1-4). Intersection of these two curves, which is common among silicate-H₂O binary system, produces two critical end-points. The lower critical end-point is located close to the critical point of H₂O (374 °C and 221 bar). The solubility of silicates in aqueous vapor at these conditions is very low and it usually exhibits retrograde behavior with respect to temperature. The second upper critical end-point represents termination

of the fluid- saturated silicate solidus. In the system $\text{SiO}_2\text{-H}_2\text{O}$, this occurs at 1100 °C and 0.97 GPa (Kennedy *et al.* 1962). As the upper critical end-point is approached, the silicate solubility in aqueous fluid dramatically increases until complete fluid-melt miscibility occurs. The critical curves are located at 550-1000 °C and 0.3-2.2 GPa for felsic to intermediate silicate- H_2O systems (Bureau and Keppler 1999). Other volatiles such as F and B, or excess Na shift the critical curve to significantly lower temperature (Sowerby and Keppler 2002). Supercritical fluids are reported to occur above 800 °C at 6 GPa in basaltic system (Kessel *et al.* 2005).

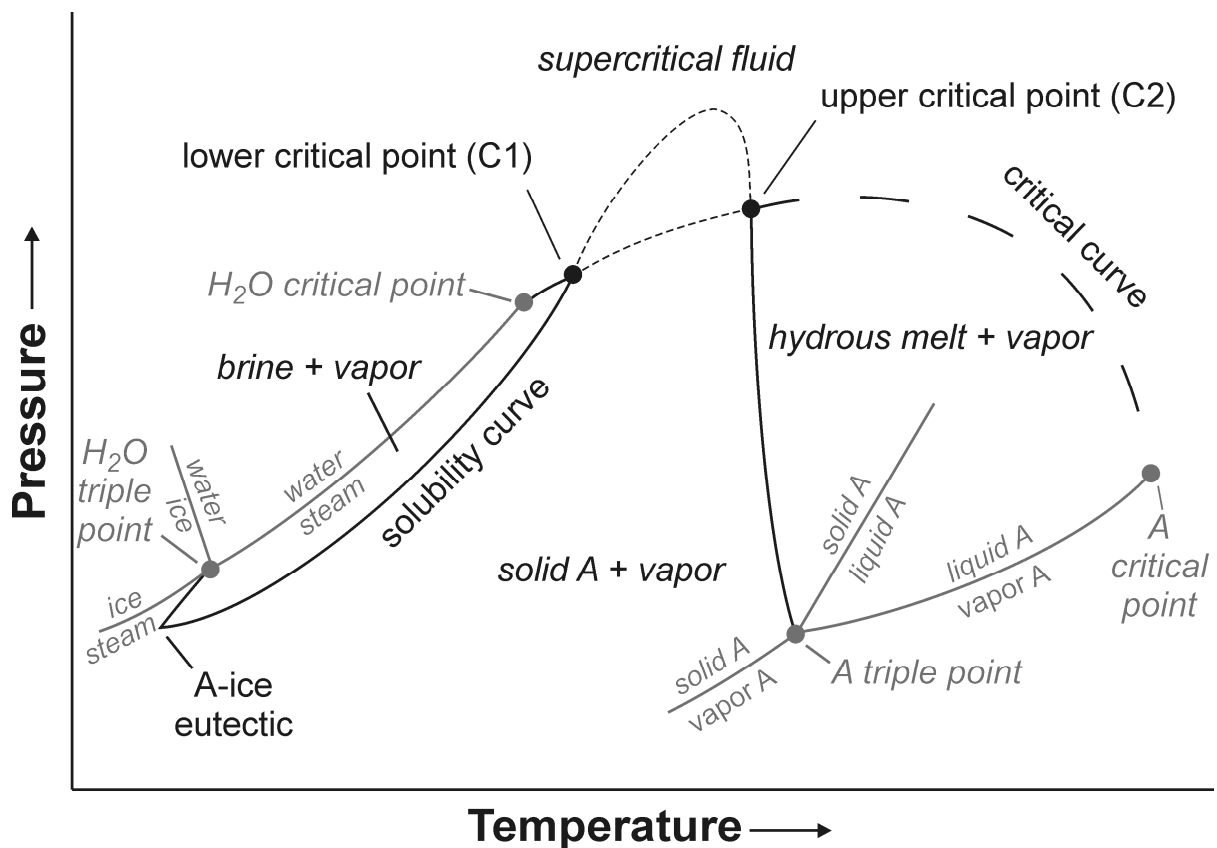


Fig. 1-4. Pressure vs. temperature projection of phase relations in a two component H_2O -A system (modified from Manning 2004). Grey curves indicate phase relations for one-component systems H_2O and a hypothetical substance A; black curves represent relations for A- H_2O mixtures. Labeling of all fields is for a H_2O -rich composition. Short dashed lines denote metastable portions of curves.

The pressure-temperature conditions of fluid-saturated solids for representative rock compositions were compiled by Hack *et al.* (2007b) and they indicate that geothermal gradients of young and hot slabs intersect the metasediment and metabasalt solids at 670-700 °C and 1.0-2.5 GPa, whereas geotherms of old and cold slabs are likely to pass through conditions exceeding those of the second critical end-point. In the latter case, fluids produced by dehydration reactions become progressively solute-rich. During ascent through the mantle wedge, that is, heating and

decompression, the fluids coexisting with surrounding solids will continuously evolve to H₂O-rich silicate melts.

1.5. Fluid composition in subduction zones

The physico-chemical properties of water, in particular the dielectric constant, dictate mineral solubility and aqueous speciation (Dolej– and Manning, 2010). Mineral solubilities are further enhanced by the presence of other ligands or aluminosilicate solutes (Manning 2004). This picture becomes more complex when supercritical fluids become solute-rich or even continuously evolve to hydrous melts. Solute structure changes from hydrated ions or ion pairs through small polymer clusters to the interconnected network of a hydrous silicate liquid (Mysen 1998, Zotov and Keppler 2000, Newton and Manning 2009). *In situ* spectroscopic studies and non-Henrian behavior of aqueous solutes both reveal that silica polymerization is significant at subduction-zone conditions (Zhang and Frantz 2000, Zotov and Keppler 2000, 2002, Newton and Manning 2002, 2003). Aluminosilicate-bearing fluids play a crucial role in promoting solubilities of high field strength elements such as Ti (Audéat and Keppler 2005, Manning 2007, Antignano and Manning 2008).

Samples of fluids produced by slab devolatilization are limited to shallow subduction and are available from Costa Rica and Izu-Bonin convergent margins (Fryer et al. 1990, Kimura 1997). In the former location these fluids were sourced at 10-15 km depth, with a temperature from 100 to 150 °C, and they contain 2.8 wt. % total solute, dominated by alkalis and silica. The Cl content is lower than that in the seawater (Silver et al. 2000). In the Izu-Bonin/Mariana forearc pore fluids have a Cl/(Cl+H₂O) concentration of 4.25 wt. % (Straub and Layne 2003).

Thermodynamic calculations performed at conditions corresponding to the blueschist-eclogite transition suggest that aqueous fluids are Na-Ca-Al-Si-bearing, with low Mg and Fe contents unless significant amounts of Cl are present (Manning 1998). Similarly, a 5-molal NaCl solution in equilibrium with garnet and orthopyroxene at 900 °C and 2 GPa has 8.3 wt. % solute, dominated by SiO₂ and with elevated contents of Mg, Ca and Al (Brenan et al. 1995a). Thus, the solutes in H₂O-rich fluids in subduction zones are dominated by alkali and aluminosilicate components. Fluid inclusions in exhumed ultra-high pressure rocks have salinities ranging between 1 and 7 wt. % NaCl equiv. (Gao and Klemd 2001). This is in agreement with the ratio of Cl and H₂O flux from the slab to the mantle wedge, indicating an overall salinity of 7 wt. % (Jarrard 2003).

Halogens such as chlorine and fluorine are very soluble and mobile elements, and may serve as ligands for the formation of aqueous complexes. Elevated concentrations of halogens in

magmatic arcs indicate that they are released from the slab and can effectively be transferred to the partial melting region in the mantle wedge (Schilling et al. 1978, Ito et al. 1983). Various models indicate that the main portion of subducted Cl is lost from the slab before reaching a depth of 200 km, and imply that subducting lithologies are unable to carry halogens down into the deeper mantle (e.g., Schilling et al. 1978, Ito et al. 1983, Dixon et al., 2002) whereas others argue for partial recycling of halogens into the Earth's interior (Philippot 1993, Magenheimer et al. 1995). According to Smith (1981) the total amount of chlorine and fluorine stored in the Earth's mantle is $7-20 \cdot 10^{18}$ kg and $\sim 8 \cdot 10^{19}$ kg, respectively. He considers apatite to be the main halogen carrier, with ~ 3 wt. % F and 1 wt. % Cl in its structure, followed by phlogopite with ~ 0.5 wt. % F and 0.05 wt. % Cl.

1.6. Trace element signature of subduction fluids

The fluid-mineral partitioning studies indicate that large ion lithophile elements (LILE) such as K, Rb and Cs are preferentially transported *via* fluid from the slab to the mantle wedge whereas high-field strength elements (HFSE), for instance, Ti, Zr, Nb or Ta, are less soluble and remain immobile (Keppler 1996, Audétat and Keppler 2005, Tropper and Manning 2005, Kessel et al. 2005, Antignano and Manning 2008). In this scenario, arc magmas are expected to show an enrichment in LILE but a depletion in HFSE. Mechanisms of enrichment in the incompatible elements relative to N-MORB remain, however, still poorly understood. Trace element patterns of subduction-zone fluids show enrichments in LILE and Pb, and depletions in high field strength elements (Manning 2004). The decoupling of LILE and HFSE is further promoted by the presence of Cl (Brenan *et al.* 1995b, Keppler, 1996; Fig. 1-5).

By contrast, high field strength elements (HFSE) such as Ti, Zr, Hf, Nb, Ta are very immobile in aqueous fluids at high pressure and temperature due to their very low solubilities in H₂O. Experimental solubilities range from few to some tens ppm at 700-1100 °C and 1-2.3 GPa (Audétat and Keppler 2005, Tropper and Manning 2005, Antignano and Manning 2008, Baier et al. 2008). The solubility of high field strength elements may be enhanced by complexing with other ligands or incorporation in aluminosilicate polymers (Audétat and Keppler 2005, Antignano and Manning 2008, Manning et al. 2008). These equilibria and their systematics have yet to be explored, and their potential for affecting the immobility of HFSE in the slab-derived fluids evaluated.

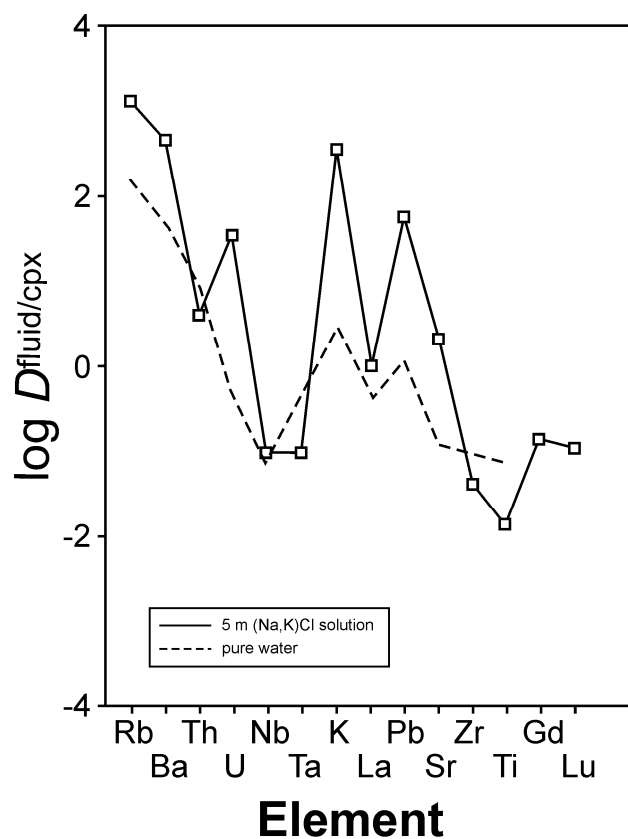


Fig. 1-5. Partition coefficients of trace elements between aqueous fluids and clinopyroxene at 1040 °C and 3 kbar (redrawn from Keppler 1996). Note the enhancement of partitioning into the fluid phase by the presence of chlorine.

1.7. Research objectives and thesis organization

The principal objective of this thesis is to constrain the behavior of trace elements and halogens in mineral-aqueous fluid systems under subduction zone conditions. Experimental and computational methods were used to investigate the incorporation of chlorine and fluorine in the mantle mineral phases and their partitioning into aqueous fluids, and to study zirconium mobility in aqueous fluids. This thesis consists of three manuscripts prepared for publication in international journals (Chapters. 2-4) where I have addressed the following research goals:

(1) Experimental determination of the partitioning of chlorine and fluorine between aqueous fluid and mafic minerals (forsterite, enstatite and pyrope) at temperatures and pressures applicable to the mantle wedge. Experimental runs were performed in a piston cylinder apparatus at 1100 °C and 2.6 GPa and chemical compositions of the run products were analyzed by electron microprobe and secondary ion mass spectrometry. Mass balance calculations were employed to determine partition coefficients for fluorine and chlorine between aqueous fluid and silicate minerals; these data are then used to constrain the effective rock/fluid ratio and therefore the style of flow through the mantle wedge in subduction zones.

(2) A computational study of the incorporation of fluorine in forsterite by a silicon vacancy substitution mechanism and its energetics to very high pressures. I performed an *ab-initio* simulation by general gradient approximation (GGA) and local density approximation (LDA) on a set of variably fluorinated forsterite structures as well as minerals of the humite group and sellaite, MgF₂. The simulations define enthalpy, and pressure-volume equations of state and non-ideal mixing properties of all phases present along the forsterite-MgF₂ binary join. The humite-group phases and sellaite represent buffers of fluorine concentration in forsterite, hence the corresponding solubilities of fluorine were evaluated up to 1800 K and 20 GPa. These simulations complement the experimental studies on halogen partitioning between fluid and minerals and provide insights into the atomistic substitution mechanism.

(3) Experimental investigation of zircon solubility in aqueous fluids at high pressure and temperature by *in situ* observations in a hydrothermal diamond anvil cell. I have determined the Zr solubility in pure H₂O at 865-1025 °C and 0.6-2.0 GPa as well as studying the effect of silica, chlorine and aluminosilicate on the solubility. The results were used to develop a thermodynamic model for the Zr solubility as a function of temperature and solvent density. I use this model to show that Zr is not transported by subduction zone fluids and the Zr budget of arc magmas is dominated by the mantle source.

The thesis concludes with the summary of results (Chapter 5).

1.9. References

- Abrahmson E. H., Brown J. M. (2004): Equation of state of water based on speeds of sound measured in the diamond-anvil cell, *Geochimica and Cosmochimica Acta*, 68, 1827-1835.
- Antignano A., Manning C. E. (2008): Rutile solubility in H₂O, H₂O-SiO₂, and H₂O-NaAlSi₃O₈ fluids at 0.7-2.0 GPa and 700-1000 °C: implications for mobility of nominally insoluble elements, *Chemical Geology*, 255, 283-293.
- Audétat A., Keppler H. (2005): Solubility of rutile in subduction zone fluids, as determined by experiments in the hydrothermal diamond anvil cell, *Earth and Planetary Science Letters*, 232, 393-402.
- Baier J., Audétat A., Keppler H. (2008): The origin of the negative niobium tantalum anomaly in subduction zone magmas, *Earth and Planetary Science Letters*, 267, 290–300.
- Berhorst A., Flueh E. R., McIntosh K. D., Ranero C. R., Ahmed I., Silver E. A., Barckhausen U. (2003): The crustal structure of the convergent Nicaraguan margin from a combined reflection and refraction study, *Journal of Geophysical Research*, Abstract 9692, 5.

- Brenan J. M., Shaw H. F., Phinney D. L., Ryerson F. J. (1994) Rutile-aqueous fluid partitioning of Nb, Ta, Hf, Zr, U and Th δ implications for high-field strength element depletions in island-arc basalts, *Earth and Planetary Science Letters*, 128, 327-339.
- Brenan J. M., Shaw H. F., Ryerson F. J. (1995a): Experimental evidence for the origin of lead enrichment in convergent-margin magmas, *Nature*, 378, 54-56.
- Brenan J. M., Shaw H. F., Ryerson F. J., Phinney D. L. (1995b): Mineral-aqueous fluid partitioning of trace elements at 900 °C and 2.0 GPa: Constraints on the trace element chemistry of mantle deep crustal fluids, *Geochimica et Cosmochimica Acta*, 59, 3331-3350.
- Bureau H., Keppler H., (1999): Complete miscibility between silicate melts and hydrous fluids in the upper mantle: experimental evidence and geochemical implications, *Earth and Planetary Science Letters*, 165, 187–196.
- Churakov S. V., Gottschalk M. (2003): Perturbation theory based equation of state for polar molecular fluid: I. Pure fluids, *Geochimica et Cosmochimica Acta*, 67, 2397–2414.
- Davies G. H. (1999): The role of hydraulic fractures and intermediate-depth earthquakes in generating subduction-zone magmatism, *Nature*, 398, 142–145.
- Dixon J. E., Leist L., Langmuir C., Schilling J. G. (2002): Recycled dehydrated lithosphere observed in plume-influenced mid-ocean-ridge basalt, *Nature*, 420, 385-389.
- Dobson D. P., Meredith P. G., Boon S. A. (2002): Simulation of subduction zone seismicity by dehydration of serpentine, *Science*, 298, 1407-1410.
- Dolejs D., Manning C. E. (2010): *Thermodynamic model for mineral solubility in aqueous fluids: theory, calibration, and application to model fluid-flow systems*, *Geofluids*, 10 (Frontiers anniversary volume), 20-40.
- Fryer P., Pearce J. A., Stokking L. B., et al. (1990): Proceedings of the Ocean Drilling Program, Initial Reports, 125, 1092 pp.
- Gao J., Klemd R., (2001): Primary fluids entrapped at blueschist to eclogite transition: evidence from the Tianshan meta-subduction complex in northwest China, *Contributions to Mineralogy and Petrology*, 142, 1-14.
- Green T. H., Ringwood A. E. (1968): Genesis of the calc-alkaline igneous rock suite, *Contributions to Mineralogy and Petrology*, 18, 163-174.
- Guo F., Nakamura E., Fan W., Kobayashi K., Li C., Gao X. (2009): Mineralogical and geochemical constraints on magmatic evolution of Paleocene adakitic andesites from the Yanji area, NE China, *Lithos*, 112, 321-341.
- Hack A. C., Hermann J., Mavrogenes J. A. (2007a): Mineral solubility and hydrous melting relations in the deep Earth: analysis of some binary A-H₂O system pressure-temperature-composition topologies, *American Journal of Science*, 307, 833-855.

- Hack A. C., Thompson A. B., Aerts M. (2007b): Phase relations involving hydrous silicate melts, aqueous fluids, and minerals, *Reviews in Mineralogy and Geochemistry*, 65, 129-177.
- Hacker B. R., Peacock S. M., Abers G. A., Holloway S. D. (2003): Subduction factory: 2. Are intermediate-depth earthquakes in subducting slabs linked to metamorphic dehydration reactions? *Journal of Geophysical Research*, 108, 2030-2046.
- Ito E., Harris D. M., Anderson A. T. (1983): Alteration of oceanic crust and geologic cycling of chlorine and water, *Geochimica et Cosmochimica Acta*, 47, 1613-1624.
- Iwamori H. (1998): Transportation of H₂O and melting in subduction zones, *Earth Planetary Science Letters*, 160, 65-80.
- Jarrard R. D. (2003): Subduction fluxes of water, carbon dioxide, chlorine and potassium, *Geochemistry Geophysics Geosystems*, 4, doi: 10.1029/2002GC000392.
- Karsli O., Dokuz A., Uysal I., Aydin F., Kandemir R., Wijbrans J. (2010): Generation of the Early Cenozoic adakitic volcanism by partial melting of mafic lower crust, Eastern Turkey: Implication for crustal thickening to delamination, *Lithos*, 114, 109-120.
- Kawamoto T. (2006): Hydrous phases and water transport in the subducting slab, *Reviews in Mineralogy & Geochemistry*, 62, 273-289.
- Kay R. W. (1978): Aleutian magnesian andesites: Melts from subducted Pacific ocean crust, *Journal of Volcanology and Geothermal Research*, 4, 117-132.
- Kennedy G. C., Heard H. C., Wasserburg G. J., Newton R. C. (1962): The upper three-phase region in the system SiO₂-H₂O, *American Journal of Science*, 260, 501-521.
- Keppler H. (1996): Constraints for partitioning experiments on the composition of subduction-zone fluids, *Nature*, 380, 237-240.
- Kerrick D.M., Connolly J. A. D. (2001): Metamorphic devolatilization of subducted mid-ocean ridge metabasalts: implications for seismicity, arc magmatism and volatile recycling, *Earth and Planetary Science Letters*, 189, 19-29.
- Kessel R., Schmidt M. W., Ulmer P., Pettke T. (2005): Trace elements signature of subduction-zone fluids, melts and supercritical liquids at 120-180 km depth, *Nature*, 437, 724-727.
- Kimura G., Silver E., Blum P., et al. (1997): Costa Rica Accretionary Wedge. Sites 1039-1043, *Proceedings of the Ocean Drilling Program, Initial Reports 170*, 458 pp.
- Magenheim A. J., Spivack A. J., Michael P. J., Gieskes J. M. (1995): Chlorine stable isotope composition of the oceanic crust: Implications for the Earth's distribution of chlorine, *Earth and Planetary Science Letters*, 131, 427-432.
- Manning, C. E. (1998): Fluid composition at the blueschist-eclogite transition in the model system Na₂O-MgO-Al₂O₃-SiO₂-H₂O-HCl, *Swiss Bulletin of Mineralogy and Petrology*, 78, 225-242.

- Manning C. E. (2004): The chemistry of subduction-zone fluids, *Earth and Planetary Science Letters*, 223, 1-16.
- Manning C. E. (2007): Solubility of corundum + kyanite in H₂O at 700°C and 10 kbar: evidence for Al-Si complexing at high pressure and temperature, *Geofluids*, 7, 258-269.
- Manning C. E., Wilke M., Schmidt C., Cauzid, J. (2008): Rutile solubility in albite-H₂O and Na₂Si₃O₇-H₂O at high temperatures and pressures by in-situ synchrotron radiation micro-XRF, *Earth and Planetary Science Letters*, 272, 730-737.
- Marsh B. D., Carmichael I. S. E. (1974): Benioff zone magmatism, *Journal of Geophysical Research*, 79, 1196-1206.
- Marshall W. L., Franck E. U. (1981): Ion product of water substance, 0-1000 °C 1-10,000 bars new international formulation and its background, *Journal of Physical and Chemical Reference Data*, 10, 295 pp.
- Matsumoto T., Kawabata T., Matsuda J. I., Yamamoto K., Mimura K. (2003): ³He/⁴He ratios in well gases in the Kinki district, SW Japan: surface appearance of slab-derived fluids in a non-volcanic area, *Earth and Planetary Science Letters*, 216, 221-230.
- Mibe K., Fujii T., Yasuda A. (1999): Control of the location of the volcanic front in island arcs by aqueous fluid connectivity in the mantle wedge, *Nature*, 401, 259– 262.
- Mibe K., Fujii T., Yasuda A. (2002): Composition of aqueous fluid coexisting with mantle minerals at high pressure and its bearing on the differentiation of the Earth's mantle, *Geochimica et Cosmochimica Acta*, 66, 2273-2285.
- Mysen B. O. (1998): Interaction between aqueous fluid and silicate melt in the pressure and temperature regime of the Earth's crust and upper mantle, *Neues Jahrbuch für Mineralogie, Abhandlungen*, 172, 227-244.
- Newton R. C., Manning C. E. (2002): Solubility of enstatite + forsterite in H₂O at deep crust/upper mantle conditions: 4 to 15 kbar and 700 to 900 °C, *Geochimica et Cosmochimica Acta*, 66, 4165-4176.
- Newton R. C., Manning C. E. (2003): Activity coefficient and polymerization of aqueous silica at 800 °C, 12 kbar, from solubility measurements on SiO₂-buffering mineral assemblages, *Contributions to Mineralogy and Petrology*, 146, 135–143.
- Newton R. C., Manning C. E. (2009): Hydration state and activity of aqueous silica in H₂O-CO₂ fluids at high pressure and temperature, *American Mineralogist*, 94, 1287-1290.
- Pasquale V., Verdoya M., Chiozzi P. (2005): Thermal structure of the ionian slab, *Pure and Applied Geophysics*, 162, 967-986.
- Peacock S. M., Wang K. (1999): Seismic consequences of warm versus cool subduction metamorphism: examples from southwest and northeast Japan, *Science*, 286, 937-939.

- Pearce J. A., Stern R. J. (2006): The origin of back-arc basin magmas: trace element and isotope perspectives, *Back-arc Spreading Systems: Geological, Biological, Chemical and Physical interactions*, American Geophysical Union, *Geophysical Monograph Series 166*, 63-86.
- Philippot P. (1993): Fluid-melt-rock interaction in mafic eclogites and coesite-bearing metasediments: Constraints on volatile recycling during subduction, *Chemical Geology*, *108*, 93–112.
- Plank T., Langmuir C. H. (1998): The chemical composition of subducting sediment and its consequences for the crust and mantle, *Chemical Geology*, *145*, 325-394.
- Ranero C. R., Morgan J. P., McIntosh K., Reichert C. (2003): Bending-related faulting and mantle serpentinization at the Middle America trench, *Nature*, *425*, 367-373.
- Rüpke L. H., Morgan J. P., Hort M., Connolly J. A. D. (2004): Serpentine and the subduction zone water cycle, *Earth and Planetary Science Letters*, *223*, 17-34.
- Sallares V., Ranero C. R. (2003): Structure of the incoming ocean plate and the erosional convergent margin off Antofagasta, northern Chile, *Geophysical Research Abstracts*, *5*, 02839.
- Schilling J. G., Unni C. K., Bender M. L. (1978): Origin of chlorine and bromine in the oceans, *Nature*, *273*, 631-636.
- Schmidt M. W., Poli S. (1998): Experimentally based water budgets for dehydrating slab and consequences for arc magma generation, *Earth and Planetary Science Letters*, *163*, 361-379.
- Silver E., Kastner M., Fisher A., Morris J., McIntosh K., Saffer D. (2000): Fluid flow paths in the middle America trench and Costa Rica margin, *Geology*, *28*, 679-682.
- Smith J. V. (1981): Halogen and phosphorus storage in the Earth, *Nature*, *289*, 762-765.
- Sowerby J. R., Keppler H. (2002): The effect of fluorine, boron and excess sodium on the critical curve in the albite-H₂O system. *Contributions to Mineralogy and Petrology*, *143*, 32–37.
- Stalder R., Ulmer P. (2001): Phase relations of a serpentine composition between 5 and 14 GPa: significance of clinohumite and phase E as water carriers into the transition zone, *Contributions to Mineralogy and Petrology*, *140*, 670-679.
- Straub S. M., Layne G. D. (2003): The systematic of chlorine, fluorine, and water in Izu arc front volcanic rocks: implications for volatile recycling in subduction zone, *Geochimica et Cosmochimica Acta*, *21*, 4179-4203.
- Staudigel H., Hart S., Schmincke H., Smith B. (1989): Cretaceous ocean crust at DSDP Sites 417 and 418: Carbon uptake from weathering versus loss by magmatic outgassing, *Geochimica et Cosmochimica Acta*, *53*, 3091-3094.

- Tropper P., Manning C. E. (2005): Very low solubility of rutile in H₂O at high pressure and temperature, and its implications for Ti mobility in subduction zones. *American Mineralogist*, 90, 502-505.
- van Keken P. E., Kiefer B., Peacock S. M. (2002): High-resolution models of subduction zones: implications for mineral dehydration reactions and the transport of water into the deep mantle, *Geochemistry, Geophysics, Geosystems*, 3, doi: 10.1029/2001GC000256.
- Wagner W., Pruss A. (2002): The IAPWS formulation (1995) for the thermodynamic properties of ordinary water substance for general and scientific use. *Journal of Physical and Chemical Reference Data*, 31, 387-535.
- Wallmann K. (2001): The geological water cycle and the evolution of marine $\delta^{18}\text{O}$ values, *Geochimica et Cosmochimica Acta*, 65, 2469-2485.
- Wiryana S., Slutsky L. J., Brown J. M. (1998): The equation of state of water to 200 °C and 3.5 GPa: model potentials and the experimental pressure scale, *Earth and Planetary Science Letters*, 163, 123-130.
- Withers A.C., Kohn S.C., Brooker R.A., Wood B.J. (2000): A new method for determining the PóVóT properties of high-density H₂O using NMR: results at 1.4-4.0 GPa and 700ó1100 °C. *Geochimica et Cosmochimica Acta*, 64, 1051–1057.
- Yokoyama T., Nakamura E., Kobayashi K., Kuritani T. (2002): Timing and trigger of arc volcanism controlled by fluid flushing from subducting slab, *Proceedings of the Japanese Academy, Ser. B, Physical and Biological Sciences*, 78, 190-195.
- Zhang Y. G., Frantz J. D. (2000): Enstatite-forsterite-water equilibria at elevated temperatures and pressures, *American Mineralogist*, 85, 918-925.
- Zotov N., Keppler H. (2000): *In-situ* Raman spectra of dissolved silica species in aqueous fluids to 900 °C and 14 kbar, *American Mineralogist*, 85, 600-603.
- Zotov N., Keppler H. (2002): Silica speciation in aqueous fluids at high pressures and high temperatures, *Chemical Geology* 184, 71-82.

2. Partitioning of halogens between mantle minerals and aqueous fluids: an experimental study

2.0. Abstract

Understanding the global geochemical cycle of halogens requires knowledge of solubility and incorporation mechanisms of fluorine and chlorine in the upper mantle silicate minerals. I have performed phase equilibrium experiments in the system forsterite-enstatite-pyrope-H₂O with MgCl₂ or MgF₂ at 1100 °C and 2.6 GPa to constrain the solubility of halogens in the peridotite mineral assemblage and the fluid-mineral partition coefficients. The chlorine solubility in forsterite, enstatite and pyrope is very low, 0.2-0.9 ppm, and it is independent of the fluid salinity (0.3-40 wt. % Cl), suggesting that some intrinsic saturation limit in the crystal is reached already at very low Cl concentrations. Chlorine is therefore exceedingly incompatible in upper mantle minerals. The fluorine solubility is 16-31 ppm in enstatite and 24-52 ppm in pyrope, again independent of fluid salinity. Forsterite dissolves 246-267 ppm up to a fluid salinity of 1.6 wt. % F. At higher fluorine contents in the system, forsterite is replaced by the minerals of the humite group. Fluorine concentration of 2.6 wt. % in clinohumite, 3.6 wt. % in humite, 4.6-6.7 wt. % chondrodite, and 11.4 wt. % in norbergite were observed. The fluorine solubility in forsterite and garnet is comparable to that of hydroxyl, which would be consistent with the charge coupled substitution MgO₂ F₂ in forsterite, and fluorination of oxygen polyhedra and charge balance by local chemical defects in pyrope. In enstatite the fluorine solubility in Al-bearing systems is much lower than that of hydroxyl, revealing that the substitution [SiO]²⁺ [AlF]²⁺ is ineffective. The decrease in chlorine solubility by four orders of magnitude when compared to fluorine is consistent with increasing lattice strain. The fluid-mineral partition coefficients are 10¹-10³ for fluorine and 10³-10⁶ for chlorine. Since the latter values are approximately three orders of magnitude higher than those for hydroxyl partitioning, fluid flow from subducting slab through the mantle wedge will lead to more efficient sequestration of H₂O into the nominally anhydrous minerals. In turn, this progressive decoupling of chlorine and H₂O leads to a gradual increase in the fluid salinity. Simple mass balance calculations reveal that rock-fluid ratios of (1.3-4) × 10³ are required to produce the characteristic Cl/H₂O signature of primitive arc magmas, whereas the rock-fluid ratios of (1.4-6) × 10³ are necessary to increase the fluid salinity to the levels found in fluid inclusions in eclogites. Accordingly, fluid flow from the subducted slab into the zone of melting in the mantle wedge does not only occur in narrow channels, but the fluid is predicted to pervasively infiltrate and interact with a large volume of mantle peridotite.

2.1. Introduction

Fluorine and chlorine are minor constituents in the upper mantle and were traditionally interpreted being hosted by hydrous phosphates or silicates (Smyth 1981, Smyth et al. 1981, Newsom 1995, Aiuppa et al. 2009). In contrast, no systematic attention has been paid to possibilities of incorporating halogens in the nominally anhydrous silicates (*cf.* Bromiley and Kohn 2007). This is particularly relevant for halogen release during main dehydration reactions in the slab and the hydrated upper mantle. Subducted serpentinites host between 45 and 2000 ppm Cl (Orberger et al. 1999, Scambelluri et al. 2004, Bonifacie et al. 2008, Wei et al. 2008) and 47 to 430 ppm F (Wei et al. 2008). However, concentrations of F and Cl in the primitive mantle are much lower, 25 and 17 ppm, respectively (McDonough and Sun 1995) and it is not clear if this budget is limited by the availability of accessory phosphates or hydrous silicates, or is controlled by halogen incompatibility in nominally anhydrous rock-forming silicates. If rock-forming silicates can incorporate fluorine or chlorine to an extent comparable to hydroxyl contents, they may become the most important planetary reservoir of halogens. In the opposite case, halogen incompatibility in the nominally anhydrous minerals would cause their release to slab-derived aqueous fluids, fluid flow through the mantle would induce changes in the fluid salinity, in addition, to providing ligands for complexing and transporting trace elements such as Pb, Ba, Sr or Rb.

In contrast to silicate minerals, chlorine and fluorine are quite soluble in silicate melts and aqueous fluids (Webster 1990, Webster 1992, Métrich and Rutherford 1992, Kravchuk and Keppler 1994, Icenhower and London 1997, Bureau and Keppler 1999). As a consequence, strong partitioning and efficient sequestration is expected to occur at the interface of various reservoirs such as mantle minerals, aqueous fluids and silicate melts in the slab-mantle wedge settings. This behavior makes halogens potentially sensitive tracers of geochemical cycling in the Earth's interior.

In this study, I report new experimental data on the solubility of fluorine and chlorine in forsterite, enstatite and garnet, and partition coefficients between these minerals and aqueous fluid at 1100 °C and 2.6 GPa. I apply our results to Cl and H₂O behavior in slab-derived aqueous fluids and mantle peridotite to interpret the Cl/H₂O ratios of primitive arc magmas and aqueous fluids in eclogites and gain quantitative insights into the distributed vs. focused nature of the fluid flow through the mantle wedge.

2.2. Experimental methods

Experiments were performed in an end-loaded piston cylinder apparatus at Bayerisches Geoinstitut (Germany). Starting materials were mixtures of high-purity chemicals: Mg(OH)₂ 99.95 %, Al(OH)₃ 99.95 % and SiO₂ 99.99 %, or anhydrous silicate glasses synthesized from MgO 99.99 %, Al₂O₃ 99.995 % and SiO₂ 99.99 %. All oxides were fired at 1500 °C for 3 hours before use. The oxide-hydroxide mixtures were carefully weighed and ground in an agate mortar for 40-60 minutes. For the glass preparation, the mixture was placed in a platinum crucible, melted at 1600 °C for 2 hours, and rapidly quenched. The resulting glass was ground in an agate mortar for 40-60 minutes under ethanol and dried. Pt₉₅Rh₀₅ capsules, 10 mm long and 5 mm in diameter were used for the experiments. 120-140 mg of the starting material together with 30-40 mg MgCl₂ · 6 H₂O, MgF₂ or their relative aqueous solutions were loaded into capsules to achieve the desired salinity, and sealed by arc welding. During welding the capsule was held in a brass jacket cooled by liquid nitrogen to prevent any loss of volatiles. The weight loss after welding was less than 0.4 % of the charge mass. The sealed capsules were stored in oven at 130 °C for several hours to check for leakage.

The capsules were placed in 1/2-inch talc-pyrex assemblies with tapered graphite furnaces and run in an end-loaded piston-cylinder apparatus at $T = 1100$ °C and $P = 2.6$ GPa for 2 days. These conditions are well below the fluid-saturated solidi in the systems forsterite-enstatite-H₂O and pyrope-H₂O (Fig. 2-1) to ensure the formation of mineral-fluid assemblages in the absence of silicate melt. Due to the presence of hydrates or fluids in the capsule, the assembly was heated and pressurized simultaneously to prevent excessive capsule deformation or failure and run conditions were reached in 30 minutes by a hot piston-out path. Temperature was controlled using a Pt-Pt₉₀Rh₁₀ thermocouple. The experiments were quenched nearly isobarically within several seconds by shutting off the power. After each experiment the capsule was carefully extracted from the assembly, weighed and the charge mounted for microprobe analysis and secondary ion mass spectrometry. Occasional weight loss during the experiments was less than 0.5 % of the total charge mass, and it was taken into account in the mass balance calculations.

Each charge was investigated with a scanning electron microscope to identify stable mineral phases and solute quench products. The major element composition of the minerals was measured with a JEOL JXA-8200 electron microprobe at the Bayerisches Geoinstitut in wavelength dispersive mode using the following standards: forsterite (Mg), diopside (Ca, Si), spinel (Al), orthoclase (K), albite (Na), iron (Fe), apatite (F) and vanadinite (Cl). The accelerating voltage was 15 kV, the beam current equal to 15 nA with a beam diameter of 1-2 μm. Element concentrations were obtained by the PRZ correction procedure. Chemical composition and salinity of the

coexisting fluid were calculated by mass balance using the bulk composition of the charge together with the amounts and composition(s) of the solid phase(s).

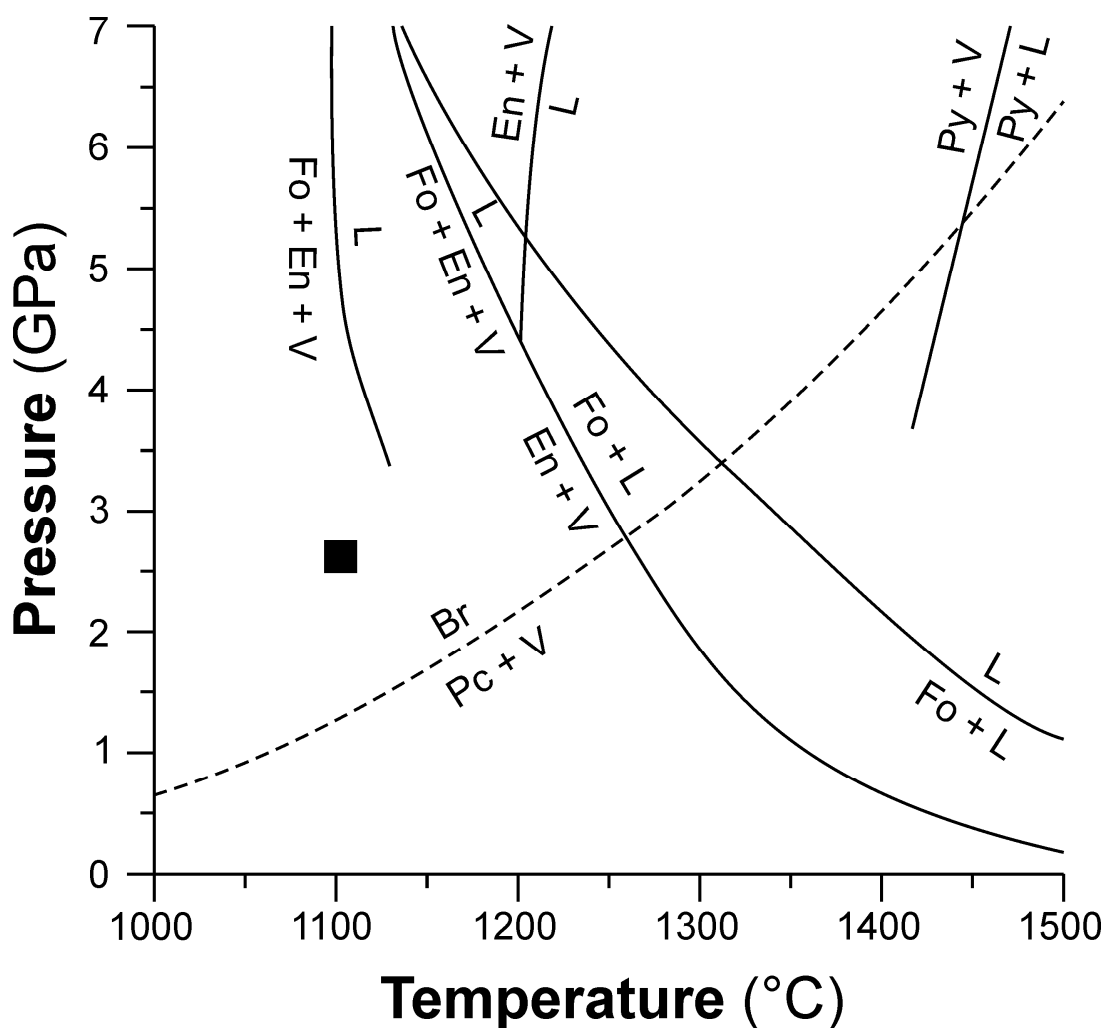


Fig. 2-1. Pressure-temperature diagram illustrating experimental conditions and the location of the fluid-saturated solidi in the peridotite-H₂O system (Kushiro et al. 1968, Inoue 1994, Sumita and Inoue 1996, Yamada et al. 2004, Fukui et al. 2005, Melekhova et al. 2007). Abbreviations: Br . brucite, En . enstatite, Fo . forsterite, L . liquid, Pc . periclase, V . vapor.

The F and Cl concentrations in forsterite, enstatite and pyrope were measured by a Cameca ims 6f SIMS instrument at the Helmholtz Centre Geoforschungszentrum Potsdam. The sample mounts were cleaned in an ultrasonic bath with high purity ethanol for five minutes prior to coating with a 35 nm thick high purity gold cover. The sample mounts were placed under high vacuum for at least 24 hours using an in-house designed sample carousel (Wiedenbeck et al. 2004). In the absence of suitably characterized and matrix-matched specimens necessary for the calibration of the relative secondary ion yields, I have produced standards by ion implantation. High quality specimens of forsterite, enstatite and pyrope were tested for major element homogeneity by electron microprobe analysis and for low intrinsic F and Cl contents using SIMS

point analyses. They all have low but detectable amounts of halogens which appeared to be fairly homogeneously distributed. The specimens were prepared with two plane parallel faces and the surfaces intended for ion implantation were polished to a roughness lower than 20 nm. All three phases were concurrently ion implanted first with ^{35}Cl at 130 kV and $1.3 \cdot 10^{14} \text{ cm}^{-2}$, followed by ^{19}F at 70 kV; $3.7 \cdot 10^{14} \text{ cm}^{-2}$). SIMS relative sensitivity factors were determined using the peak height method whereby the maximum $^{19}\text{F}/^{28}\text{Si}$ and $^{35}\text{Cl}/^{28}\text{Si}$ secondary ion intensities were compared to the known maximum halogen concentrations derived from ten thousand Monte Carlo simulations per material and implant species. Implant ion density vs. depth profiles were modeled using the SRIM version 2003.26 software. Calibration runs were carried out to a depth well below where implanted ions could be detected and the signals for both ^{19}F and ^{35}Cl intrinsic to the reference materials were subtracted from the maximum count rate observed for the implant profile.

The actual SIMS analyses used a 4 nA $^{133}\text{Cs}^+$ beam at a nominal voltage of 10 kV, which was focused to approximately 10 μm diameter spot on the polished sample surface. Since the calibration method employed ion implanted reference materials, I performed all analyses in a depth-profiling mode conducted with a 50 x 50 μm primary beam raster resulting in a sputtering rate of *ca.* 0.38 nm s^{-1} . Charge compensation was achieved using normal incident electron flooding operating at a 4 to 7 V potential above the -7.5 kV secondary ion extraction potential. The mass spectrometer was operated at a mass resolution ($M/\Delta M$ at 10% of peak maximum) of 1800-2300, which was sufficient to resolve the $^{19}\text{F}^{16}\text{O}$ isobaric interference from the ^{35}Cl peak. A 150 μm contrast aperture was used in conjunction with a 100 μm field aperture, equivalent to an 8 μm diameter field-of-view at the sample surface. A 50 V wide energy window, centred while sputtering a non-conductive sample using electron flooding, was used without the application of an additional offset voltage. A single cycle of the peak stepping sequence consisted of 18.9 Da (0.1 s per cycle), ^{19}F (4 s), ^{28}Si (2 s) and ^{35}Cl (8 s). All analyses were run until effectively constant count rates on both the ^{19}F and ^{35}Cl mass stations were obtained. A typical analysis required approximately 25 minutes of data collection whereas the calibration runs on the ion implanted reference materials took 50 minutes. The $^{19}\text{F}/^{28}\text{Si}$ and $^{35}\text{Cl}/^{28}\text{Si}$ ratios for each run were calculated from the mean count rates of the final 20 cycles of the data collection. The weight concentrations of fluorine or chlorine, respectively, were obtained by using the SiO_2 concentration of the mineral previously measured by electron microprobe. Chemical composition and halogen concentrations in the coexisting aqueous fluid were calculated by mass balance.

2.3. Results

Experimental run products were composed of one or two silicate minerals and an aqueous fluid with quenched solute. Individual phase assemblages are listed in Table 2-1. Forsterite, enstatite and pyrope are well crystallized, 50 to 500 μm in size, and exhibit subhedral or euhedral shapes (Fig. 2-2). The humite group minerals are also well crystallized, subhedral and 30-1000 μm in size. Chemically heterogeneous SiO_2 - and halogen-rich aggregates were found in all runs, and these are interpreted as quenched solute from aqueous fluid.

Table 2-1. Experimental conditions and product assemblages

Run	Starting materials	Nominal salinity (wt. % halogen in the fluid)	Run products
Chlorine			
16	synthetic glass (py)	39.61	pyrope, aqueous fluid
15	synthetic glass (py)	10.37	pyrope, aqueous fluid
34	synthetic glass (py)	5.10	pyrope, aqueous fluid
35	synthetic glass (py)	1.00	pyrope, aqueous fluid
37	oxide-hydroxide mix.	21.04	forsterite, enstatite, aqueous fluid
32	oxide-hydroxide mix.	3.02	forsterite, enstatite, aqueous fluid
33	oxide-hydroxide mix.	0.58	forsterite, enstatite, aqueous fluid
43	oxide-hydroxide mix.	0.32	forsterite, enstatite, aqueous fluid
Fluorine			
36	synthetic glass (py)	10.30	pyrope, aqueous fluid
38	synthetic glass (py)	1.79	pyrope, chondrodite, aqueous fluid
39	synthetic glass (py)	0.68	pyrope, aqueous fluid
26	oxide-hydroxide mix.	33.66	enstatite, chondrodite, norbergite, aqueous fluid
40	oxide-hydroxide mix.	8.51	enstatite, clinohumite, humite, aqueous fluid
41	oxide-hydroxide mix.	4.13	enstatite, chondrodite, aqueous fluid
42	oxide-hydroxide mix.	2.09	forsterite, enstatite, aqueous fluid
44	oxide-hydroxide mix.	0.30	forsterite, enstatite, aqueous fluid

py = pyrope glass, composition: 29.994 wt. % MgO , 25.923 wt. % Al_2O_3 , 44.714 wt. % SiO_2

oxide-hydroxide mixture, composition: 57.483 wt. % $\text{Mg}(\text{OH})_2$, 0.796 wt. %, $\text{Al}(\text{OH})_3$, 41.721 wt. % SiO_2 .

All Cl-bearing runs produced forsterite and enstatite, or pyrope, and an aqueous fluid. In F-bearing experiments with pyrope glass the resulting assemblage is pyrope + aqueous fluid; in run 38 a trace amount of chondrodite was observed.

In the F-bearing runs with oxide-hydroxide mixtures corresponding to forsterite and enstatite, the phase assemblage changes according to the fluorine concentration in the charge. At < 1.6 wt. % F in the fluid experiments yielded forsterite + enstatite + aqueous fluid (runs 42 and 44). At > 0.63 wt. % F in the fluid the phase assemblages are chondrodite + enstatite + aqueous fluid (run 41), enstatite + clinohumite + humite (run 40), and enstatite + chondrodite + norbergite + aqueous fluid (run 26). This sequence appears to reflect different stabilities of F-bearing end-members of the humite group as indicated by phase equilibrium studies of Duffy and Greenwood (1979) and Rice (1979, 1980).

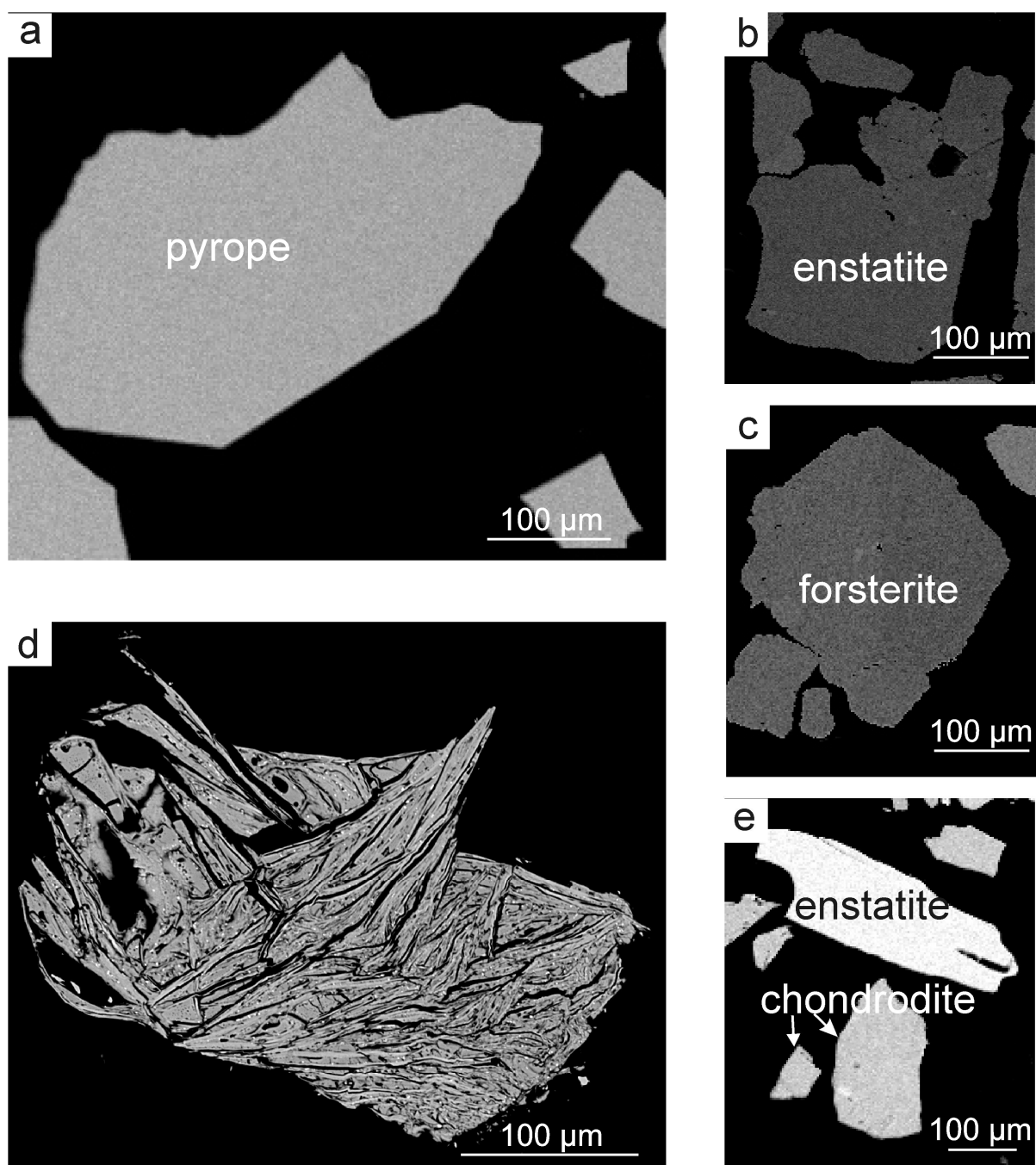


Fig. 2-2. Backscattered electron images of experimental run products: (a) pyrope (run 38); (b) enstatite (run 43); (c) forsterite (run 43); (d) quenched solute from aqueous fluid (run 32); (e) enstatite and chondrodite (run 26).

The major element compositions of forsterite and pyrope correspond to their ideal stoichiometric formulas. In Al_2O_3 -bearing experiments, enstatite incorporates 0.15-0.50 wt. % Al_2O_3 (0.07-0.02 Al atoms per 6 O-formula unit). The humite group minerals are solid solutions between the hydroxyl- and the fluorine-rich end-members, and contain very small amounts of Al_2O_3 . Chondrodite in equilibrium with pyrope contains 0.16 wt. % Al_2O_3 (run 38), whereas all other humite-group phases in low-Al charges have less than 0.03 wt. % Al_2O_3 .

Table 2-2. Chlorine concentrations in experimental run products

Run	Forsterite		Enstatite		Pyrope		Aqueous fluid salinity (wt. % Cl)
	<i>n</i>	conc. (ppm)	<i>n</i>	conc. (ppm)	<i>n</i>	conc. (ppm)	
16	-	-	-	-	2	0.20 ± 0.04	30.2 ± 5.2
15	-	-	-	-	1	0.36 ± 0.07	8.7 ± 1.5
34	-	-	-	-	2	0.28 ± 0.06	4.10 ± 0.64
35	-	-	-	-	2	0.56 ± 0.01	0.83 ± 0.13
37	3	0.45 ± 0.09	2	0.34 ± 0.07	-	-	17.2 ± 1.0
32	2	0.29 ± 0.06	2	0.31 ± 0.06	-	-	2.44 ± 0.12
33	-	-	2	0.28 ± 0.05	-	-	0.46 ± 0.02
43	4	0.55 ± 0.11	3	0.29 ± 0.06	-	-	0.25 ± 0.01

Table 2-3. Fluorine concentrations in experimental run products

Run	Forsterite		Enstatite		Pyrope	humite group mineral	Aqueous fluid salinity (wt. % F)	
	<i>n</i>	conc. (ppm)	<i>n</i>	conc. (ppm)	<i>n</i>	conc. (wt. %)		
36	-	-	-	-	1	52 ± 11	-	8.30 ± 1.45
38	-	-	-	-	2	47.1 ± 9.4	4.6 ± 0.1 (Chn)	1.32 ± 0.11
39	-	-	-	-	9	23.7 ± 4.7	-	0.51 ± 0.071
26	-	-	3	30.1 ± 6.0	-	-	11.4 ± 0.1 (Nrb)	17.5 ± 2.3
							6.7 ± 0.1 (Chn)	
40	-	-	2	19.4 ± 3.9	-	-	3.6 ± 0.1 (Hum)	4.80 ± 0.21
							2.6 ± 0.1 (Chu)	
41	-	-	2	30.6 ± 6.1	-	-	4.9 ± 0.1 (Chn)	0.63 ± 0.15
42	2	246 ± 49	2	18.3 ± 3.7	-	-	-	1.64 ± 0.064
44	4	267 ± 53	5	15.5 ± 3.1	-	-	-	0.22 ± 0.091

Chu = clinohumite; Hum = humite; Chn = chondrodite; Nrb = norbergite

The chlorine solubility in forsterite, enstatite and pyrope is very low, 0.2-0.7 ppm, and there is no correlation with the fluid salinity (Tab. 2-2; Fig. 2-3a). The fluorine solubility in these minerals is up to three orders of magnitude higher than that of chlorine, and it reaches 246-267 ppm F in forsterite, 15.5-30.1 ppm F in Al-bearing enstatite, and 23.7-52.3 ppm F in pyrope (Tab 2-3; Fig. 2-3b). The fluorine concentrations in the humite-group minerals vary as follows (Table 2-3; Fig. 2-4): clinohumite (2.6 wt. % F; molar F/(F+OH) = $X_F = 0.42$), humite (3.6 wt. % F; $X_F = 0.46$), chondrodite (4.6-6.7 wt. % F; $X_F = 0.42-0.61$), norbergite (11.4 wt. % F; $X_F = 0.60$). The coexistence of two humite group minerals in runs 26 and 40 permits calculation of the fluorine-hydroxyl partition coefficients: $D^{\text{hum}/\text{chum}} = X_F^{\text{hum}} / X_F^{\text{chum}} = 1.10$ and $D^{\text{no}/\text{cho}} = 0.98$. These results indicate almost no fractionation of fluorine between humite-group pairs at 1100 °C and 2.6 GPa.

Fig. 2-3 illustrates that the maximum solubility of halogens in forsterite, enstatite and pyrope have been reached independently of the fluid salinity, therefore, the fluid-mineral partition coefficients of chlorine and fluorine are expected to monotonously increase with the halogen content in the fluid (Fig. 2-3). The $D_{\text{Cl}}^{\text{fl}/\text{min}}$ increases from $4.5 \cdot 10^3$ to $1.6 \cdot 10^6$ (Fig. 2-5a) and the overall fit including all three mineral phases is described by the following power law:

$$D_{\text{Cl}}^{\text{fl/min}} = 27860X^{1.06}$$

(2-1)

where X is the fluid salinity in wt. % Cl. The standard deviation of the fit is 0.97.

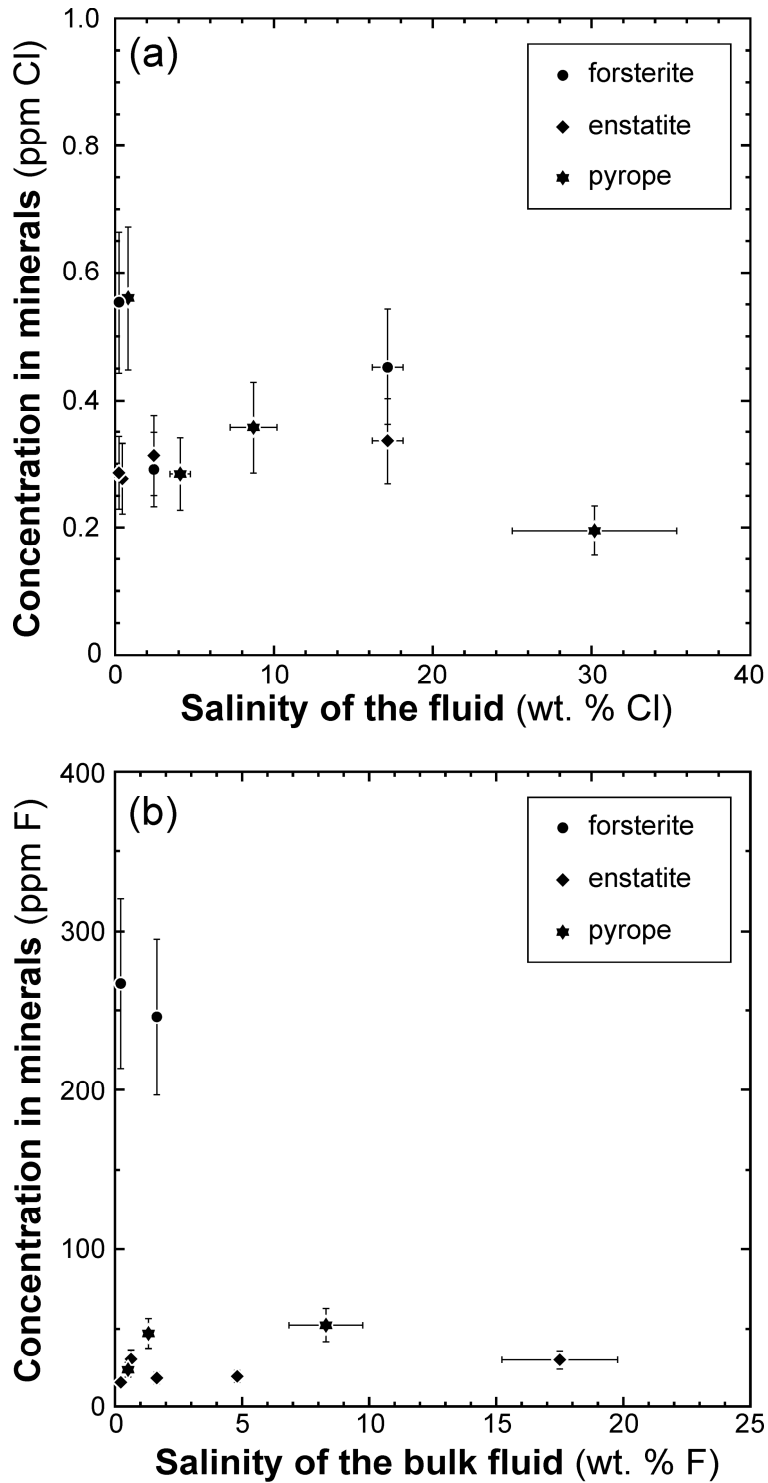


Fig. 2-3. Fluid salinity vs. halogen concentration in forsterite, enstatite and pyrope: (a) fluid salinity (wt. % Cl) vs. Cl ppm; (b) fluid salinity (wt. % F) vs. F ppm. The bulk salinity in (b) refers to a nominal fluid salinity neglecting possible presence of small amounts of fluoride melt.

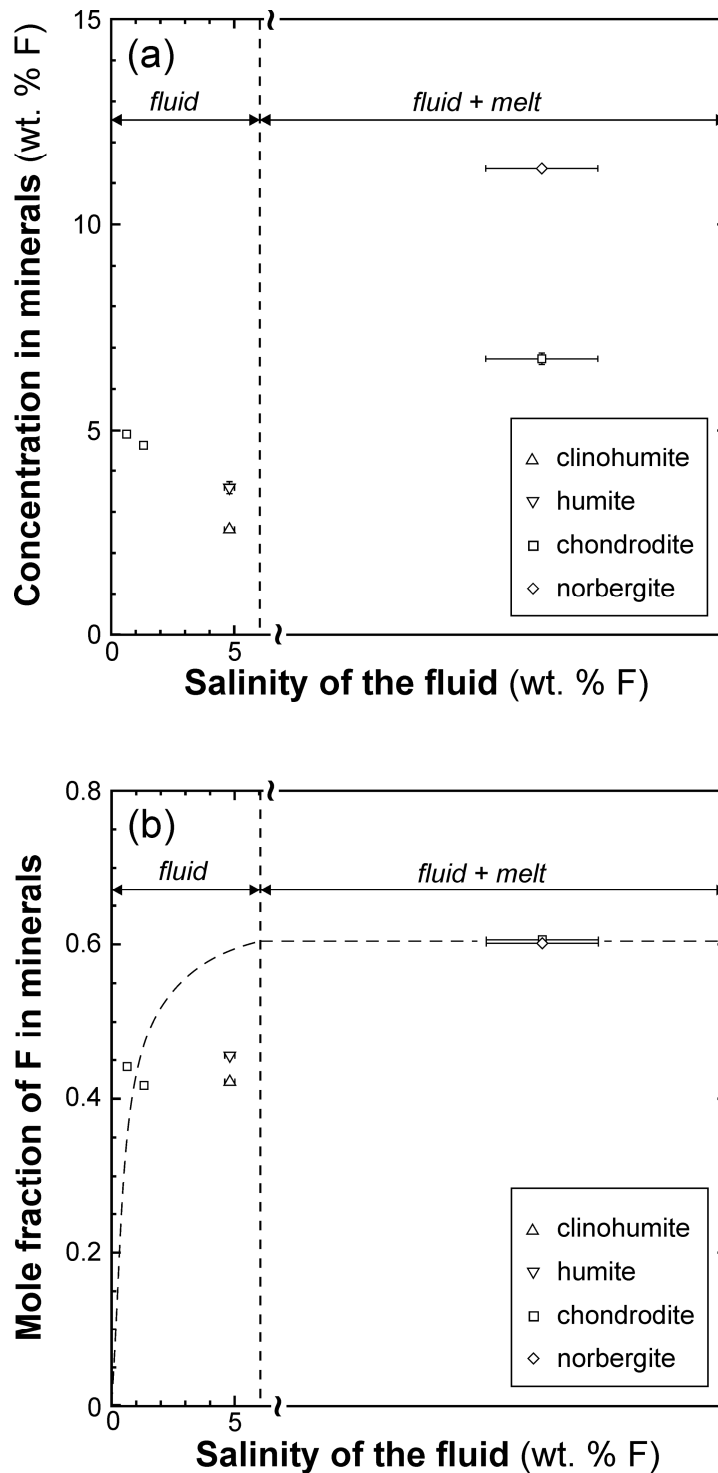


Fig. 2-4. Diagrams of (a) fluid salinity vs. halogen concentration and (b) fluid salinity vs. mole fraction of fluorine, X_F , in humite group minerals.

For fluorine, the partition coefficient for nominally anhydrous minerals, $D_F^{fl/min}$ increases from ~8 to 5.8×10^3 as the fluid salinity increases. Similar trend is observed for the humite group minerals, $D_F^{fl/min}$ ranges from $8.4 \cdot 10^0$ to $5.8 \cdot 10^3$. I note that both sets of partition coefficients achieve constant values at fluid salinities greater than 6 wt. % F (Fig. 2-5b). This trend, together

with the X_F in the humite group minerals, is interpreted to indicate occurrence of an invariant assemblage of silicate minerals + aqueous fluid + hydrous fluoride (or fluorosilicate) melt.

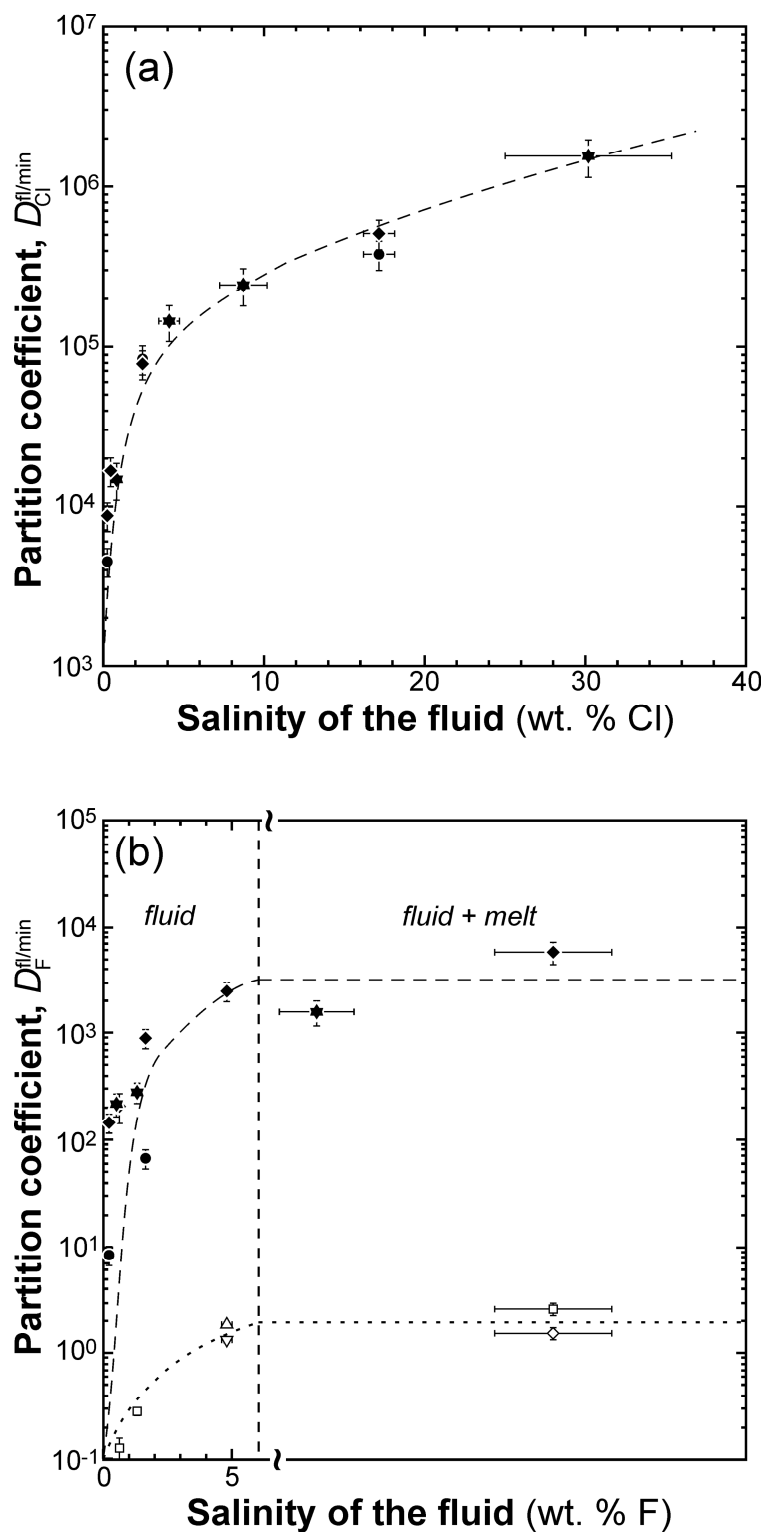


Fig. 2-5. Partition coefficients of (a) Cl and (b) F between aqueous fluid and silicate minerals. Closed symbols refer to anhydrous upper mantle minerals, open symbols to humite group minerals. Symbols are the same as in Figure 2-3 and 2-4.

Table 2-4. Partition coefficients between minerals and aqueous fluid

Run	$D^{fl/fo}$	$D^{fl/en}$	$D^{fl/py}$	$D^{fl/hgm}$
Chlorine				
16	-	-	$(1.55 \pm 0.41) \cdot 10^6$	-
15	-	-	$(2.44 \pm 0.64) \cdot 10^5$	-
34	-	-	$(1.45 \pm 0.37) \cdot 10^5$	-
35	-	-	$(1.47 \pm 0.38) \cdot 10^4$	-
37	$(3.80 \pm 0.78) \cdot 10^5$	$(5.11 \pm 1.1) \cdot 10^5$	-	-
32	$(8.40 \pm 1.73) \cdot 10^4$	$(7.81 \pm 1.6) \cdot 10^4$	-	-
33	-	$(1.67 \pm 0.34) \cdot 10^4$	-	-
43	$(4.5 \pm 0.92) \cdot 10^3$	$(8.74 \pm 1.78) \cdot 10^3$	-	-
Fluorine				
36	-	-	$(1.59 \pm 0.42) \cdot 10^3$	-
38	-	-	$(2.79 \pm 0.60) \cdot 10^2$	$(2.83 \pm 0.24) \cdot 10^{-1}$ (Chn)
39	-	-	$(2.17 \pm 0.53) \cdot 10^2$	-
26	-	$(5.81 \pm 1.39) \cdot 10^3$	-	$(2.60 \pm 0.34) \cdot 10^0$ (Chn) $(1.54 \pm 0.20) \cdot 10^0$ (Nrb)
40	-	$(2.48 \pm 0.57) \cdot 10^3$	-	$(1.87 \pm 0.089) \cdot 10^0$ (Chu) $(1.34 \pm 0.079) \cdot 10^0$ (Hum)
41	-	$(2.06 \pm 0.65) \cdot 10^2$	-	$(1.28 \pm 0.31) \cdot 10^{-1}$ (Chn)
42	$(6.68 \pm 1.36) \cdot 10^1$	$(8.97 \pm 1.83) \cdot 10^2$	-	-
44	$(8.39 \pm 1.71) \cdot 10^0$	$(1.44 \pm 0.25) \cdot 10^2$	-	-

fl = fluid; fo = forsterite; en = enstatite; py = pyrope; hgm = humite group minerals;
Chu = clinohumite; Hum = humite; Chn = chondrodite; Nrb = norbergite

2.4. Discussion

2.4.1. Incorporation mechanisms of halogens in nominally anhydrous silicates

In our experiments, fluorine and chlorine concentrations in forsterite, enstatite and pyrope do not vary with fluid salinity but remain approximately constant. This suggests that an intrinsic saturation limit was reached over the studied range of fluid salinities (0.2-30.2 wt. %). In addition, the Cl or F solubilities in three different silicate hosts are broadly similar.

The ionic radius of fluorine is very similar to that of hydroxyl, in addition to equality of their charges. The OH concentration in synthetic olivines synthesized at 1300 °C and 2 GPa is 54-375 ppm (Mosenfelder et al. 2006), which compares very well with our experimental results for F. Since the protonation of oxygen coupled with the formation of Mg vacancies in the octahedral site is the predominant incorporation mechanism (Smyth et al. 2006), I suggest *per analogiam* that the fluorine solubility in forsterite may be controlled by the substitution $[MgO_2]^{2-} \rightarrow [F_2]^{2-}$. By contrast, the H₂O concentration in pure enstatite synthesized at 1100 °C and 2.5 GPa is 113-223 ppm but it increases to 904-1102 ppm in aluminous enstatite (Rauch and Keppler 2002, Mierdel et al. 2007). These values are more than 20 times higher than our measured fluorine solubilities in Al-bearing systems, hence the substitution $[AlF]^{2+} \rightarrow [SiO]^{2+}$ does not appear to be the controlling incorporation mechanism for F in orthopyroxene. In garnet, hydroxyl and fluorine are

incorporated by the silicate vacancy, that is, $(\text{SiO}_4)^{4-} \leftrightarrow (\text{F}_4)^{4-}$ (Valley et al. 1983, Smyth et al. 1990, Visser 1993). Natural Ca-poor garnets crystallized at low pressure host as much as 3.8 wt. % F (Manning and Bird 1990, Smyth et al. 1990), whereas in our experiments at 2.6 GPa the fluorine solubility is 24-52 ppm. This remarkable decrease with increasing pressure is, however, in agreement with the water solubility in pyrope at 1000 °C and 2.5 GPa (100 ppm H₂O; Lu and Keppler 1997). These authors concluded, based on the dependence of the water solubility on pressure, that the hydroxyl is incorporated in pyrope as isolated OH groups charge balanced by chemical defects in the tetrahedral or dodecahedral site. Since the hydroxyl and fluorine solubilities in pyrope are very similar, an incorporation mechanism by the fluorination of oxygen polyhedra in pyrope is conceivable.

The chlorine solubility in forsterite, enstatite and pyrope is 0.2-0.7 ppm, that is, two to three orders of magnitude lower than that of fluorine and hydroxyl (Lu and Keppler 1997, Mosenfelder et al. 2006, Mierdel et al. 2007). This difference fits reasonably well with a decrease in partition coefficient predicted by lattice strain model (Blundy and Wood 1994, 2003) when considering that the ionic radius of chlorine (1.88 Å) is substantially greater than that of fluorine, hydroxyl or oxygen (1.33-1.40 Å; Shannon 1976).

2.4.2. The Cl/H₂O ratio of arc magmas and formation of mantle brines

Our experiments demonstrate that partition coefficients of chlorine between aqueous fluid and mantle minerals are very high (10^3 - 10^6), and the solubilities of Cl and H₂O in nominally anhydrous minerals differ by approximately four orders of magnitude. These findings imply that H₂O and Cl in aqueous fluids percolating through the peridotite assemblage will decouple, and the salinity will rise. Previous studies indicated that 99 % of the Cl budget of the arc magmas has its origin in the dehydrating slab (Straub and Layne 2003) and that nearly the whole Cl budget of the subducting slab is recycled into the planetary exosphere (Schilling et al. 1978, Ito et al. 1983, Straub and Layne 2003). The extremely high incompatibility of Cl in anhydrous minerals may thus provide a sensitive tracer of fluid evolution as well as a means to determine the efficiency of the water cycle in the slab-wedge system.

The initial salinity of aqueous fluids released during prograde dehydration of subducting mafic rocks and serpentinites varies from 0.4 to 2-7 wt. % NaCl equiv. (Straub and Layne 2003, Scambelluri et al. 2004). The upper limit is consistent with the ratio of global fluxes of Cl and H₂O from the subducting slab to the mantle (Gao and Klemd 2001). In contrast, the Cl/H₂O ratios of melt inclusions representing primary arc basalts range from 0.017 to 0.14 (Cervantes and Wallace 2003, Johnson et al. 2009), thus implying an interaction with fluids of salinity as high as

15 wt. % NaCl equiv. (Wallace 2005). Furthermore, primary fluid inclusions in metabasaltic eclogites range between 17 and 45 wt. % NaCl equiv. but the mechanism for the formation of the saline fluids has not yet been reliably identified (Scambelluri and Philippot 2001).

Our results show that less than 1 ppm Cl is incorporated in nominally anhydrous mantle minerals at 1100 °C and 2.6 GPa whereas the H₂O solubility in the garnet peridotite is ~975 ppm at the same conditions (Keppler and Bolfan-Casanova 2006, Mookherjee and Karato 2010). This implies that progressive fluid-rock interaction in the mantle wedge will lead to preferential removal of H₂O from the fluid and will increase its salinity. In order to demonstrate if the mechanism of preferential H₂O uptake to nominally anhydrous minerals may be important for the origin of saline fluids and for the high Cl/H₂O ratios in arc magmas I formulate a simple mass balance model to predict the changes in fluid salinity during its interaction with a mantle peridotite. I have considered several low-salinity fluids, with 0.24 to 4.25 wt. % Cl (Gao and Klemd 2001, Straub and Layne 2003, Scambelluri et al. 2004). Batch calculations of H₂O and Cl mass balance were performed to simulate Rayleigh chromatographic exchange (e.g., Albarède 1995). Calculations were performed by sequentially equilibrating increasing amounts of rock in 10 g increments with 1 g saline fluid. In each step, the solubility of H₂O in forsterite, enstatite and pyrope was scaled to the activity of H₂O in the fluid and the predicted amount of H₂O was transferred from the fluid to the minerals. Consequently, the amount of fluid was decreasing and its salinity was rising because Cl is nearly insoluble in minerals. In the model, the presence of hydrous phases, which can fractionate H₂O and Cl from the fluid, such as amphibole or phlogopite, is not considered because the fluid experiences an upward temperature path where hydrous silicates are unstable (Manning 2004).

Fig. 2-6 illustrates results of calculations for several plausible initial fluid salinities and progressive increasing degrees of interaction with the surrounding peridotite. All fluids show a monotonous increase in fluid salinity as H₂O is preferentially incorporated in the nominally anhydrous minerals during fluid flow in the mantle. The Cl/H₂O ratios of the primary arc melts are reproduced at the rock-fluid ratios between 1300 and 4000, whereas the formation of saline brines would require the rock-fluid ratios of 1400-6000.

These numbers strongly suggest that fluid flow from the subducted slab into the zone of melting in the mantle wedge does not only occur in narrow channels, but the fluid infiltrates and interacts with a large volume of mantle peridotite. Accordingly, the contribution of the mantle wedge may in fact dominate the flux of some fluid-mobile trace elements into the zone of melting. The salinity of the subduction zone fluids is constrained by the composition of fluids from shallow devolatilization (Scambelluri and Philippot 2001, Scambelluri et al. 2004) and by global

subduction fluxes (Jarrard et al. 2003). These two estimates vary between 0.24 and 4.25 wt. % Cl in the fluid.

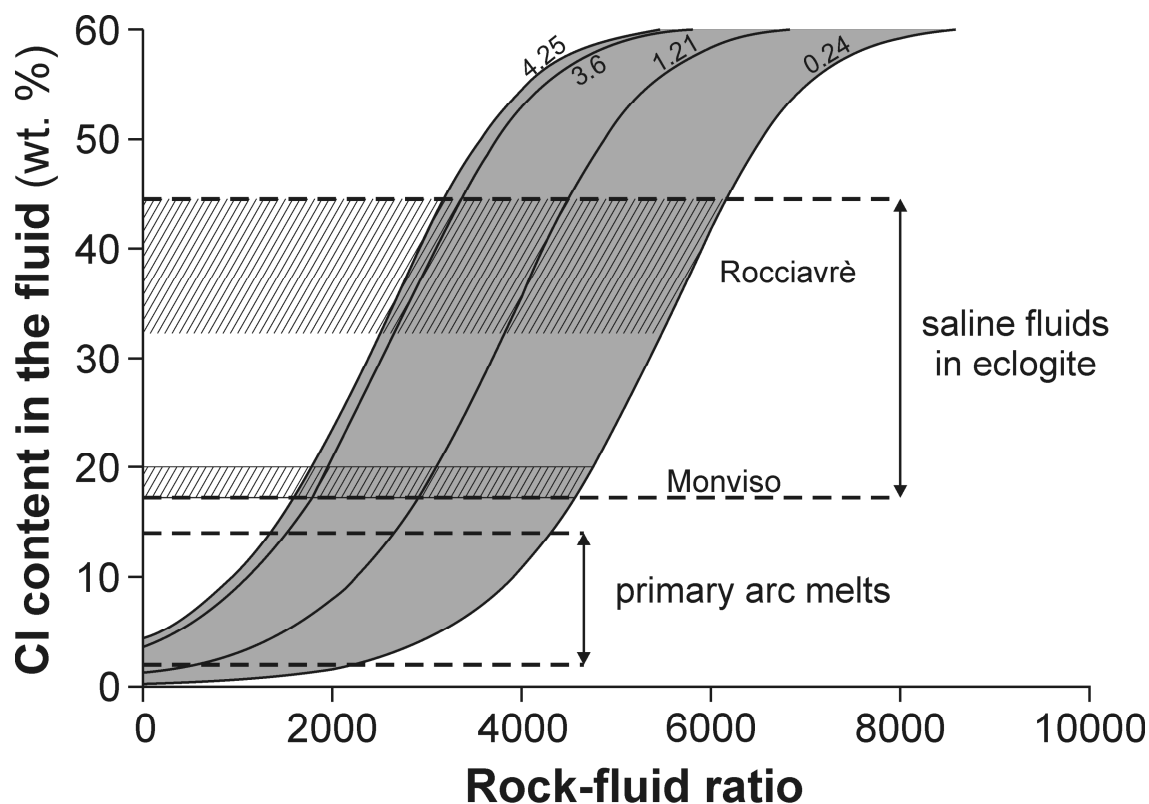


Fig. 2-6. The Cl concentration in the fluid vs. rock-fluid ratio diagram illustrating the progressive increase in the fluid salinity as the amount of the rock that interacted with the fluid along the flow path increased. The four different curves refer to four different initial salinities (0.24, 1.21, 3.6, and 4.25 wt. % Cl). The ranges of the Cl content in the aqueous fluids infiltrating the arc melting region (Cervantes and Wallace 2003, Johnson et al. 2009) and in the metabasaltic eclogites (Scambelluri and Phillippot 2001) are shown for comparison.

2.5. Conclusions

(1) The solubility of chlorine in forsterite, enstatite and pyrope is very low, 0.2-0.7 ppm. The fluorine solubility reaches ~260 ppm in forsterite, 16-30 ppm in Al-bearing enstatite, and 24-52 ppm in pyrope. These solubilities are also independent of the fluid salinity and they indicate that intrinsic solubility limits have been reached over the entire range of salinity studied (up to 30 wt. % Cl). The fluid-mineral partition coefficient, D_{Cl} , ranges between 4.5×10^3 and 1.6×10^6 and is well represented by the power law, $D_{Cl} = 27860 X^{1.06}$ for the entire peridotite assemblage. The D_F increases from $8.4 \cdot 10^0$ to $5.8 \cdot 10^3$, then it becomes constant at ~6 wt. % F in the aqueous fluid. This is interpreted to result from invariant saturation with the hydrous fluoride (or fluorosilicate) melt.

(2) The solubilities of fluorine in forsterite and pyrope are broadly similar to hydroxyl solubilities. The consistent substitution mechanisms are the fluorination of vertices of oxygen polyhedra charge balanced by octahedral vacancies or other local chemical defects. By contrast, our measured fluorine solubilities in aluminous enstatite are more than 20 times lower than those of hydroxyl, suggesting that the $[\text{AlF}]^{2+}$ $[\text{SiO}]^{2+}$ substitution is not an efficient incorporation mechanism. The solubilities of chlorine are two to three orders of magnitude lower than those of fluorine and such behavior extends to silicate liquids where the solubility negatively correlates with the increasing ionic radius. The observed decrease in chlorine solubility is within permissible limits imposed by the lattice strain theory on element partitioning.

(3) The presence of fluorine in our experiments stabilizes minerals of the humite group at fluid salinities greater than 0.63 wt. % F. The molar $\text{F}/(\text{F}+\text{OH})$ ratios range from 0.42 to 0.61, and the exchange of OH and F between coexisting humite-group phases is ideal. The fluid-mineral partition coefficients, $1.3 \cdot 10^{-1}$ - $3.0 \cdot 10^0$, indicate that substantial portion of the fluorine budget can be stored in these phases and transported to Earth's deep interior, if they are stable along the subduction path. In addition, the humite group minerals can incorporate Ti, Zr, Nb and Ta into their structure (López-Sánchez-Vizcaíno 2005) thus indirectly affecting the HFSE cycle at convergent plate boundaries.

(4) The solubilities of H_2O and Cl in the nominally anhydrous minerals differ by three to four orders of magnitude. It is thus expected that progressive percolation of the aqueous fluid through the anhydrous peridotite assemblage will lead to gradual sequestration of H_2O , hence increasing fluid salinity. Incremental mass balance calculations demonstrate that the rock-fluid ratio of 1300-4000 is necessary to elevate the fluid salinity to the level required for the source region of primary arc melts, and that of 1400-6000 to produce saline brines found in high-pressure eclogites.

2.6. References

Aiuppa A., Baker D. R., Webster J. D. (2009): Halogens in volcanic systems, *Chemical Geology*, 263, 1-18.

Albaréde F. (1995): Introduction to geochemical modeling, *Cambridge University Press*.

Blundy J. D., Wood B. J. (1994): Prediction of crystal-melt partition coefficients from elastic moduli, *Nature*, 372, 452-454.

Blundy J. D., Wood B. J. (2003): Partitioning of trace elements between crystal and melts, *Earth and Planetary Science Letters*, 210, 383-397.

- Bromiley D., Kohn S. C. (2007): Comparisons between fluoride and hydroxide incorporation in nominally anhydrous and fluorine-free mantle minerals, *Goldschmidt Conference Abstracts*, A124.
- Bureau H., Keppler H. (1999): Complete miscibility between silicate melts and hydrous fluids in the upper mantle: experimental evidence and geochemical implications, *Earth and Planetary Science Letters*, 165, 187-196.
- Bonifacie M., Busigny V., Mével C., Philippot, Agrinier P, Jendrzejewski N., Scambelluri M., Javoy M. (2008): Chlorine isotopic composition in seafloor serpentinites and high-pressure metaperidotites. Insights into oceanic serpentinization and subduction processes, *Geochimica et Cosmochimica Acta*, 72, 126-139.
- Cervantes P., Wallace P. J. (2003): The role of H₂O in subduction-zone magmatism: new insights from melt inclusions in high-Mg basalts from central Mexico, *Geology*, 31, 235-238.
- Duffy C. J., Greenwood H. J. (1979): Phase equilibria in the system MgO-MgF₂-SiO₂-H₂O, *American Mineralogist*, 64, 1156-1173.
- Fukui H., Inoue T., Yasui T., Katsura T., Funakoshi K., Ohtaka O. (2005): Decomposition of brucite up to 20 GPa: evidence for high MgO-solubility in the liquid phase, *European Journal of Mineralogy*, 17, 261-267.
- Gao J., Klemd R., Zhang L., Wang Z., Xiao X. (1999): PóT path of high-pressure/low-temperature rocks and tectonic implications in the western Tianshan Mountains, NW China, *Journal of Metamorphic Geology* 17, 621-636.
- Icenhower J. P., London D. (1997): Partitioning of fluorine and chlorine between biotite and granitic melt: experimental calibration at 200 MPa H₂O, *Contributions to Mineralogy and Petrology*, 127, 17-29.
- Inoue T. (1994): Effect of water on melting phase relations and melt composition in the system Mg₂SiO₄-MgSiO₃-H₂O up to 15 GPa, *Physics of the Earth and Planetary Interior*, 85, 237-263.
- Ito E., Harris D., Anderson A. T. (1983): Alteration of oceanic crust and geologic cycling of chlorine and water, *Geochimica et Cosmochimica Acta*, 47, 1613-1624.
- Jarrard R. D. (2003): Subduction fluxes of water, carbon dioxide, chlorine and potassium, *Geochemistry Geophysics Geosystems*, 4, doi: 10.1029/2002GC000392.
- Johnson E. R., Wallace P. J., Granados H. D., Manea V. C., Kent A. J. R., Bindeman I. N., Donegan C. S. (2009): Subduction related volatile recycling and magma generation beneath central Mexico: Insights from melt inclusions, oxygen isotopes and geodynamic models, *Journal of Petrology*, 50, 1729-1764.

- Keppler H., Bolfan-Casanova N. (2006): Thermodynamics of water solubility and partitioning, *Reviews in Mineralogy and Geochemistry*, 62, 193-230.
- Kravchuk I. F., Keppler H. (1994): Distribution chlorides between aqueous fluids and felsic melts at 2 kbar and 800 °C, *European Journal of Mineralogy*, 6, 913-923.
- Kushiro I., Yoder H. S. Jr., Nishikawa M. (1968): Effect of water on the melting of enstatite, *Geological Society of America Bulletin*, 79, 1685-1692.
- Lu R., Keppler H. (1997): Water solubility in pyrope to 100 kbar, *Contributions to Mineralogy and Petrology*, 129, 35-42.
- Manning C. E., Bird D. K. (1990): Fluorian calcic garnets from the host rocks of the Skaergaard intrusion: implications for metamorphic fluid composition, *American Mineralogist*, 75, 859-873.
- Manning, C. E. (2004): The chemistry of subduction-zone fluids. *Earth and Planetary Science Letters*, 223, 1-16.
- McDonough W. F., Sun S.-S. (1995): The composition of the Earth, *Chemical Geology*, 120, 223-253.
- Melekhova E., Schmidt M. W., Ulmer P., Pettke T. (2007): The composition of liquids coexisting with dense hydrous magnesium silicates at 11-13.5 GPa and the endpoints of the solidi in the MgO-SiO₂-H₂O system, *Geochimica et Cosmochimica Acta*, 71, 3348-3360.
- Métrich N., Rutherford M. J. (1992): Experimental study of chlorine in hydrous silicic melts, *Geochimica et Cosmochimica Acta*, 56, 607-616.
- Mierdel K., Keppler H., Smyth J. R., Langenhorst F. (2007): Water solubility in aluminous orthopyroxene and the origin of the Earth's asthenosphere, *Science*, 315, 364-368.
- Mookherjee M., Karato S. (2010): Solubility of water in pyrope rich garnet at high pressures and temperature, *Geophysical Research Letters*, 37, doi 10.1029/2009GL041289.
- Mosenfelder J. L., Deligne N. I., Asimow P. D., Rossman G. R. (2006): Hydrogen incorporation in olivine from 2-12 GPa, *American Mineralogist*, 91, 285-294.
- Newsom H.E (1995): Composition of the solar system, planetes, meteorites, and major terrestrial reservoirs, *Global Earth Physics: A Handbook of Physical Constants*, American Geophysical Union, Washington, 1, 159-189.
- Orberger B., Métrich N., Mosbah M., Mével C., Fouquet Y. (1999): Nuclear microprobe analysis of serpentine from the mid-atlantic ridge, *Nuclear Instruments and Methods in Physics Research B*, 158, 575-581.
- Rauch M., Keppler H. (2002): Water solubility in orthopyroxene, *Contributions to Mineralogy and Geochemistry*, 143, 525-536.

- Rice J. M., (1980): Phase Equilibria Involving Humite Minerals in Impure Dolomitic Limestones Part I. Calculated Stability of Clinohumite, *Contributions to Mineralogy and Petrology*, 71, 219-235.
- Rice J. M., (1981): Phase Equilibria Involving Humite Minerals in Impure Dolomitic Limestones Part II: Calculated Stability of Chondrodite and Norbergite, *Contributions to Mineralogy and Petrology*, 75, 205-223.
- Scambelluri M., Philippot P. (2001): Deep fluids in subduction zones, *Lithos*, 55, 213-227.
- Scambelluri M., Müntener O., Ottolini L., Pettke T. T., Vannucci R. (2004): The fate of B, Cl and Li in the subducted oceanic mantle and in the antigorite breakdown fluids, *Earth and Planetary Science Letters*, 222, 217-234.
- Shannon R. D. (1976): Revised effective ionic radii and systematic studies of interatomic distances in halides and chalcogenides, *Acta Crystallographica A*, 32, 751-767.
- Schilling J. G., Unni C. K., Bender M. L. (1978): Origin of chlorine and bromine in the oceans, *Nature*, 273, 631-636.
- Smyth J. R. (1981): Halogen and phosphorus storage in the Earth, *Nature* 289, 762-765.
- Smyth J. R., Delaney J. S., Hervig R. L., Dawson J. B. (1981): Storage of F and Cl in the upper mantle: geochemical implications, *Lithos* 14, 133-147.
- Smyth J. R., Madel R. E., McCormick T. C., Monuz J. L., Rossman G. R. (1990): Crystal-structure refinement of a F-bearing spessartine garnet, *American Mineralogist*, 75, 314-318.
- Smyth J. R., Frost D. J., Nestola F., Holl C. M., Bromiley G. (2006): Olivine hydration in the deep upper mantle: effect of temperature and silica activity, *Geophysical Research Letters*, 33, doi: 10.1029/2006GL026194.
- Straub S. M., Layne G. D. (2003): The systematic of chlorine, fluorine, and water in Izu arc front volcanic rocks: implications for volatile recycling in subduction zone, *Geochimica et Cosmochimica Acta*, 21, 4179-4203.
- Sumita T., Inoue T. (1996): Melting experiments and thermodynamic analyses on silicate-H₂O systems up to 12 GPa, *Physics of the Earth and Planetary Interiors*, 96, 187-200.
- Valley J. W., Essene E. J., Peacor D. R. (1983): Fluorine-bearing garnets in Adirondack calc-silicates, *American Mineralogist*, 68, 444-448.
- Visser D. (1993): Fluorine-bearing hydrogarnets from Blengsvatn, Bamble sector, south Norway, *Mineralogy and Petrology*, 47, 209-218.
- Wallace P. J. (2005): Volatiles in subduction zone magmas; concentrations and fluxes based on melt inclusion and volcanic gas data, *Journal of Volcanology and Geothermal Research*, 140, 217-240.

- Webster J. D. (1990): Partitioning of F between H₂O and CO₂ fluids and topaz rhyolite melt implication for mineralizing magmatic-hydrothermal fluids in F-rich granitic system, *Contributions to Mineralogy and Petrology*, 104, 424-438.
- Webster J. D. (1992): Fluid-melt interactions involving Cl-rich granites: experimental study from 2 to 8 kbar, *Geochimica et Cosmochimica Acta*, 56, 679-687.
- Wei W., Kastner M., Spivack A. (2008): Chlorine isotopes and halogen concentrations in convergent margins with implications for the Cl isotopes cycle in the ocean, *Earth and Planetary Science Letters*, 266, 90-104.
- Wiedenbeck M., Rhende D., Lieckefett R., Witzki H. (2004): Cryogenic SIMS and its applications in the Earth sciences, *Applied Surface Science*, 231-232, 888-892.
- Yamada A., Inoue T., Irifune T. (2004): Melting of enstatite from 13 to 18 GPa under hydrous conditions, *Physics of the Earth and Planetary Interiors*, 147, 45-56.

3. Solubility of fluorine in forsterite to very high pressures: a first principles computational study

3.0. Abstract

I have investigated the solubility of fluorine in forsterite along the $\text{Mg}_2\text{SiO}_4\text{-MgF}_2$ join in order to constrain halogen storage during breakdown of humite-group minerals in the peridotitic upper mantle. By using first-principles computations, I have determined the pressure-volume equations of state, ground-state energetics and mixing properties of orthorhombic $\text{Mg}_2\text{SiO}_4\text{-Mg}_2\text{F}_4$ solutions, fluorine-bearing end-members of the humite group, and sellaite. The molar volumes at various pressures up to 14 GPa were fitted by a third order Birch-Murnaghan equation of state. In the generalized gradient approximation (GGA), forsterite has a bulk modulus, $K_0 = 119.4 \pm 1.6$ GPa and its pressure derivative, $K_0' = 3.73 \pm 0.03$. Both properties change nearly linearly as fluorine is substituted into the forsterite structure by $[\text{SiO}_4]^{4-} \leftrightarrow [\text{F}_4]^{4-}$. The metastable orthorhombic Mg_2F_4 has $V_0 = 41.9 \pm 0.1 \text{ cm}^3 \text{ mol}^{-1}$, $K_0 = 60.9 \pm 1.5$ GPa and $K_0' = 4.34 \pm 0.07$, which makes it by *ca.* 3 % bigger and 39 % more compressible than the stable MgF_2 (sellaite), $V_0 = 20.25 \pm 0.02 \text{ cm}^3 \text{ mol}^{-1}$, $K_0 = 84.5 \pm 1.5$ GPa and $K_0' = 4.0 \pm 0.2$. Energies of mixing at ground state along the $\text{Mg}_2\text{SiO}_4\text{-Mg}_2\text{F}_4$ binary with orthorhombic structure are weakly negatively non-ideal and show tendency by $-8.03 \text{ kJ mol}^{-1}$ toward ordering of silicate tetrahedra and fluorine quadruplets at the centre of the binary join. The mixing properties are successfully reproduced by a symmetric binary solution between forsterite, $\text{Mg}_4[\text{SiO}_4]_2$, and an intermediate compound, $\text{Mg}_4[\text{SiO}_4]\text{F}_4$, with excess mixing energy of $6.8 \pm 1.0 \text{ kJ mol}^{-1}$. Energy calculations indicate that the humite-group phases are by $7.3\text{-}14.0 \text{ kJ mol}^{-1} \text{ atom}^{-1}$ more stable than the orthorhombic solid solution and hence act as buffers that dictate the maximum fluorine solubility in forsterite. Using ground-state enthalpies and configurational entropies, the solubilities of fluorine in forsterite buffered by humite-group minerals were calculated as function of pressure and temperature. The fluorine solubility sharply increases with temperature, from 0.01 ppm at 500 K up to 0.34 wt. % at 1900 K. By contrast, the effect of pressure is small, leading to a decrease in solubility by factor of two to three as pressure rises from 0 to 12 GPa. All calculations were verified by simulations in the local density approximation (LDA) and yielded concentration differences smaller than half a logarithmic unit over an investigated range of seven orders of magnitude. During devolatilization reactions in the subducting slab, fluorine is expected to partition preferentially to aqueous fluids (or silicate melts) but when these media pass through the mantle wedge, the partition coefficients are expected to decrease, and a portion of the fluorine budget will become incorporated and stored

in the mantle peridotites. The strong progressive temperature dependence of fluorine solubility, predicted in this study, thus promotes mantle metasomatism in the high-temperature and low-pressure regions beneath arcs.

3.1. Introduction

Subduction zone elemental fluxes provide important insights into the partitioning of elements during slab metamorphism and dehydration, that is, the proportions which are subducted into deeper Earth's interior or are returned through arc magmatism to the lithosphere or atmosphere. For halogens, which are frequently incorporated in hydroxyl-bearing silicates and phosphates, the subduction component in arc outflux varies substantially, 93 % for Cl and ~50 % for F of the total amount (Straub and Layne 2003). As a consequence, about half of the fluorine budget has a mantle origin but mechanisms of its incorporation and transport are not understood. Preliminary experiments in the forsterite-sellaite (MgF_2) binary at 1350-1600 °C and 1-2 GPa revealed solubility of fluorine in forsterite up to 0.45 wt. % (Bromiley and Kohn 2007) although these authors reported presence of sellaite or clinohumite lamellae in the forsterite. The potentially high fluorine solubility in nominally anhydrous minerals in the mantle has implications for location of dehydration reactions, e.g., breakdown of serpentine, humite-group phases and other hydrous magnesium silicates, stability of apatite, and could also explain the low proportion of the fluorine subduction component in arc magmas found by Straub and Layne (2003).

In this study I investigate the energetics and solubility of fluorine in forsterite by first principles computations. Our calculations provide pressure-volume equations of state for forsterite- Mg_2F_4 solid solutions, humite-group minerals, and sellaite (MgF_2) as well as non-ideal solution properties. In turn, these are utilized to calculate the fluorine solubility in forsterite at temperature up to 1800 K and pressure of 20 GPa, and discuss the storage capacity and redistribution of halogens in the upper mantle at convergent plate boundaries.

3.2. Crystal chemistry of fluorine-bearing magnesium silicates

Magnesium silicates with hydroxyl or fluorine groups encompass the ternary composition space $\text{MgO-SiO}_2\text{-H}_2\text{O}$ (F_2O_{-1}) (Yamamoto and Akimoto 1977, Wunder and Schreyer 1997, Smyth 2006, Frost 2006, Kawamoto 2006). Within this ternary, forsterite is colinear with minerals of the humite-group (clinohumite, humite, chondrodite, and norbergite), along the forsterite-sellaite (MgF_2) binary.

Forsterite has orthorhombic symmetry (Pbnm, Birle et al. 1968) in which oxygen atoms define a nearly hexagonal close packing arranged around [100] in which half of the octahedral

sites are occupied by Mg and one eighth of the tetrahedral sites are occupied by Si. The $(\text{MgO}_6)^{-10}$ octahedra are connected by sharing edges, forming chains along [001], whereas $(\text{SiO}_4)^{-4}$ tetrahedra are intercalated between chains of octahedra. Sellaite (MgF_2) has tetragonal rutile structure, and this difference is expected to limit the extent of fluorine substitution in forsterite. Magnesium fluoride consists of a distorted hexagonal packing of fluorine atoms, whereby $(\text{MgF}_6)^{-4}$ octahedra are very nearly regular and form chains parallel to the [001] by sharing edges (Strunz and Nickel, 2001).

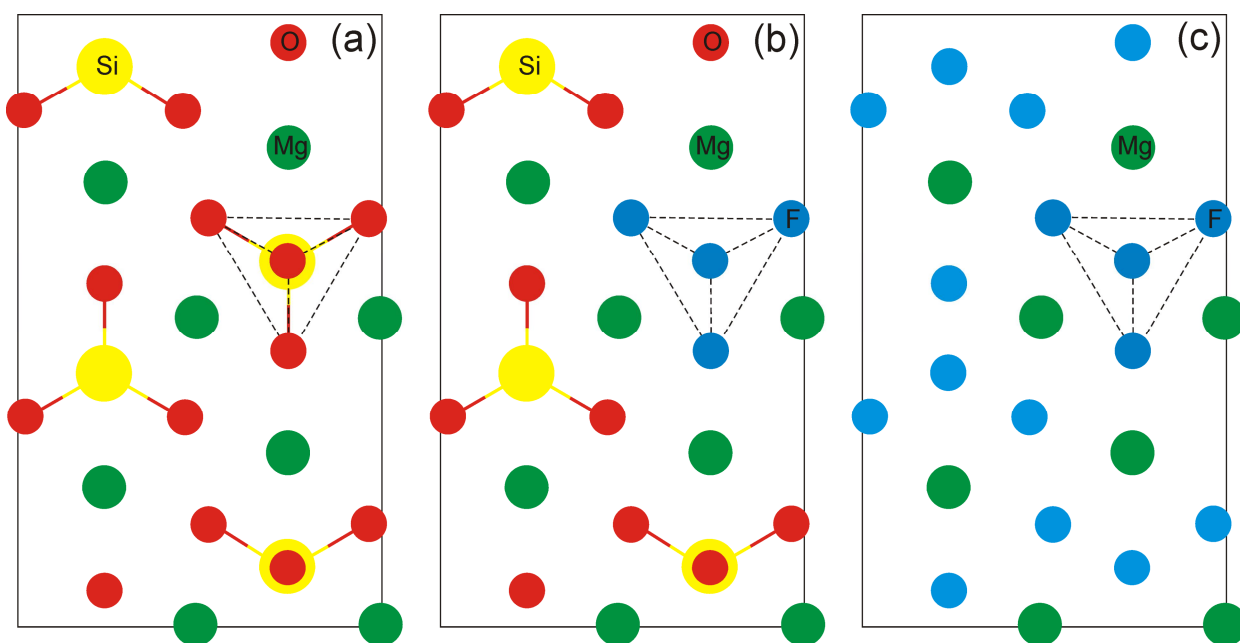


Fig. 3-1. Schematic representation of crystal structures of forsterite (a), orthorhombic F-doped forsterite (f250) (b) and orthorhombic Mg_2F_4 (f1000) (c). Green circles represent Mg atoms; yellow circles represent Si atoms; red circles represent O atoms and blue circles represent F atoms. Structures are oriented perpendicular to a-axis. The incorporation mechanism of F via Si vacancy is represented in (b): an $[\text{F}_4]^{-4}$ quadruplet substitutes for an $[\text{SiO}_4]^{-4}$ group in the forsterite structure. All crystal structures have the spatial group Pbnm.

Along the Mg_2SiO_4 - MgF_2 join, the F incorporation in forsterite can be described by the equilibrium:



This silicon-vacancy substitution mechanism involves the replacement of an $(\text{SiO}_4)^{-4}$ group by a $(\text{F}_4)^{-4}$ quadruplet in the crystal structure (Fig. 3-1). This has already been proposed for

fluorine incorporation in calcic and magnesian garnets (Valley et al. 1983, Smyth et al. 1990, Visser 1993) and explored in preliminary experiments using forsterite (Bromiley and Kohn 2007).

In the forsterite-sellaite binary, several intermediate phases are potentially stable: clinohumite, humite, chondrodite, and norbergite, and these are prospective fluorine hosts in peridotites, serpentinites and kimberlites (Möckel 1969, McGetchin and Silver 1970, Trommsdorff and Evans 1980, Evans and Trommsdorff 1983, Dymek et al. 1988, López Sánchez-Viscaino et al 2005). Fluorine-bearing end-members of the humite group have general formula $n \text{Mg}_2\text{SiO}_4 \cdot \text{MgF}_2$, where n ranges from 1 to 4 (Tab. 3-1).

The crystal structures of humite group minerals are defined by alternating $2n$ forsterite layers and brucite double sheets (Mg_2F_4) along [100] plane (Taylor and West 1928). All phases in the humite group have a pseudo-hexagonal close packing of O, OH, F arranged in a pseudo-hexagonal pattern around [010] forming chains of edge-sharing octahedra are parallel to a -axis. Tetrahedral sites are occupied by $(\text{SiO}_4)^{4-}$ groups or $(\text{OH},\text{F})_4^{4-}$ anions, thus defining substitution $(\text{SiO}_4)^{4-} \leftrightarrow (\text{F}_4)^{4-}$. Fundamentally, fluorine quadruplets and silicate anions are expected to be randomly distributed in the forsterite structure whereas in the humite group phases, they are preferentially ordered into sheets. The energetic difference between these two arrangements dictates, by applying standard thermodynamic relations, the permissible solubility of fluorine in forsterite.

Tab. 3-1. Composition and crystallographic data of magnesium silicates and fluoride.

Mineral	n	Chemical formula	Space group	a (Å)	b (Å)	c (Å)	β °	Z	Ref.
forsterite		Mg_2SiO_4	$Pbnm$	4.76	10.23	5.99		4	1
clinohumite	4	$\text{Mg}_8\text{Si}_4\text{O}_{16}(\text{OH},\text{F})_2$	$P2_1/c$	13.66	4.74	10.25	100.8	2	2
humite	3	$\text{Mg}_7\text{Si}_3\text{O}_{12}(\text{OH},\text{F})_2$	$Pm\bar{c}n$	20.85	4.74	10.26		4	3
chondrodite	2	$\text{Mg}_5\text{Si}_2\text{O}_8(\text{OH},\text{F})_2$	$P2_1/c$	7.84	4.73	10.25	109.1	2	4
norbergite	1	$\text{Mg}_3\text{SiO}_4(\text{OH},\text{F})_2$	$Pbmn$	8.75	4.71	10.27		4	5
sellaite		MgF_2	$P4_2/mnm$	4.62		3.05		2	6

References: 1 - Birle et al. (1968), 2 - Robinson et al. (1973), 3 - Ribbe and Gibbs (1971), 4 - Gibbs et al. (1970), 5 - Gibbs and Ribbe (1969), 6 - Baur (1976).

3.3. Computational method

I perform first-principles calculations based on density functional theory (Hohenberg and Kohn 1964, Kohn and Sham 1965). Simulations have been carried out using the Vienna *Ab Initio* Simulation Package (VASP; Kresse and Furthmüller 1996a,b). Two widely used approximations have been used to describe the exchange-correlation functional: the local density approximation (LDA) and the generalized gradient approximation (GGA). In all cases, I employ ultra-soft pseudopotentials (Kresse and Hafner 1994). Cut-off energy chosen for the calculations is 600 eV and break conditions for the self-consistent ionic and electronic relaxation loop were 10^{-8} and 10^{-7} ,

respectively. The structures were completely relaxed to the most energetically favorable configurations for all end-member and solution phases at static conditions. After the relaxed structures were obtained, a series of simulations with compressed and expanded volumes was carried out for each phase in order to constrain the pressure-volume relations. Volumes used to constrain the pressure-volume relations ranged from *ca.* 110 to 65 % of the relaxed value; in several cases the range was decreased (from *ca.* 110 to 80 %) in order to avoid unstable behavior of the structure at high pressure.

Internal energies were calculated from the Kohn-Sham equation (Kohn and Sham 1965), which includes contributions from the electronic kinetic energy, nucleus-nucleus and nucleus-electron interaction potential energy, Coulombic electron interaction and exchange-correlation potential energy. The Kohn-Sham equations are exact, but the functional form of the potential due to exchange and correlation is not known. The exchange-correlation potential has been solved by local density approximation (LDA), where the exchange and correlation energy is taken to be analogous to that of homogeneous electron gas with the same density, and by the generalized gradient approximation (GGA), in which the exchange-correlation term is treated as a function of the charge density gradient (Perdew et al. 1996). The LDA performs remarkably well for a wide variety of crystal structures; nevertheless it tends to overestimate the density (overbinding effect). By contrast, GGA significantly improves the description of the core (and to some extent the valence) electrons, therefore simulation energy differences and reaction barriers are remarkably improved (Oganov et al. 2002). Measured experimental volumes always fit between those simulated by LDA (lower boundary) and GGA (upper boundary); therefore both approximations were used to investigate *P-V* relations of the simulated phases. Despite that the GGA overestimates bond lengths, energy values appear to be more reliable (Oganov et al. 2002). Therefore, GGA has been taken as our preferred approximation.

Thermodynamic properties were obtained from internal energies by applying standard thermodynamic relationships. Pressure in each simulation was calculated from the stress-tensor retrieved by the total force (*F*):

$$F = \frac{dU}{dr} \quad (3-2)$$

where *U* and *r* are the internal energy and the atomic position, respectively. The enthalpy (*H*) at pressure (*P*) of interest was calculated as follows:

$$H = U + PV \quad (3-3)$$

where V is the volume. The simulation conditions for end-member solid phases are summarized in Table 3-2. A set of nine solution compounds with 28 to 111 atoms per box in the $\text{Mg}_2\text{SiO}_4\text{-Mg}_2\text{F}_4$ binary, including a hypothetical Mg_2F_4 end-member with forsterite structure, were generated (Eq. 3-1; Table 3-3). Note that substitution of two fluorine quadruplets for silicate tetrahedra creates three different configuration but replacement of one or three of the four silicate tetrahedra in the forsterite unit cell does not create multiple possible configurations.

Table 3-2. Simulation conditions for end-member solids

Symbol	Phase	Mole fraction Mg_2F_4	Number of atoms per box	Atoms per formula unit	Supercell	k -point grid
Fo	forsterite	0	28	7	1×1×1	4 4 4
Chu	clinohumite	0.111	62	31	1×1×1	2 2 2
Hum	humite	0.143	96	24	1×1×1	2 2 2
Chn	chondrodite	0.2	34	17	1×1×1	2 2 2
Nrb	norbergite	0.333	40	10	1×1×1	2 2 2
Sel	sellaite	1	6	3	1×1×1	4 4 4

Table 3-3. Simulation conditions for forsterite- Mg_2F_4 solid solution compounds (Pbnm)

Symbol	Mole fraction Mg_2F_4	Number of atoms per box	Atoms per formula unit	Supercell	k -point grid
Fo	0	28	7	1 × 1 × 1	4 4 4
f063	1/16	111	6.94	2 × 2 × 1	2 2 2
f083	1/12	83	6.92	3 × 1 × 1	2 2 4
f125	1/8	55	6.89	2 × 1 × 1	2 2 4
f250	1/4	27	6.75	1 × 1 × 1	4 4 4
f500	2/4	26	6.5	1 × 1 × 1	4 4 4
f750	3/4	25	6.25	1 × 1 × 1	4 4 4
f875	7/8	49	6.13	2 × 1 × 1	4 4 4
f917	11/12	73	6.08	3 × 1 × 1	2 2 2
f938	15/16	97	6.06	2 × 2 × 1	2 2 2
f1000	4/4	24	6	1 × 1 × 1	4 4 4

3.3. Results

3.3.1. Pressure-volume relations at static conditions

Molar volumes of relaxed cells and at a stepwise compression to are listed in Table 3-A1 and shown in Fig. 3-2. The volumes obtained by GGA and LDA differ systematically by 6 to 11 %. Due to their respective under- and overbonding effect, these two approaches bracket the volumetric properties determined experimentally at ambient conditions.

Using the GGA, the molar volumes in the system $\text{Mg}_2\text{SiO}_4\text{-Mg}_2\text{F}_4$ relaxed under static conditions increase from 6.36 to 7.02 $\text{cm}^3 \text{mol}^{-1} \text{atom}^{-1}$. The molar volumes of the forsterite- Mg_2F_4 solution vary nearly linearly with composition but solution compounds f875 and f917 show negative deviations by 0.05 and 0.03 $\text{cm}^3 \text{mol}^{-1} \text{atom}^{-1}$ from the ideal mixing behavior. The calculated volumetric Margules parameter for the solid solution (when f875 and f917 are

excluded) is negligibly small, $-0.02 \text{ cm}^3 \text{ mol}^{-1} \text{ atom}^{-1}$, and it will not be considered in subsequent thermodynamic calculations.

Molar volumes of the minerals of the humite group are lower than those of the corresponding solid solutions. The magnitude of this difference increases with the Mg_2F_4 fraction, the difference in molar volume is $0.02 \text{ cm}^3 \text{ mol}^{-1} \text{ atom}^{-1}$ (-0.3 %) for clinohumite, $0.03 \text{ cm}^3 \text{ mol}^{-1} \text{ atom}^{-1}$ (-0.4 %) for humite, $0.08 \text{ cm}^3 \text{ mol}^{-1} \text{ atom}^{-1}$ (-1.2 %) for chondrodite and $0.10 \text{ cm}^3 \text{ mol}^{-1} \text{ atom}^{-1}$ (-1.5 %) for norbergite. Sellaite has a difference in molar volume compared to the f1000 compound of $0.28 \text{ cm}^3 \text{ mol}^{-1} \text{ atom}^{-1}$ (-4.1 %). Since the molar volumes of the humite-group minerals are always smaller than those of the orthorhombic solid solution (Fig. 3-2), this implies that increasing pressure will destabilize fluorine-bearing forsterite and cause a decrease in fluorine solubility.

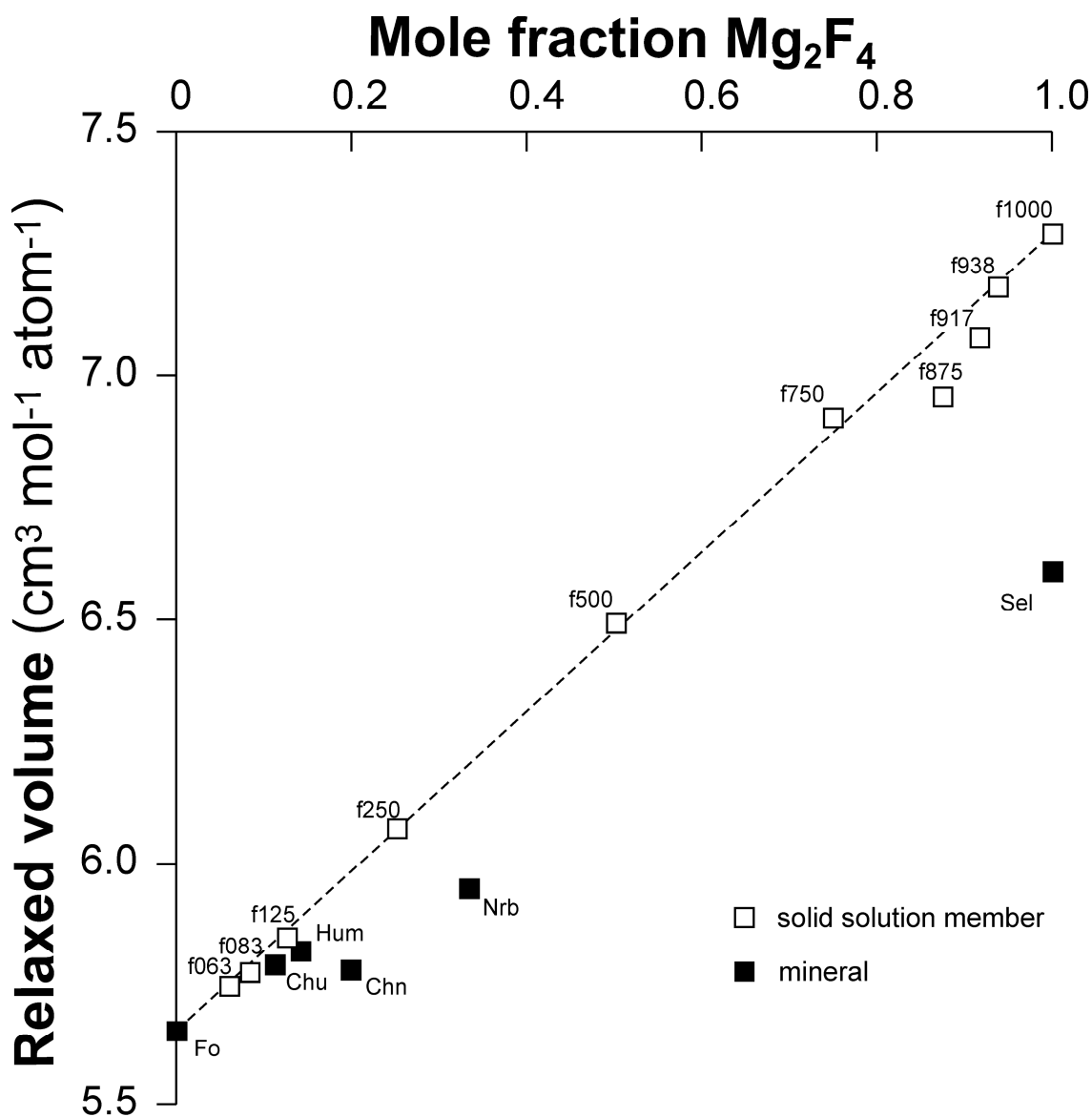


Fig. 3-2. Relaxed volumes of solid solution compounds vs. Mg_2F_4 mole fraction.

I have used the third order Birch-Murnaghan equation of state to fit the pressure-volume results for each phase or solution composition (Murnaghan 1937, Birch 1947, Angel 2000):

$$P = \frac{3}{2}K_0 \left[\left(\frac{V_0}{V} \right)^{\frac{7}{3}} - \left(\frac{V_0}{V} \right)^{\frac{5}{3}} \right] \left\{ 1 - \frac{3}{4}(4 - K_0') \left[\left(\frac{V_0}{V} \right)^{\frac{2}{3}} - 1 \right] \right\} \quad (3-4)$$

where V_0 , K_0 and K_0' are molar volume, bulk modulus and its pressure derivative respectively at a reference pressure of 0 GPa. The equation of state parameters are listed in Tables 3-4 and 3-5 and they are graphically shown in Fig. 3-3 and 3-4.

Sellaite has V_0 of $20.25 \pm 0.02 \text{ cm}^3 \text{ mol}^{-1}$, a K_0 of $84.32 \pm 1.5 \text{ GPa}$ and K_0' value of 3.98 ± 0.2 . The bulk moduli of the orthorhombic forsterite- Mg_2F_4 solutions decrease nearly linearly from 119.43 (forsterite) to 60.90 GPa (Mg_2F_4). By contrast, K_0' values increase almost linearly from 3.73 (forsterite) to 4.34 (Mg_2F_4). The humite-group minerals exhibit a similar trend; their bulk moduli decrease in a monotonous manner from 113.7 to 106.4 GPa for clinohumite through norbergite, respectively, and pressure derivatives of the bulk modulus range between 3.80 and 4.01. Despite the small differences in bulk moduli between the forsterite- Mg_2F_4 solid solution and the humite-group phase, the volumes of the latter remain smaller within the whole investigated pressure range. This implies that the humite minerals become progressively more stable with increasing pressure than the corresponding orthorhombic solid solution.

Table 3-4. Volumetric properties (per formula unit) of end-member solids at static conditions

	GGA			LDA		
	V_0 ($\text{cm}^3 \text{ mol}^{-1}$)	K_0 (GPa)	K_0'	V_0 ($\text{cm}^3 \text{ mol}^{-1}$)	K_0 (GPa)	K_0'
Fo	44.48 ± 0.07	119.43 ± 1.6	3.73 ± 0.03	41.76 ± 0.08	130.52 ± 2.5	3.68 ± 0.06
Chu	198.74 ± 0.17	113.69 ± 1.6	3.80 ± 0.08	185.41 ± 0.04	125.94 ± 0.3	3.89 ± 0.03
Hum	154.17 ± 0.04	109.84 ± 0.4	4.01 ± 0.03	143.75 ± 0.03	124.95 ± 0.2	3.97 ± 0.03
Chn	109.06 ± 0.02	109.80 ± 0.3	4.01 ± 0.03	101.66 ± 0.04	124.66 ± 0.4	3.94 ± 0.06
Nrb	64.87 ± 0.02	106.43 ± 0.5	3.93 ± 0.04	60.30 ± 0.01	120.72 ± 0.1	3.85 ± 0.02
Sel	20.25 ± 0.02	84.32 ± 1.5	3.98 ± 0.15	18.41 ± 0.01	105.31 ± 0.6	3.74 ± 0.10

Table 3-5. Volumetric properties (per formula unit) of solution compounds at static conditions

	GGA			LDA		
	V_0 ($\text{cm}^3 \text{ mol}^{-1}$)	K_0 (GPa)	K_0'	V_0 ($\text{cm}^3 \text{ mol}^{-1}$)	K_0 (GPa)	K_0'
f063	44.37 ± 0.05	115.08 ± 1.1	3.77 ± 0.02	41.50 ± 0.04	128.30 ± 1.2	3.67 ± 0.03
f083	44.31 ± 0.05	114.41 ± 1.2	3.76 ± 0.03	41.42 ± 0.04	127.28 ± 1.1	3.69 ± 0.03
f125	44.23 ± 0.04	111.69 ± 0.9	3.79 ± 0.02	41.30 ± 0.04	125.19 ± 1.1	3.69 ± 0.03
f250	44.06 ± 0.04	105.70 ± 0.8	3.76 ± 0.02	41.02 ± 0.03	118.12 ± 0.9	3.70 ± 0.02
f500	43.53 ± 0.05	93.03 ± 1.0	3.79 ± 0.03	40.23 ± 0.04	104.97 ± 1.0	3.73 ± 0.03
f750	42.87 ± 0.07	78.55 ± 1.2	3.90 ± 0.04	39.15 ± 0.03	91.36 ± 0.7	3.86 ± 0.04
f875	42.17 ± 0.04	69.31 ± 1.0	4.17 ± 0.13	38.13 ± 0.02	84.00 ± 0.3	4.45 ± 0.07
f917	41.92 ± 0.08	68.75 ± 1.9	4.11 ± 0.25	37.90 ± 0.01	82.12 ± 0.3	4.26 ± 0.03
f938	42.08 ± 0.07	62.37 ± 1.4	4.51 ± 0.11	37.82 ± 0.02	80.83 ± 0.7	4.21 ± 0.06
f1000	41.85 ± 0.10	60.86 ± 1.5	4.34 ± 0.07	37.42 ± 0.03	78.03 ± 0.8	4.31 ± 0.05

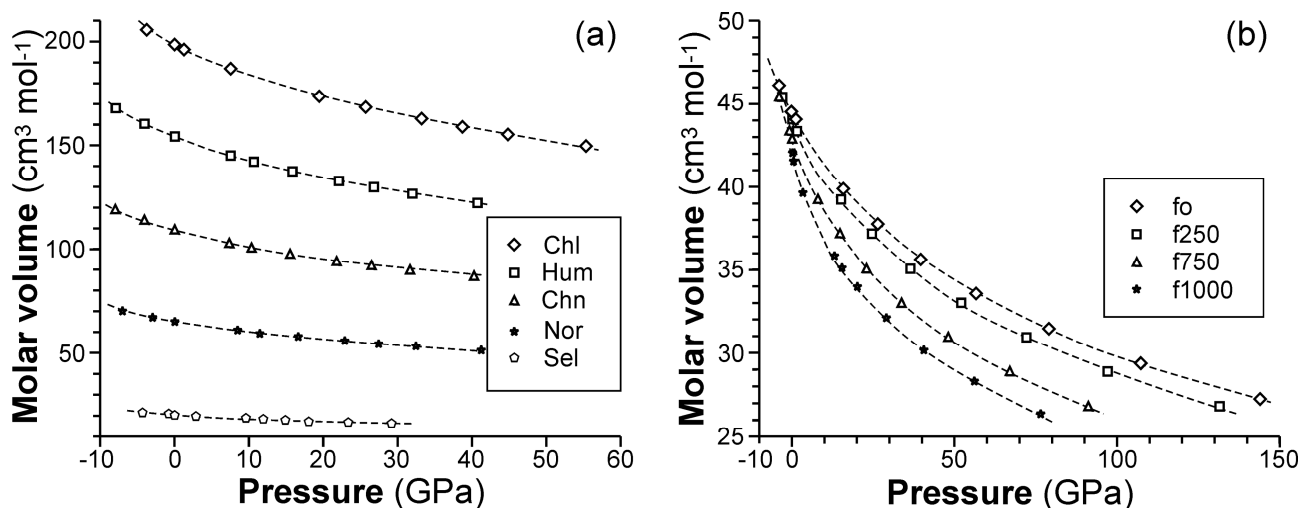


Fig. 3-3. Variation of molar volume (per formula unit) with pressure at $T = 0$ K for minerals (a) and solid solution compounds (b) as calculated using the GGA.

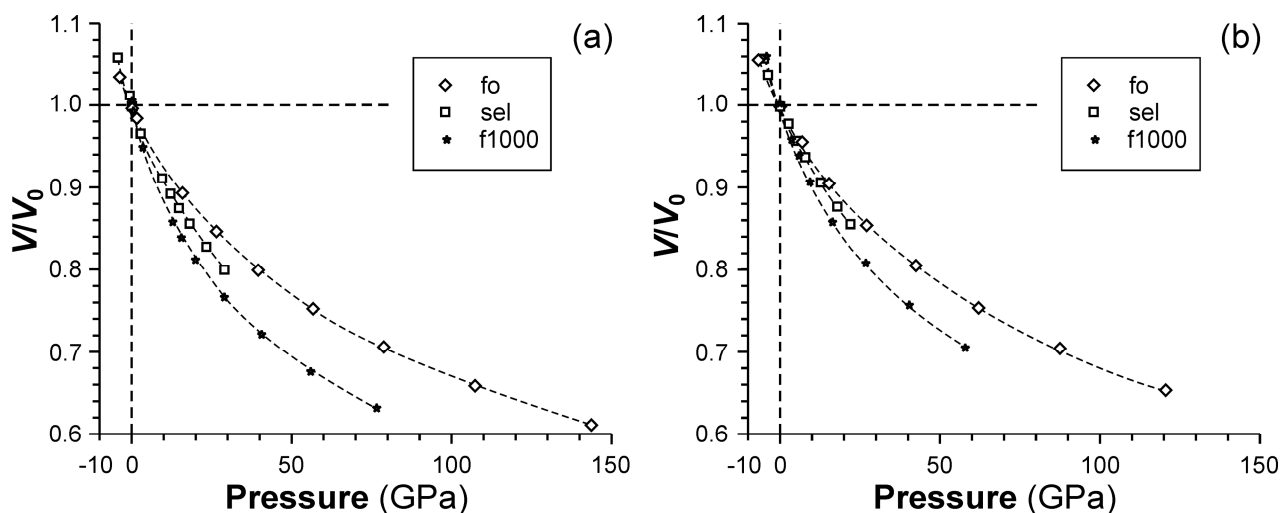


Fig. 3-4. Variation in reduced molar volume (V/V_0) with pressure for forsterite, sellaite and orthorhombic magnesium fluoride (f1000) calculated by GGA (a) and LDA (b).

3.3.2. Internal energy and enthalpy at static conditions

The internal energies of the Mg_2SiO_4 - Mg_2F_4 solid solutions and of the humite-group minerals at static conditions and $P = 0$ GPa are listed in Table 3-6 and illustrated in Fig. 3-5. The difference between internal energy for sellaite and orthorhombic Mg_2F_4 is $24.03 \text{ kJ mol}^{-1}$, whereby sellaite is more stable. For the Mg_2SiO_4 - Mg_2F_4 solid solutions, internal energies decrease with increasing mole fraction of Mg_2F_4 monotonously from 63.36 to $44.43 \text{ kJ mol}^{-1} \text{ atom}^{-1}$. The internal energies of the humite-group minerals are $3\text{-}8 \text{ kJ mol}^{-1} \text{ atom}^{-1}$ lower than those of corresponding orthorhombic solid solutions. Consequently, the humite-group minerals are expected to be more stable, and equilibria may be written with them as buffers to calculate fluorine solubility in forsterite.

Table 3-6. Internal energies of end-members (per formula unit) in the ground state and those of formation from oxides and magnesium fluoride.

Phase	U (kJ mol ⁻¹)	ΔfU (kJ mol ⁻¹)
Fo	-4682.37	-51.55
Clh	-20295.45	-226.92
Hum	-15615.35	-177.66
Chn	-10922.91	-116.04
Nor	-6242.26	-66.22

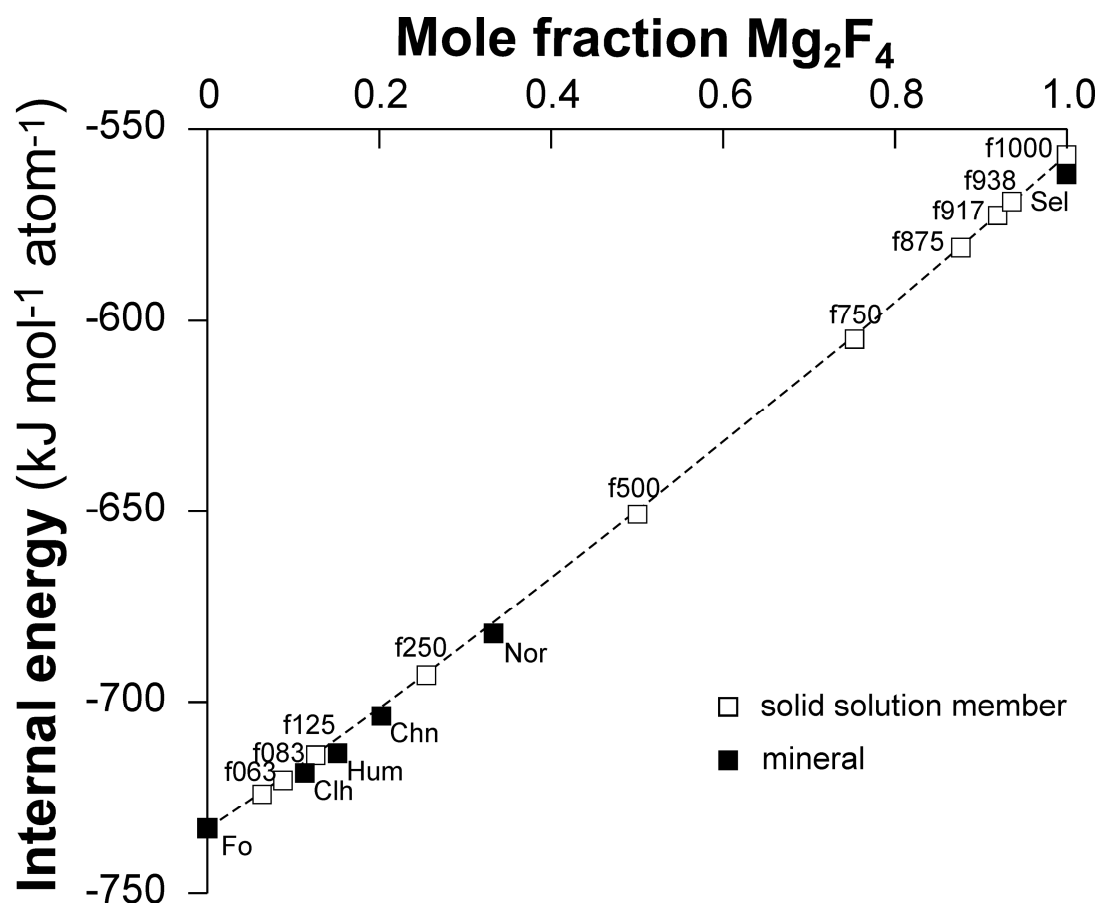


Fig. 3-5. Internal energy vs. composition diagram at $T = 0$ K and $P = 0$ GPa.

3.3.3. Thermodynamic mixing properties

Mixing energies of the orthorhombic Mg_2SiO_4 - Mg_2F_4 solutions show negative deviations from ideal mixing (Table 3-7, Fig. 3-6). The deviations are not consistent with symmetric or asymmetric excess polynomial but exhibit a pronounced minimum (-8.03 kJ per mole of end-members) in the centre of the join, $Mg_4[SiO_4]F_4$, suggesting ordering of silicate tetrahedra and fluoride quadruplets in the orthorhombic structure. Therefore, it is more appropriate to treat the solution as two separate binaries with two independent Margules parameters. The internal energies in the Mg_4SiO_8 - $Mg_4[SiO_4]F_4$ space were fitted to obtain a symmetric Margules parameter, $W = 6.8 \pm 1.0$ kJ mol⁻¹.

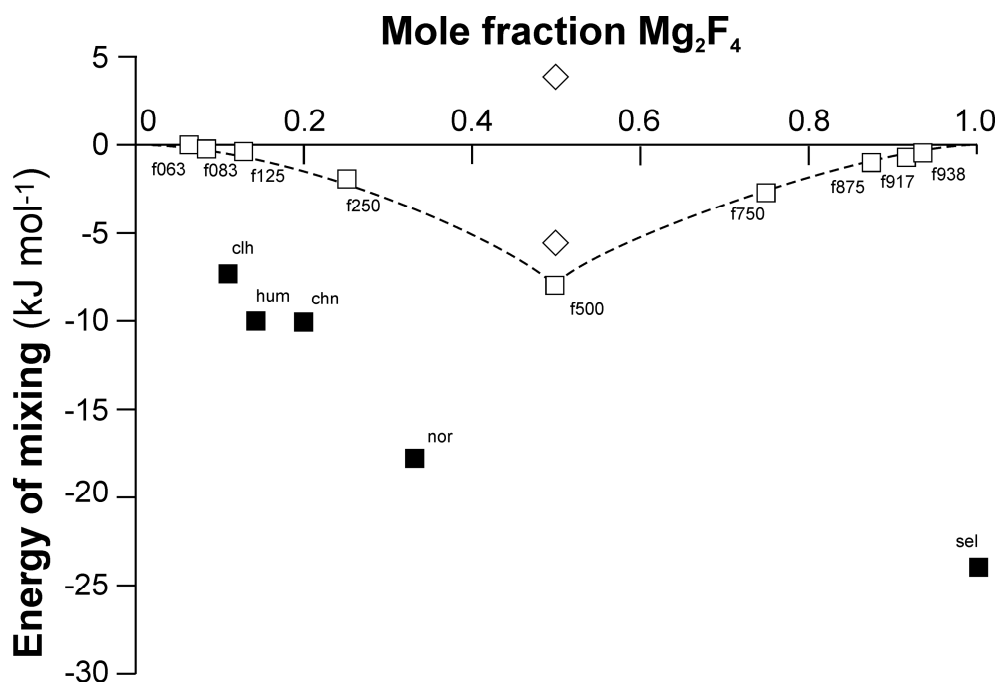


Fig. 3-6. Mixing energies (per mole of end-members) for orthorhombic solid solutions (open squares). Energies of the humite-group minerals are also shown for comparison (solid squares). Open diamonds indicate relaxed energy of less favorable configurations of f500.

Table 3-7. Internal energies (per formula unit) and energies of formation (from one mole of end-members) at $T = 0$ K and $P = 0$ GPa.

Phase	Mole fraction of Mg_2F_4	U (kJ mol ⁻¹)	ΔU (kJ mol ⁻¹)
End-member phases			
Fo	0	-4682.48	0.00
Clh	0.111	-20295.45	-7.28
Hum	0.143	-15615.35	-10.01
Chn	0.2	-10922.91	-9.98
Nor	0.333	-6242.26	-17.79
Sel	1	-3090.51	-24.02
Solid solution compounds			
f063	0.0625	-4581.44	0.05
f083	0.0833	-4548.11	-0.29
f125	0.125	-4480.84	-0.36
f250	0.25	-4280.36	-1.87
f500	0.5	-3882.51	-8.03
f750	0.75	-3473.16	-2.68
f875	0.875	-3269.41	-0.93
f917	0.9167	-3201.84	-0.70
f938	0.9375	-3167.89	-0.40
f1000	1	-3066.48	0.00

3.4. Discussion

3.4.1. Comparison of the GGA and LDA results

I carried out the molecular simulations in both the GGA and LDA in order to test the significance of the under- and overbinding effect imposed by the choice of computational method

on the predicted thermodynamic properties. Molar volumes and internal energies show systematic differences in these two approximations, which are related to a different treatment of the core and valence electrons (Oganov et al. 2002). The use of reduced volumes (V/V_0) in the pressure-volume equations of state, as well as utilization of energies of formation from end-members, Mg_2SiO_4 and Mg_2F_4 , substantially reduce these differences and provide consistent results for mineral stabilities and fluorine solubilities in forsterite. The reduced volumes (V/V_0) calculated by LDA become slightly lower at high pressures, that is, the phases are predicted to be stiffer. Consequently, the bulk moduli predicted by LDA are greater by 8-12 %; for sellaite, the difference reaches 20 %.

Internal energies computed using LDA are systematically higher than for GGA. For solid solution compounds the differences in internal energy varies from 63.36 (forsterite) to 44.43 $\text{kJ mol}^{-1} \text{atom}^{-1}$ (Mg_2F_4), whereas for the humite group minerals the internal energy differences decrease from 61.58 to 57.90 $\text{kJ mol}^{-1} \text{atom}^{-1}$; for sellaite, the value is 45.33 $\text{kJ mol}^{-1} \text{atom}^{-1}$. Energies of formation from end members calculated by LDA and GGA are consistent.

3.4.2. Comparison of the pressure-volume properties with experimental results

Pressure-volume relations at ambient temperature were determined for forsterite, sellaite and several hydroxyl- and fluorine-bearing minerals of the humite group. Experimental bulk modulus of forsterite ranges between 129.6 and 135.7 GPa with $K_0\phi = 3.88$ -4.00 (Hazen 1976, Will et al. 1986, Couvy et al. 2010). This is in a very good agreement with the result from our LDA simulations ($K_0 = 130.5$ GPa, $K_0\phi = 3.68$; Table 3-4), whereas the GGA results tend to underestimate the bulk modulus ($K_0 = 119.4$ GPa). Similarly, K_0 of sellaite was determined experimentally to be 101.7 GPa with $K_0\phi = 3.85$ (Vassilou et al. 1985), which is comparable to our LDA predictions ($K_0 = 105.3$ GPa, $K_0\phi = 3.74$; Table 3-4) rather than the GGA simulations ($K_0 = 84.3$ GPa). The experimental results for the humite-group minerals are less systematic, partly due to variable hydroxyl-fluorine ratios in the samples. With the exception of anomalously high bulk modulus for chondrodite ($K_0 = 136.2$ with $K_0\phi = 3.7$) reported by Faust and Knittle (1994), the bulk moduli of the humite group vary between 113.0 and 119.4 GPa ($K_0\phi = 4.0$ -5.6). These experimental measurements are in a slightly better agreement with the GGA results.

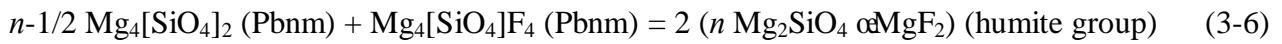
3.4.3. Fluorine solubility in forsterite

Thermodynamic properties of the orthorhombic forsterite- Mg_2F_4 solution, sellaite and humite-group minerals are used to calculate the solubility of fluorine in forsterite at elevated temperatures and pressures. Under all conditions studied, minerals of the humite-group are more stable than the orthorhombic forsterite- Mg_2F_4 solid solution. Therefore, the humite group minerals

may be set as buffers to define maximum solubilities of fluorine in forsterite. The solubility of fluorine is given by mole fraction of the Mg_2F_4 end member in the orthorhombic solution when the Gibbs energy of the following equilibrium becomes zero:



In view of the strong ordering near the $\text{Mg}_4[\text{SiO}_4]\text{F}_4$ composition, I will limit the solution range to the $\text{Mg}_4[\text{SiO}_4]_2$ - $\text{Mg}_4[\text{SiO}_4]\text{F}_4$ composition space. Upon reorganization, Eq. 3-5 becomes:



with the Gibbs energy of reaction ($\Delta_r G$) approximated as follows:

$$\Delta_r G \approx \Delta_r U^\circ + \int_0^P \Delta_r V^\circ dP + RT \ln K \quad (3-7)$$

where $\Delta_r U^\circ$ and $\Delta_r V^\circ$ are the standard reaction internal energies and volume, respectively. The equilibrium constant, K , incorporates activities of $\text{Mg}_4[\text{SiO}_4]_2$ and $\text{Mg}_4[\text{SiO}_4]\text{F}_4$ in the orthorhombic solid solution (Eq. 3-6). The ideal mixing contribution arises from mixing of the fluorine quadruplets on one of the tetrahedral sites only to account for ordering (see Section 3.3.3). The non-ideal contribution to the activity, expressed by the activity coefficient, γ , is defined by the symmetric Margules solution model:

$$RT \ln \gamma_i = (1 - X_i)^2 W \quad (3-8)$$

with $W = 6.8 \text{ kJ mol}^{-1}$.

I calculated the fluorine solubility in forsterite buffered by individual humite-group minerals up to 1900 K and 12 GPa (Table 3-A5; Fig. 3-7). The solubility of fluorine strongly increases with temperature, from 0.01-1.6 ppm at 500 K to 0.19-0.88 wt. % F at 1700 K and 0 GPa. Pressure has a subordinate effect on the fluorine solubility and it causes its decrease by a factor of four from 0 to 12 GPa. This is a consequence of consistently smaller molar volumes of the humite-group minerals than those of the orthorhombic solid solutions.

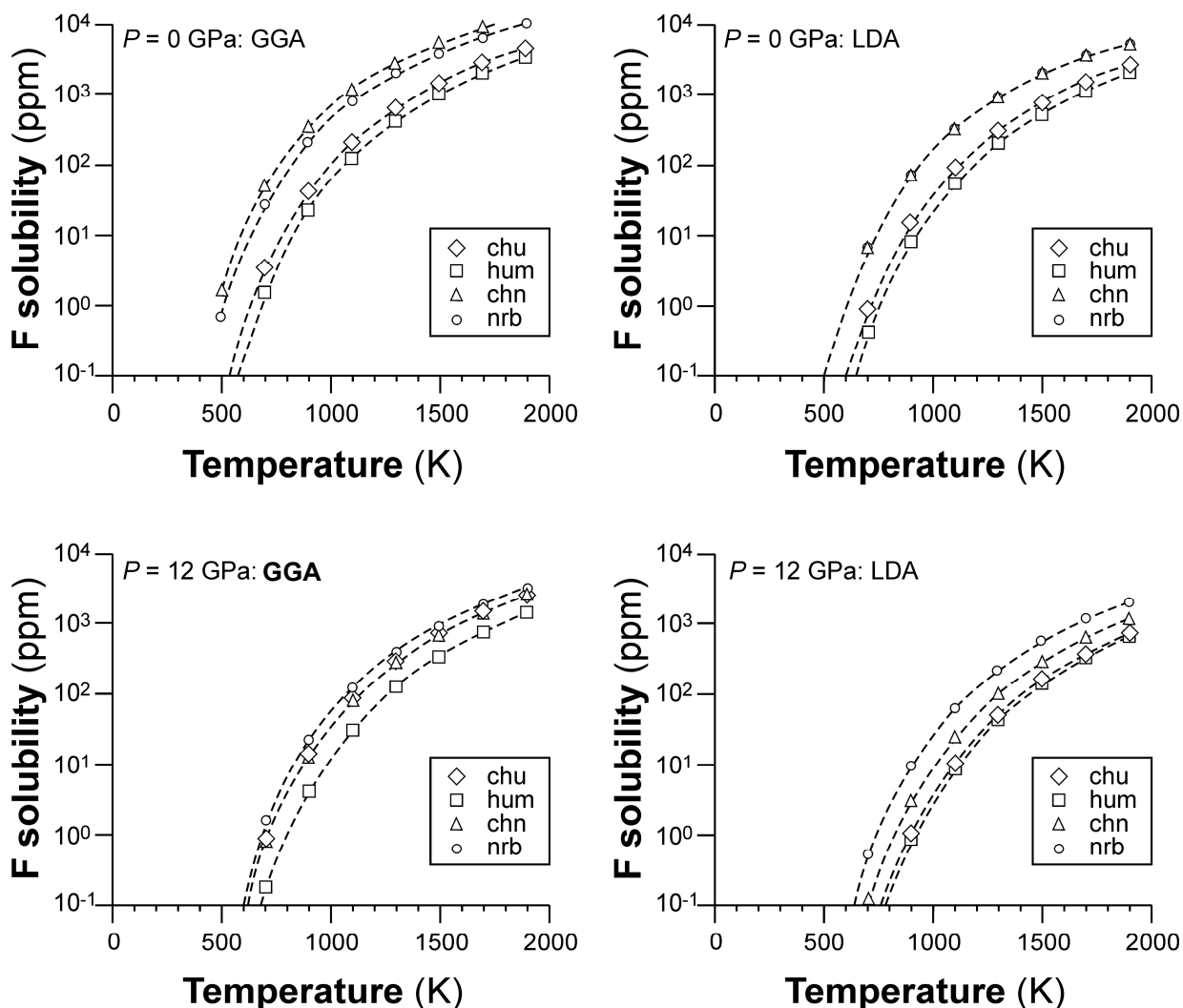


Fig. 3-7. Fluorine solubility in forsterite at $P = 0$ GPa and at $P = 12$ GPa buffered with humite-group minerals calculated by GGA and LDA.

The solubility differences defined by various humite-group buffers are minor (approx. half of an order of magnitude on the eight orders of magnitude scale). This is supported by experimental observation that enthalpy differences among individual humite-group phases are very small (Duffy and Greenwood 1977, Rice 1980, 1981). Under all conditions I simulated, the solubility of fluorine is the lowest when buffered by humite ($3 \text{ Mg}_2\text{SiO}_4 \rightleftharpoons \text{MgF}_2$) which implies that this mineral is the most stable phase within the humite group (*cf.* Fig. 3-7).

The results of our calculations are in a good agreement with experimental measurements up to 1600 °C and 2.6 GPa (Bromiley and Kohn 2007, Chapter 2). At 1350-1600 °C and 1-2 GPa, the fluorine solubilities in forsterite in equilibrium with clinohumite reach 0.45 wt. % F (Bromiley and Kohn 2007) whereas my GGA calculations predict 4.3-2.4 wt.% F. However, my calculations indicate that the stable buffer should be humite, dictating the solubility of 0.08-0.31 wt. % F with humite as stable buffer. In Chapter 2 I have determined the concentration of 246-267 ppm F in

forsterite in equilibrium with fluorine-bearing fluids (salinity 1.6 wt. % F), undersaturated with the humite-group minerals at 1100 °C and 2.6 GPa. According to our calculation at such pressure and temperature conditions the fluorine solubility is about 800 ppm F using the GGA, and about 300 ppm with the LDA.

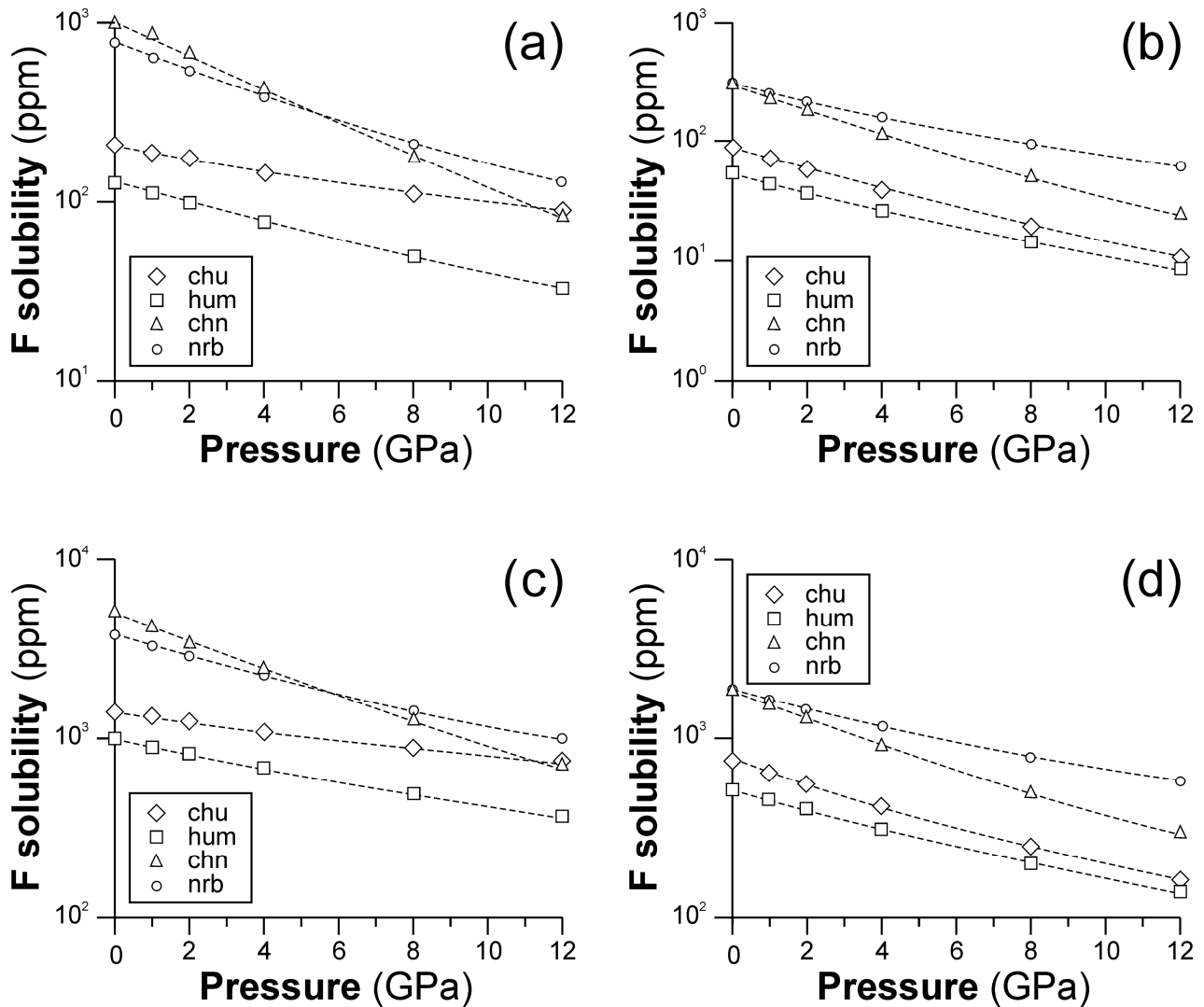


Fig. 3-8. Fluorine solubility in forsterite at $T = 1100$ K (a, b) and $T = 1500$ K in (c, d) buffered with the humite-group minerals calculated by GGA (a, c) and LDA (b, d).

3.4.4. Geochemical implications

My calculations predict that the maximum solubility of fluorine in forsterite strongly depends on temperature; it increases from 23 ppm to 0.2 wt. % F between 625 and 1425 °C at 0 GPa, and from 7 ppm to 0.1 wt. % F in the same temperature range at 8 GPa. The average fluorine concentration in the Earth's primitive mantle is 25 ppm (McDonough and Sun 1995). The main fluorine carriers are phlogopite, apatite and amphibole (Smyth 1981), whereas fluorine concentrations in anhydrous mantle phases are negligible (Smyth 1981, Aiuppa et al. 2009). The

fluorine budget of the subducting slab is highly variable and it depends on the proportion of sedimentary component and degree of hydration, that is, modal abundance of amphibole and serpentine. Subducting sediments host 490-620 ppm F (Gao et al. 1998), hydrated oceanic crust contains approx. 78 ppm F (Straub and Layne 2003), whereas the fluorine budget in the underlying lithospheric mantle varies between 47 and 430 ppm according to the degree of serpentinization (Wei et al. 2008). These estimates imply that subducting slab may contain up to one order of magnitude higher concentrations of fluorine than the primitive Earth's mantle. Along the slab geotherm, the predicted fluorine solubility in forsterite is very low, less than 50 ppm, due to depressed temperature. It is, therefore, unlikely, that nominally anhydrous minerals as products of slab devolatilization reactions, will contain fluorine abundances that would substantially exceed the average mantle budget.

The efficiency of fluorine sequestration to aqueous fluids or partial melts and its subsequent dispersal or storage in the mantle wedge is dictated by the values of the fluid-mineral partition coefficient ($D^{fl/min}$) and its dependence on temperature and pressure. The strong temperature dependence of fluorine solubility in forsterite suggests that $D^{fl/min}$ should rapidly decrease as temperature increases. During devolatilization, fluorine will preferentially partition to the aqueous fluids ($D^{fl/min} \sim 10^2-10^3$; see Chapter 2) but as the fluid pervades the mantle wedge along the path of increasing temperature and decreasing pressure (Manning 2004), the solubility of fluorine in forsterite substantially increases ($D^{fl/min}$ decreases). Portion of the fluorine budget in the fluid will be transferred to the mantle wedge peridotites, thus enhancing the mantle metasomatism. This scenario is supported by mass balance calculations (Straub and Layne 2003), which indicate that approx. 50 % of the fluorine budget in the volcanic arc magmas has a slab origin (*via* aqueous fluids).

3.5. References

- Aiuppa A., Baker D. R., Webster J. D. (2009): Halogens in volcanic systems, *Chemical Geology*, 263, 1-18.
- Angel R. J. (2000): Equations of state, *Reviews in Mineralogy and Geochemistry*, 41, 35-58.
- Baur W. H. (1976): Rutile-type compounds. V. Refinement of MnO_2 and MgF_2 , *Acta Crystallographica B*, 32, 2200-2204.
- Birch F. (1947): Finite elastic strain of cubic mineral, *Physical Review*, 71, 809-824.
- Birle J. D., Gibbs G. V., Moore P. B., Smith J. V. (1968): Crystal structures of natural olivines, *American Mineralogist*, 53, 807-824.

- Bromiley D. W., Kohn S. C. (2007): Comparisons between fluoride and hydroxide incorporation in nominally anhydrous and fluorine-free mantle minerals, *Geochimica et Cosmochimica Acta*, 71, A124.
- Couvy H., Chen J., Drozd V. (2010): Compressibility of nanocrystalline forsterite, *Physics and Chemistry of Minerals*, 37, 6, 343-351.
- Duffy C. J., Greenwood H. J. (1979): Phase equilibria in the system MgO-MgF₂-SiO₂-H₂O, *American Mineralogist*, 64, 1156-1173.
- Dymek R. F., Boak J. L., Brothers S. C. (1988): Titanian chondrodite-bearing and titanian clinohumite-bearing metadunite from the 3,800 Ma Isua Supracrustal Belt, West Greenland - Chemistry, petrology, and origin, *American Mineralogist*, 73, 547-558.
- Evans B. W., Trommsdorff V. (1983): Fluorine-hydroxyl titanian clinohumite in Alpine recrystallized garnet peridotite: compositional controls and petrologic significance, *American Journal of Science*, 283, 355-369.
- Faust J., Knittle E. (1994): Static compression of chondrodite: implications for water in the upper mantle, *Geophysical Research Letters*, 21, 1935-1938.
- Frost D. J. (2006): The stability of hydrous mantle phases, *Reviews in Mineralogy and Geochemistry*, 62, 243-271.
- Gao S., Luo T. C., Zhang B. R., Zhang H. F., Han Y. W., Zhao Z. D., Hu Y. K. (1998): The chemical composition of the continental crust as revealed by studies in East China, *Geochimica et Cosmochimica Acta*, 62, 1959-1975.
- Gibbs G. V., Ribbe P. H. (1969): The crystal structures of the humite minerals: I. Norbergite, *American Mineralogist*, 54, 376-390.
- Gibbs G. V., Ribbe P. H., Anderson C. P. (1970): The crystal structures of the humite minerals. II. Chondrodite, *American Mineralogist*, 55, 1182-1194.
- Hazen R. M. (1976): Effects of temperature and pressure on the crystal structure of forsterite, *American Mineralogist*, 61, 1280-1293.
- Hohenberg P., Kohn W. (1964): Inhomogeneous electron gas, *Physical Review B*, 136, 864-871.
- Kawamoto T. (2006): Hydrous phases and water transport in the subducting slab, *Reviews in Mineralogy and Geochemistry*, 62, 273-289.
- Kohn W., Sham L. J. (1965): Self-consistent equations including exchange and correlation effects, *Physical Review*, 140, 1133-1138.
- Kresse G., Hafner J. (1994): Norm-conserving and ultrasoft pseudopotential for first-row and transition-elements, *Physics Review B*, 47, 558-561.
- Kresse G., Furthmüller J. (1996): Efficiency of ab-initio total energy calculations for metals and semiconductors. *Computational Material Science*, 6, 15-50.

- Kresse G., Furthmüller J. (1996): Efficient iterative schemes for ab initio total-energy calculations using a plane-wave basis set. *Physical Review B*, 54, 11169-11186.
- López Sánchez-Vizcaíno V., Trommsdorff V., Gómez-Pugnaire M. T., Garrido C. J., Müntener O., Connolly J. A. D. (2005): Petrology of titanian clinohumite and olivine at the high pressure breakdown of antigorite serpentinite to chlorite harzburgite (Almirez Massif, S. Spain), *Contributions to Mineralogy and Petrology*, 149, 627-646.
- Manning, C. E. (2004): The chemistry of subduction-zone fluids. *Earth and Planetary Science Letters*, 223, 1-16.
- McDonough W. F., Sun S.-S. (1995): The composition of the Earth, *Chemical Geology*, 120, 223-253.
- McGetchin T. R., Silver L. T. (1970): Compositional relations in minerals from kimberlite and related rocks in the Moses Rock dike, San Juan Country, Utah, *American Mineralogist*, 55, 1738-1771.
- Möckel J. R. (1969): Structural petrology of the garnet peridotite of Alpe Arami (Ticino), Switzerland, *Leidse Geologische Mededelingen*, 42, 61-130.
- Murnaghan F. D. (1937): Finite deformations of an elastic solid, *American Journal of Mathematics*, 49, 235-260.
- Oganov A. R., Brodholt J. P., Price G. D. (2002): *Ab initio* theory of phase transitions and thermoelasticity of minerals, *EMU Notes in Mineralogy*, 4, 83-170.
- Perdew J. P., Burke K., Wang Y. (1996): Generalized gradient approximation for the exchange-correlation hole of a many-electron system, *Physical Review B*, 54, 16533-16539.
- Rice J. M., (1980): Phase Equilibria Involving Humite Minerals in Impure Dolomitic Limestones Part I. Calculated Stability of Clinohumite, *Contributions to Mineralogy and Petrology*, 71, 219-235.
- Rice J. M., (1981): Phase Equilibria Involving Humite Minerals in Impure Dolomitic Limestones Part II: Calculated Stability of Chondrodite and Norbergite, *Contributions to Mineralogy and Petrology*, 75, 205-223.
- Ribbe P. H., Gibbs G. V. (1971): Crystal structures of the humite minerals: III. Mg/Fe Ordering in the humite and its relation to other ferromagnesian silicates, *American Mineralogist*, 56, 1155-1173.
- Robinson K., Gibbs G. V., Ribbe P. H. (1973): The crystal structures of the humite group minerals. IV. Clinohumite and titanoclinohumite, *American Mineralogist*, 58, 43-49.
- Smyth J. R. (1981): Halogen and phosphorus storage in the Earth, *Nature* 289, 762-765.
- Smyth J. R., Madel R. E., McCormick T. C., Monuz J. L., Rossman G. R. (1990): Crystal-structure refinement of a F-bearing spessartine garnet, *American Mineralogist*, 75, 314-318.

- Smyth J. R. (2006): Hydrogen in high pressure silicate and oxide mineral structures, *Reviews in Mineralogy and Geochemistry*, 62, 85-115.
- Straub S. M., Layne G. D. (2003): The systematic of chlorine, fluorine, and water in Izu arc front volcanic rocks: implications for volatile recycling in subduction zone, *Geochimica et Cosmochimica Acta*, 21, 4179-4203.
- Strunz H., Nickel E. H. (2001): Strunz mineralogical tables. Chemical-structural mineral classification system, 9th edition, *Schweizerbart, Berlin and Stuttgart*, 870 pp.
- Taylor W. H., West J. (1928): The crystal structure of the chondrodite series, *Proceedings of the Royal Society (London)*, 117, 517-552.
- Trommsdorff V., Evans B.W. (1980): Titanian hydroxyl-clinohumite- formation and breakdown in antigorite rocks (Malenco, Italy), *Contributions to Mineralogy and Petrology*, 72, 229-242.
- Valley J. W., Essene E. J., Peacor D. R. (1983): Fluorine-bearing garnets in Adirondack calc-silicates, *American Mineralogist*, 68, 444-448.
- Vassilou J. K. (1984): Pressure dependence of the elastic moduli of single crystal MgF₂ to 1 GPa, *Journal of Applied Physics*, 57, 4543-4547.
- Visser D. (1993): Fluorine-bearing hydrogarnets from Blengsvatn, Bamble sector, south Norway, *Mineralogy and Petrology*, 47, 209-218.
- Wedepohl K. H. (1995): The composition of the continental crust, *Geochimica et Cosmochimica Acta*, 59, 1217-1232.
- Wei W., Kastner M., Spivack A. (2008): Chlorine isotopes and halogen concentrations in convergent margins with implications for the Cl isotopes cycle in the ocean, *Earth and Planetary Science Letters*, 266, 90-104.
- Will G., Hoffbauer W., Hinze E., Lauterjung J. (1986): The compressibility of forsterite up to 300 kbar measured with synchrotron radiation, *Physica*, 139-140, 193-197.
- Wunder B., Schreyer W. (1997): Antigorite: high-pressure stability in the system MgO-SiO₂-H₂O (MSH), *Lithos*, 41, 213-227.
- Yamamoto K., Akimoto S. I. (1977): The system MgO-SiO₂-H₂O at high pressures and temperatures ó stability field of hydroxyl-chondrodite, hydroxyl-clinohumite and 10 Å phase, *American Journal of Science*, 277, 288-312.

3.6. Appendix

Table 3-A1. Calculated pressure (GPa) at different molar volumes ($\text{cm}^3 \text{mol}^{-1}$) per formula unit for minerals (GGA results)

Phase												
Fo	$V (\text{cm}^3 \text{mol}^{-1})$	44.54	46.15	44.06	39.86	37.76	35.66	33.57	31.47	29.37	27.27	
	$P (\text{GPa})$	0	-3.80	1.16	15.87	26.2	39.44	56.71	78.85	107.20	143.76	
Clh	$V (\text{cm}^3 \text{mol}^{-1})$	198.95	205.72	196.37	187.02	173.93	168.32	162.71	158.97	155.23	149.61	
	$P (\text{GPa})$	0	-3.66	1.24	7.61	19.39	25.74	33.18	38.74	44.83	55.35	
Hum	$V (\text{cm}^3 \text{mol}^{-1})$	154.29	167.94	160.31	145.04	141.99	137.41	132.83	129.77	126.72	122.14	
	$P (\text{GPa})$	0	-7.92	-3.98	7.48	10.61	15.91	22.10	26.79	31.98	40.78	
Chn	$V (\text{cm}^3 \text{mol}^{-1})$	109.02	119.01	113.60	102.78	100.61	97.37	94.12	91.96	89.80	86.55	
	$P (\text{GPa})$	0	-8.01	-4.12	7.34	10.39	15.59	21.78	26.44	31.58	40.33	
Nor	$V (\text{cm}^3 \text{mol}^{-1})$	64.81	70.09	66.91	60.53	59.26	57.35	55.44	54.16	52.89	50.98	
	$P (\text{GPa})$	0	-7.05	-3.02	8.41	11.47	16.68	22.85	27.46	32.50	41.14	
Sel	$V (\text{cm}^3 \text{mol}^{-1})$	20.22	21.43	20.50	19.56	18.45	18.07	17.70	17.33	16.77	16.21	
	$P (\text{GPa})$	0	-4.29	-0.69	2.88	9.51	12.00	14.86	17.99	23.28	29.15	

Table 3-A2. Calculated pressure (GPa) at different molar volumes ($\text{cm}^3 \text{mol}^{-1}$) per formula unit for minerals (LDA)

Phase												
Fo	$V (\text{cm}^3 \text{mol}^{-1})$	41.61	46.14	44.04	39.86	37.75	35.65	33.55	31.46	29.36	27.26	
	$P (\text{GPa})$	0	-10.72	-6.53	7.88	15.33	27.32	42.40	62.03	87.49	120.42	
Clh	$V (\text{cm}^3 \text{mol}^{-1})$	185.30	205.72	196.37	177.67	173.93	168.32	162.71	158.97	155.11	149.62	
	$P (\text{GPa})$	0	-10.66	-6.47	5.84	9.10	14.71	21.26	26.21	31.71	41.01	
Hum	$V (\text{cm}^3 \text{mol}^{-1})$	143.66	167.94	160.31	145.04	141.99	137.41	132.83	129.77	126.72	122.14	
	$P (\text{GPa})$	0	-14.23	-10.99	-1.12	1.55	6.18	11.63	15.71	20.28	28.07	
Chn	$V (\text{cm}^3 \text{mol}^{-1})$	101.79	119.00	113.59	102.77	100.61	97.37	94.12	91.96	89.79	86.54	
	$P (\text{GPa})$	0	-14.32	-11.18	-1.45	1.22	5.82	11.23	15.32	19.83	27.50	
Nor	$V (\text{cm}^3 \text{mol}^{-1})$	60.27	70.09	66.91	60.53	59.26	57.35	55.44	54.16	52.87	50.98	
	$P (\text{GPa})$	0	-13.58	-10.27	-0.46	2.20	6.67	11.95	15.97	20.45	28.03	
Sel	$V (\text{cm}^3 \text{mol}^{-1})$	18.39	20.39	19.46	19.09	17.98	17.61	17.24	16.68	16.13	15.75	
	$P (\text{GPa})$	0	-8.73	-5.34	-3.65	2.61	5.16	7.92	12.57	17.9	21.91	

Table 3-A3. Calculated pressure (GPa) at different molar volumes ($\text{cm}^3 \text{mol}^{-1}$) per formula unit for orthorhombic solid solution (GGA results)

Phase		Ref.									
f063	$V (\text{cm}^3 \text{mol}^{-1})$	44.40	46.14	44.04	39.85	37.75	35.65	33.55	31.46	29.36	27.26
	$P (\text{GPa})$	0	-3.92	0.86	14.98	24.92	37.76	54.38	75.60	103.11	138.94
f083	$V (\text{cm}^3 \text{mol}^{-1})$	44.34	46.14	44.04	39.85	37.75	35.65	33.55	31.46	29.36	27.26
	$P (\text{GPa})$	0	-4.01	0.66	14.66	24.58	37.18	53.58	74.62	101.94	137.27
f125	$V (\text{cm}^3 \text{mol}^{-1})$	44.26	46.14	44.04	39.84	37.75	35.65	33.55	31.46	29.36	27.26
	$P (\text{GPa})$	0	-4.12	0.43	14.06	23.74	36.03	52.06	72.56	99.15	134.13
f250	$V (\text{cm}^3 \text{mol}^{-1})$	44.08	45.46	43.39	39.26	37.19	35.12	33.06	30.99	28.92	26.86
	$P (\text{GPa})$	0	-3.01	1.65	14.97	24.49	36.56	51.98	72.03	97.25	131.29
f500	$V (\text{cm}^3 \text{mol}^{-1})$	43.53	45.46	43.39	39.26	37.19	35.12	33.06	30.99	28.93	26.86
	$P (\text{GPa})$	0	-3.53	0.27	11.73	19.42	29.83	42.98	60.44	82.09	111.36
f750	$V (\text{cm}^3 \text{mol}^{-1})$	42.91	45.46	43.39	39.26	37.19	35.12	33.06	30.99	28.93	26.86
	$P (\text{GPa})$	0	-4.00	-0.89	8.12	14.67	22.76	33.74	48.07	66.87	90.94
f875	$V (\text{cm}^3 \text{mol}^{-1})$	42.16	46.14	44.04	39.85	39.01	37.75	36.49	35.65	34.81	33.56
	$P (\text{GPa})$	0	-5.26	-2.67	4.31	6.46	9.90	13.48	16.35	19.69	25.68
f917	$V (\text{cm}^3 \text{mol}^{-1})$	42.17	46.21	44.11	39.91	39.07	37.81	36.55	35.71	34.87	33.61
	$P (\text{GPa})$	0	-5.35	-2.99	3.89	5.72	8.90	12.52	15.54	18.44	23.89
f938	$V (\text{cm}^3 \text{mol}^{-1})$	42.27	42.35	40.43	36.58	35.81	34.65	33.50	32.73	31.96	30.80
	$P (\text{GPa})$	0	-0.46	2.51	11.96	14.45	18.82	23.97	27.92	32.11	39.53
f1000	$V (\text{cm}^3 \text{mol}^{-1})$	42.10	41.55	39.67	35.88	35.13	33.99	32.11	30.22	28.33	26.44
	$P (\text{GPa})$	0	0.54	3.31	12.92	15.37	20.06	28.93	40.48	56.09	76.57

Table 3-A4. Calculated pressure (GPa) at different molar volumes ($\text{cm}^3 \text{mol}^{-1}$) for orthorhombic solid solution (LDA results)

Phase		Ref.										
f063	$V (\text{cm}^3 \text{mol}^{-1})$	41.44	46.14	44.04	39.85	37.75	35.65	33.55	31.46	29.36	27.26	
	$P (\text{GPa})$	0	-10.80	-6.79	5.38	14.22	25.66	40.18	59.12	83.57	115.22	
f083	$V (\text{cm}^3 \text{mol}^{-1})$	41.37	46.14	44.04	39.85	37.75	35.65	33.55	31.46	29.36	27.26	
	$P (\text{GPa})$	0	-10.87	-6.92	5.11	13.76	25.10	39.48	58.20	82.42	113.86	
f125	$V (\text{cm}^3 \text{mol}^{-1})$	41.25	46.14	44.04	39.85	37.75	35.65	33.55	31.46	29.36	27.26	
	$P (\text{GPa})$	0	-10.95	-7.09	4.62	13.03	24.07	38.05	56.32	79.97	110.58	
f250	$V (\text{cm}^3 \text{mol}^{-1})$	40.96	45.45	43.39	39.26	37.19	35.12	33.06	30.99	28.92	26.86	
	$P (\text{GPa})$	0	-9.68	-6.01	5.39	13.76	24.34	37.92	55.56	78.38	108.19	
f500	$V (\text{cm}^3 \text{mol}^{-1})$	40.20	45.46	43.39	39.26	37.19	35.12	33.06	30.99	28.93	26.86	
	$P (\text{GPa})$	0	-10.09	-6.99	2.60	9.49	18.43	29.93	44.60	63.92	89.69	
f750	$V (\text{cm}^3 \text{mol}^{-1})$	39.04	45.46	43.39	39.26	37.19	35.12	33.06	30.99	28.93	26.86	
	$P (\text{GPa})$	0	-9.94	-7.74	-0.38	5.16	12.22	21.59	33.53	49.65	71.00	
f875	$V (\text{cm}^3 \text{mol}^{-1})$	38.06	46.14	44.04	39.85	39.01	37.75	36.49	35.65	34.81	33.55	
	$P (\text{GPa})$	0	-10.50	-8.79	-3.43	-1.75	0.93	4.14	6.55	9.35	14.29	
f917	$V (\text{cm}^3 \text{mol}^{-1})$	37.92	41.57	39.68	35.90	35.15	34.01	32.88	32.12	31.37	30.24	
	$P (\text{GPa})$	0	-6.21	-3.48	4.99	7.30	11.14	15.83	19.40	23.27	30.08	
f938	$V (\text{cm}^3 \text{mol}^{-1})$	37.91	39.92	38.11	34.48	33.76	32.67	31.58	30.85	30.13	29.04	
	$P (\text{GPa})$	0	-4.05	-0.58	9.07	11.64	16.10	21.30	25.35	29.73	37.40	
f1000	$V (\text{cm}^3 \text{mol}^{-1})$	37.48	41.51	39.63	35.85	35.10	33.97	32.08	30.19	28.30	26.42	
	$P (\text{GPa})$	0	-6.37	-4.12	3.65	5.82	9.20	16.56	26.74	40.17	57.78	

Table 3-A5. Calculated solubilities of fluorine (ppm F) in forsterite (GGA results)

Buffer	Pressure (GPa)	Temperature (K)							
		500	700	900	1100	1300	1500	1700	1900
Clinohumite	0	0.038	3.43	42.09	208.02	633.06	1445.21	2752.71	4644.66
	1	0.030	2.88	36.73	186.05	575.34	1328.89	2550.88	4325.96
	2	0.025	2.54	33.30	171.82	537.02	1251.48	2416.50	4114.63
	4	0.017	1.91	26.69	143.17	460.10	1092.37	2137.03	3674.54
	8	0.009	1.23	18.99	108.27	362.95	886.55	1770.94	3093.31
	12	0.006	0.87	14.42	86.38	299.59	749.75	1524.21	2694.18
Humite	0	0.013	1.57	22.86	126.03	412.53	989.92	1947.79	3353.06
	1	0.009	1.28	19.57	110.97	370.14	900.17	1788.60	3103.02
	2	0.007	1.06	16.82	98.00	333.15	820.66	1647.29	2877.50
	4	0.004	0.73	12.61	77.36	272.40	689.13	1408.50	2495.11
	8	0.002	0.36	7.24	49.14	185.32	492.28	1043.98	1901.12
	12	0.001	0.19	4.35	32.35	130.05	361.60	793.49	1483.08
Chondrodite	0	1.60	49.92	339.13	1158.34	2747.66	5253.23	8758.35	13330.67
	1	0.92	33.71	249.47	898.65	2206.13	4318.69	7320.39	11257.89
	2	0.51	22.10	179.33	684.44	1745.77	3508.40	6053.7	9432.47
	4	0.18	10.58	101.07	426.66	1164.59	2452.13	4376.71	6987.62
	8	0.03	2.73	35.23	179.63	556.51	1283.04	2446.07	4099.17
	12	0.005	0.82	13.81	83.39	290.09	726.39	1472.43	2584.12
Norbergite	0	0.70	27.63	213.49	788.33	1961.37	3857.05	6519.24	9936.45
	1	0.46	20.40	168.46	648.76	1660.26	3330.70	5712.57	8805.06
	2	0.31	15.34	134.93	540.39	1419.87	2903.27	5049.46	7867.19
	4	0.15	9.12	89.98	387.35	1069.53	2263.60	4039.56	6418.29
	8	0.04	3.55	43.21	212.21	640.54	1445.98	2706.91	4462.45
	12	0.005	1.64	23.70	129.72	421.63	1004.35	1956.86	3326.41

Table 3-A6. Calculated solubilities of fluorine (ppm F) in forsterite (LDA results)

Buffer	Pressure (GPa)	Temperature (K)							
		500	700	900	1100	1300	1500	1700	1900
Clinohumite	0	0.006	0.90	14.91	88.81	306.75	765.46	1550.76	2738.85
	1	0.004	0.65	11.51	71.91	256.25	653.96	1348.55	2409.05
	2	0.002	0.47	8.97	58.61	215.38	561.82	1177.16	2128.75
	4	0.001	0.26	5.58	39.72	154.08	421.52	910.67	1684.41
	8	-	0.09	2.37	19.74	85.51	251.30	575.17	1111.47
	12	-	0.03	1.14	10.83	51.48	161.64	388.83	780.61
Humite	0	0.002	0.41	8.08	53.72	199.98	525.89	1107.16	2004.80
	1	0.001	0.31	6.41	44.47	170.28	457.46	977.98	1791.40
	2	-	0.23	5.14	37.12	146.03	399.94	867.80	1607.95
	4	-	0.13	3.38	26.32	109.17	310.61	693.48	1312.61
	8	-	0.05	1.62	14.42	65.53	199.29	467.82	920.49
	12	-	0.02	0.88	8.78	43.08	138.49	338.86	688.50
Chondrodite	0	0.092	6.47	68.94	311.51	899.68	1935.71	3535.82	5742.44
	1	0.052	4.31	50.17	240.08	712.93	1592.98	2968.56	4892.15
	2	0.030	2.91	36.99	186.90	575.78	1321.42	2511.32	4199.38
	4	0.011	1.39	20.79	116.64	385.72	930.92	1836.07	3158.63
	8	0.002	0.37	7.47	50.42	189.30	500.82	1057.57	1916.41
	12	-	0.12	3.13	24.70	103.41	296.02	663.29	1258.11
Norbergite	0	0.087	6.26	67.15	304.60	871.10	1891.35	3440.01	5544.13
	1	0.060	4.77	54.37	256.13	751.84	1662.88	3066.38	4995.29
	2	0.042	3.69	44.52	217.42	653.92	1472.20	2750.20	4526.64
	4	0.022	2.30	30.77	160.61	505.53	1176.04	2251.98	3776.39
	8	0.006	1.02	16.34	95.63	325.61	801.67	1601.75	2775.72
	12	0.003	0.53	9.79	62.86	228.11	588.20	1216.85	2166.43

- indicates fluorine solubility below 1 ppb

4. Zircon solubility in aqueous fluids at high temperatures and pressures

4.0. Abstract

Depletion of high field strength elements is a characteristic feature of arc magmas and it has been attributed to low solubility of Zr, Nb and Ta in slab-derived aqueous fluids. I have determined zircon solubility in aqueous fluids up to 1025 °C and 20 kbar by *in situ* observation of dissolving zircon grains in the hydrothermal diamond anvil cell. Zircon solubilities in H₂O with silica activity buffered by quartz are very low, from 1.0 to 3.3 ppm Zr, and weakly increase with temperature and pressure. Experimental results were fitted to a density model:

$$\log c = 3.45 - \frac{3803}{T} + 1.52 \log \rho$$

where c is the Zr concentration in the fluid (ppm), T is temperature (K) and ρ is the fluid density (g cm⁻³). An additional experiment with a saline fluid (15 wt. % NaCl) revealed an increase in zircon solubility by a factor of 3 (4.8 ± 1.6 ppm Zr at 890 °C and 14 kbar) whereas addition of 4.5 wt. % albite as solute increased solubility by about a factor of 5. The Zr solubility at the forsterite-enstatite silica buffer is slightly higher than that at the quartz buffer and it further increases at baddeleyite saturation (48 ± 15 ppm Zr at 930 °C and 16 kbar). These observations are consistent with the stability of zircon relative to ZrO₂ + SiO₂ and suggest that Zr-Si complexes are not abundant in the fluid. During slab dehydration, the Zr content in the aqueous fluid is predicted to be 1-2 ppm and mass balance calculations imply that the high field strength element concentrations in primary arc melts will slightly decrease due to the dilution effect of infiltrating fluid. By contrast, mobile lithophile elements are predicted to increase their abundances in the melt by orders of magnitude. Our results and interpretations demonstrate that decoupling of large ion lithophile vs. high field strength elements in the arc magmas is related to different solubilities of these elements in aqueous fluids migrating from the slab to the magma source regions.

4.1. Introduction

The behavior of high field strength elements (HFSE) in subduction zones imparts a characteristic fingerprint to silicate magmas produced at convergent plate boundaries. Magma generation in the mantle wedge is assisted by fluid infiltration from the subducting slab. At subarc conditions aqueous fluids are produced by prograde breakdown of hydrous phases (Rüpke et al. 2004), and are believed to act as efficient transport agents of slab-derived constituents to the

mantle wedge (Manning 2004, Kessel et al. 2005). Their ability to transport elements into the mantle wedge is strongly influenced by the solubility and speciation of individual components. Large ion lithophile elements (LILE) are usually much more soluble and thus more mobile than high field strength elements (Pearce and Stern 2006). HFSE/LILE ratios are appreciably lower in arc magmas than in mid-ocean ridge basalts (Pearce et al. 2005), which may be the result of (i) the low solubility of HFSE compared to LILE in subduction zone fluids; (ii) preferential uptake of HFSE in the mantle wedge during the passage of slab-derived fluids or melts (Saunders et al. 1980), and/or (iii) reaction of partial melts with mantle peridotite during ascent (Kelemen et al. 1993). Recent analytical studies (e.g. Münker et al. 2004) increasingly favor the retention of HFSE relative to LILE in the slab due to their very solubility in aqueous fluids. Our knowledge of HFSE geochemistry in aqueous fluids at conditions relevant to subduction zones is, however, almost exclusively based on partitioning experiments between mantle silicate minerals and aqueous fluids (Brenan et al. 1994, Brenan et al. 1995, Keppler 1996, Ayers 1998, Stalder et al. 1998). Direct measurements of the solubilities of Zr-, Nb- or Ta-bearing phases are missing or rare (Baier et al. 2008).

Precise determination of the very low solubilities of HFSE in aqueous fluids remains a technical and analytical challenge. Mineral weight loss experiments performed in piston cylinder may suffer from excessive dissolution and reprecipitation of the minerals inside the capsule (Tropper and Manning 2005), or weight changes may become undetectable at concentrations approaching ppm level. These issues may be overcome by visual observation of the dissolution of mineral grains in aqueous fluid of known mass in a hydrothermal diamond anvil cell (HDAC; Audétat and Keppler 2005). The low thermal gradients obtainable in the HDAC and the possibility to reverse the dissolution process and observe re-precipitation of the mineral during cooling represent a significant advantage over the conventional quenching experiments in a piston-cylinder apparatus.

In this study I used the method of visual observation of complete dissolution in the HDAC to determine the solubility of zircon in H₂O at 865-1025 °C and 6.2-20.0 kbar. Exploratory experiments were conducted to assess the role of chloride ligands and silicate solute on the zircon solubility. The experimental results were used to calibrate a simple thermodynamic model for predicting zirconium solubilities as a function of temperature, pressure and activity of SiO₂.

4.2. Experimental methodology

Dissolution experiments were performed in an externally heated hydrothermal diamond anvil cell of the Bassett-type (Bassett et al. 1993a, b). Small pieces of zircon with measurable

volume were prepared from a single gem quality zircon crystal from Sri Lanka annealed at 900 °C for 16 hours. Crystal fragments were manufactured into doubly polished sections 1.0-1.6 mm thick and then broken down into regular pieces. The exact dimensions of individual pieces were determined by secondary electron microscopy, and the corresponding weight calculated by using a zircon density of 4.65 g cm⁻³. Single zircon piece was then transferred with a small needle into the open sample chamber of HDAC. In our experiments I used diamonds with a culet size of 1 mm and rhenium gaskets with bores measuring 500 μm in diameter. For Cl-bearing runs a 100 μm thick gold lining was used to avoid corrosion of the rhenium gasket and contamination of the experimental charge. In all experiments, new rhenium gaskets were used in order to avoid any zirconium contamination from previous runs. Both diamonds anvils were heated independently by molybdenum wire resistance heaters that can reach maximum temperature of approx. 1100 °C. The temperature of each diamond was recorded by NióCr thermocouples placed in direct contact with diamond covered by ceramic cement. Heating paths were controlled by manually increasing the voltage applied to the heaters, in a manner that the temperatures of the two diamonds were always within ~2 °C. In order to minimize thermal gradient between the diamond surface and the rhenium gasket, the space surrounding the diamond anvils and the rhenium gasket was filled with zirconia wool. Temperature within the sample chamber was calibrated by measuring the melting point of NaCl (800.6 °C) that was previously dried at 130 °C overnight to remove any fluid inclusions.

In most runs the diamond anvil cell was heated with a rate of 30635 °C min⁻¹ until it reached 600 °C, then the heating rate was lowered to 7615 °C min⁻¹ in order to allow for equilibrium between dissolving solids and the surrounding fluid. The latter heating rate was maintained until complete dissolution of the solid occurred. Pressure in HDAC experiments is mainly generated during heating because the aqueous fluid is confined to a sealed chamber of constant volume and thus follows an isochoric path (Shen *et al.* 1992). By varying the ratio between added solution and remaining air bubble in the sample chamber, variable pressures can be obtained at a given temperature. The mass of added water can be accurately determined from the liquidóvapor homogenization temperature and the volume of the sample chamber, with the latter being calculated based on the bulk density and the volume of the vapor bubble at some arbitrary temperature (Audéat and Keppler 2005):

$$V_{\text{cell}} = \frac{V_{\text{vap}}(\rho_{\text{vap}} - \rho_{\text{liq}})}{(\rho_{\text{tot}} - \rho_{\text{liq}})} \quad (4-1)$$

In this equation V_{vap} and V_{cell} stand for the volumes of the vapour bubble and the fluid-accessible part of sample chamber (i.e., excluding the volume of loaded solids), respectively, ρ_{vap} and ρ_{liq} for the densities of vapour and liquid, and ρ_{tot} for the bulk fluid density calculated from the homogenization temperature. The calculations were repeated five times using bubble diameters measured at different temperatures and the results were averaged. In the run with a 15 wt. % NaCl solution the densities of the liquid phase were adjusted to account for the presence of dissolved salt.

Zircon solubility at the temperature of complete dissolution was calculated from the mass of the loaded zircon piece, the mass of the loaded solution including the mass of silicate dissolved in the fluid. In the runs buffered by quartz the latter was calculated from the data of Manning (1994) and Newton and Manning (2000), whereas in the forsterite-enstatite buffered run it was estimated at 0.4 times the value of quartz saturation (value corresponding to activity of quartz at this buffer). Pressure in the sample chamber at the time of complete zircon dissolution was calculated from the fluid density measured after cooling to room temperature, using the equation of state for H₂O (Saul and Wagner 1989) and assuming that the dissolution of silicates has no excess volume of mixing. In one experiment the fluid density after the run was greater than unity, and thus needed to be determined from the melting point of ice (Wagner et al. 1994, Tanaka 2000). Oxygen fugacity was not strictly buffered in our experiments but it was probably close to the Re-ReO buffer due to the use of a rhenium gasket. However, I do not consider the oxygen fugacity to be important because Zr⁴⁺ is the only stable oxidation state of over a wide range of redox conditions (Aja et al. 1995).

Attainment of equilibrium between zircon and the surrounding fluid is indicated by the following observations: (i) when the temperature in a diamond anvil cell was held constant, the size of the crystal in the fluid-filled chamber was not changing; (ii) dissolution continued only when the temperature was further increased, and (iii) when I decreased the temperature while zircon was still present, the grain grew in size again. In order to check for potential zircon redistribution due to minor temperature gradients I also performed a long-term experiment in which temperature was raised to 700 °C, then with 0.9-1.5 °C min⁻¹ to 870 °C and kept constant for 2.5 hrs. Temperature control during this run was performed with the help of a thermostat, ensuring <1 °C difference between the two diamond anvils readings at all times.

Most of our experiments were performed by adding a relatively large piece of Brazilian quartz as silica activity buffer (Fig. 4-1). I also performed one exploratory experiment in which silica activity was buffered by enstatite and forsterite ($a_{\text{qz}} \sim 0.5$), and one experiment with pure baddeleyite (ZrO₂) in the absence of silica. Zircon solubility was also investigated in an aqueous

solution containing 15 wt. % NaCl and one containing 4.5 wt. % dissolved albite. Albite was added as regular chips of natural albite. Due to the incongruent dissolution of albite, transient precipitation of fine-grained crystals occurred at 520 °C, which redissolved at 590 °C. In order to compare our zircon solubility data with the behavior of other high field strength elements, one experiment investigated thorite solubility (ThSiO_4) in pure water with silica activity buffered by quartz.

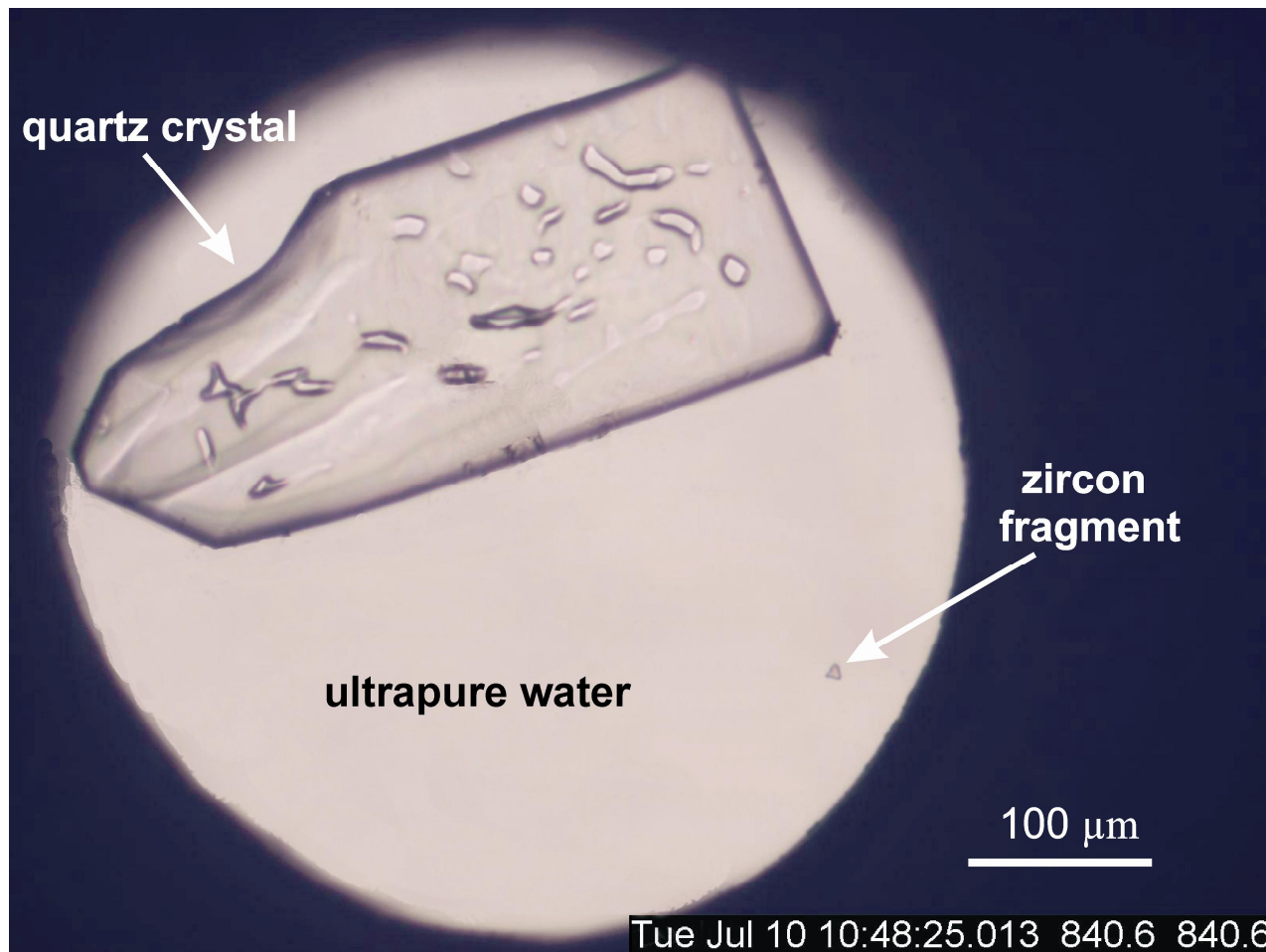


Fig. 4-1. View through the diamond anvil cell during an experiment containing zircon, excess quartz and aqueous fluid at 841 °C and 11.3 kbar. The zircon crystal originally measured 1 μm in thickness and 4 μm along each side, with its mass corresponding to 1.94 ppm Zr by weight of the total charge excluding undissolved quartz.

I have verified our zircon solubilities obtained in the HDAC by an independent experiment in a piston-cylinder apparatus where zircon-saturated fluid was trapped as fluid inclusions in quartz and subsequently analyzed by laser ablation ICP-MS. A $\text{Pt}_{95}\text{Rh}_{05}$ capsule of 5.0 mm O.D., 4.4 mm I.D. and 10 mm length was loaded with small pieces of zircon from the same grain as used in other experiments (corresponding to 50 wt. % of the charge), one large piece of quartz single crystal (~2.5 x 2.5 x 3 mm) and ultrapure water spiked with 250 ppm Rb and 250 ppm Cs

(added as chlorides) to provide an internal standard for the laser ablation analyses. The capsule was sealed by the method described by Audéat and Bali (2010), which allows the use of high fluid/solid ratios and prevents fluid loss during welding. The experiment was run in a ½-inch MgO assembly at 900 °C and 15 kbar for 40 hours, with a 5 % correction for assembly friction applied to pressure. These conditions are representative of our diamond anvil cell experiments. Quartz recrystallization during the experiment led to the formation of new overgrowths containing large, primary fluid inclusions measuring up to 100 μm in diameter. Since these fluid inclusions can have formed only after substantial quartz dissolution and reprecipitation, the activity of quartz must have been equal to unity.

4.3. Results

I performed eight zircon solubility experiments in aqueous fluid at 865-1025 °C and 6.2-20.0 kbar. Zircon solubilities determined in the presence of excess quartz in pure H₂O are listed in Table 4-1 and plotted in Fig. 4-2.

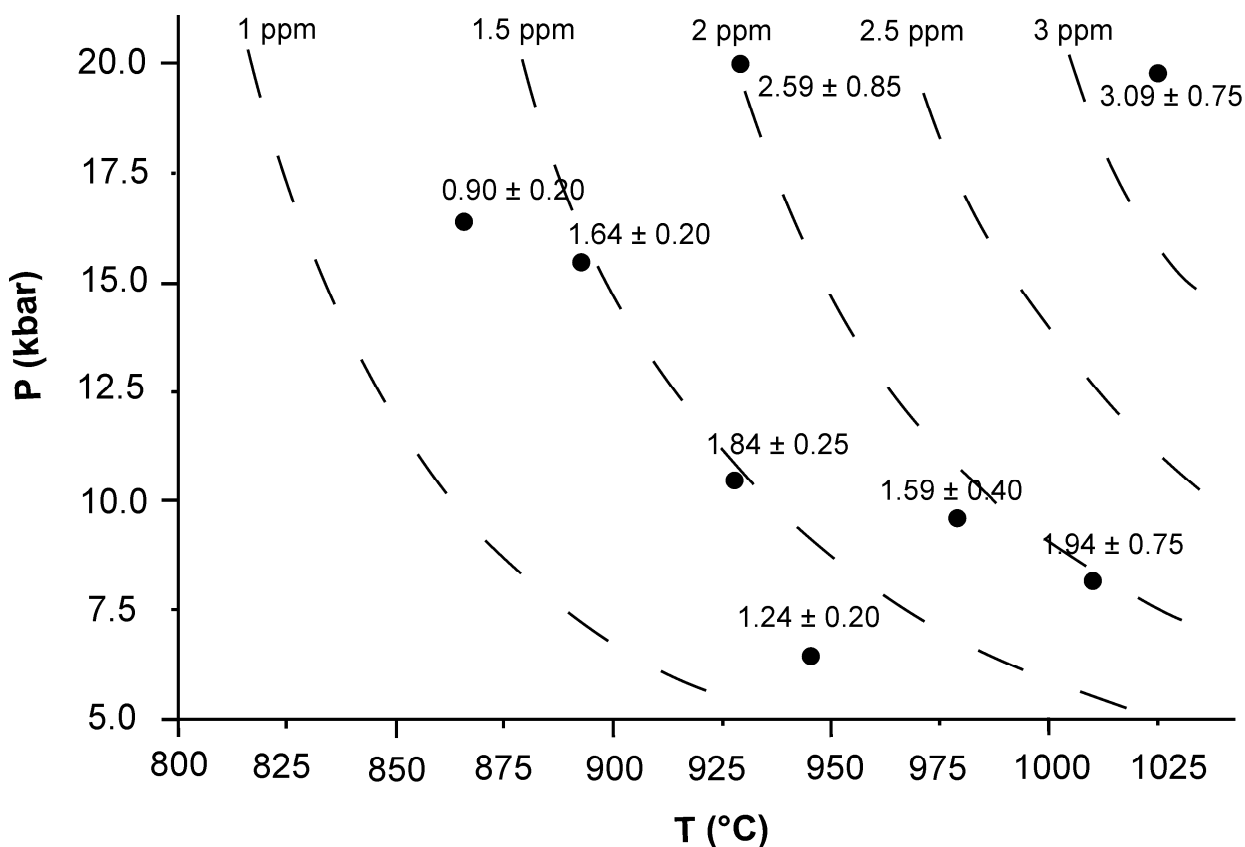


Fig. 4-2. Temperature-pressure diagram showing measured zirconium solubilities in pure water in the presence of quartz ($a_{qz} = 1$) and solubility isopleths predicted by the density model (Eq. 4-5).

Values obtained by dissolution experiments in the HDAC range from 0.90 to 3.09 ppm Zr, and increase with increasing temperature or pressure.

From the piston cylinder experiment performed at 900 °C / 15 kbar I was able to analyze 5 synthetic fluid inclusions. Resulting zircon solubilities range from 1.8-4.7 ppm Zr, with an average of 2.89 ± 1.15 ppm Zr. Within analytical uncertainty, this value is in agreement with the results obtained in the HDAC (Table 4-1).

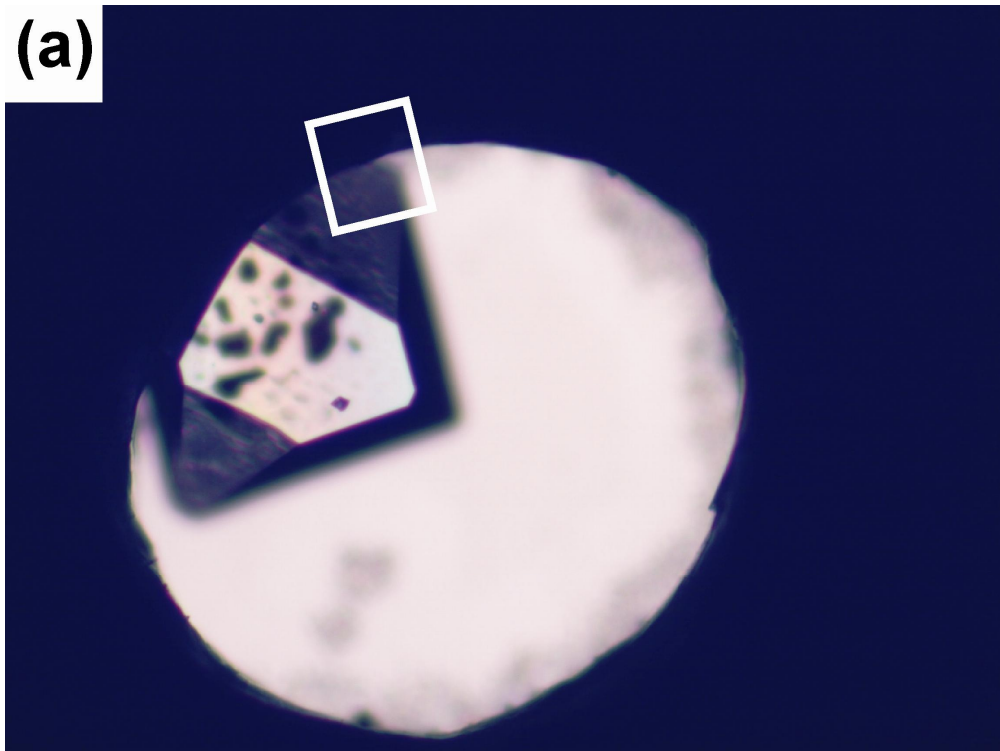
Table 4-1. Experimental conditions and measured mineral solubilities

Mineral	Instrument	Silica buffer	Fluid	T (°C)	P (kbar)	Concentration		
						ppm mineral	ppm Zr or Th	log m Zr or Th
zir	HDAC	qz	H ₂ O	926	10.30	3.7 (± 0.5)	1.84 (± 0.25)	-4.69 (± 0.06)
zir	HDAC	qz	H ₂ O	890	15.88	3.3 (± 0.4)	1.64 (± 0.20)	-4.74 (± 0.05)
zir	HDAC	qz	H ₂ O	865	16.20	1.8 (± 0.4)	0.90 (± 0.20)	-5.01 (± 0.10)
zir	HDAC	qz	H ₂ O	943	6.22	2.5 (± 0.4)	1.24 (± 0.20)	-4.87 (± 0.07)
zir	HDAC	qz	H ₂ O	1015	8.12	3.9 (± 1.5)	1.94 (± 0.75)	-4.67 (± 0.17)
zir	HDAC	qz	H ₂ O	983	9.95	3.2 (± 0.8)	1.59 (± 0.40)	-4.76 (± 0.11)
zir	HDAC	qz	H ₂ O	930	19.99	5.2 (± 1.7)	2.59 (± 0.85)	-4.55 (± 0.14)
zir	HDAC	qz	H ₂ O	1025	19.85	6.2 (± 1.5)	3.09 (± 0.75)	-4.47 (± 0.11)
zir	HDAC	fo-en	H ₂ O	720	10.00	0.9 (± 0.3)	0.45 (± 0.15)	-5.31 (± 0.14)
zir	HDAC	qz	H ₂ O, 15 wt% NaCl	893	14.4	9.0 (± 3.0)	4.48 (± 1.49)	-4.31 (± 0.14)
zir	HDAC	qz	H ₂ O, 4.5 wt% Ab	690	12.8	2.6 (± 0.4)	1.29 (± 0.2)	-4.85 (± 0.07)
bad	HDAC	-	H ₂ O	930	15.87	48 (± 15)	35.5 (± 11.1)	-3.41 (± 0.14)
thr	HDAC	qz	H ₂ O	680	7.45	1.6 (± 0.8)	1.15 (± 0.57)	-5.30 (± 0.22)
zir	piston cylinder	qz	H ₂ O	900	15.00	5.8 (± 2.3)	2.89 (± 1.15)	-4.50 (± 0.17)

ab - albite, bad - baddeleyite, en - enstatite, fo - forsterite, qz . quartz, thr - thorite, zir - zircon. Uncertainties in the mass of loaded zircon grains are reported in parentheses, whereas in the case of the piston cylinder experiment the uncertainty refers to the 1 sigma standard deviation of the 5 fluid inclusion analyses.

In our long-term HDAC experiment, which was performed with a zircon piece about 100 times larger than in other runs, I noticed that small zircon crystals started to grow along the upper gasket rim above 820 °C and while the temperature was held constant at 870 °C (Fig. 4-3). The appearance of new zircon crystals must be due to mass redistribution in response to a small temperature gradient. When the experiment was stopped after 7.5 hrs, at least 50 ppm Zr had precipitated along the upper gasket rim. This value was calculated from the combined volume of several of these newly formed zircon crystals and represents a minimum estimate because other crystals grown elsewhere may have been missed. At pressure and temperature of this experiment equilibrium zircon solubility was 2.5 ppm Zr at most, hence the amount of Zr that was re-precipitated was at least 20 times higher than the equilibrium solubility.

(a)



(b)

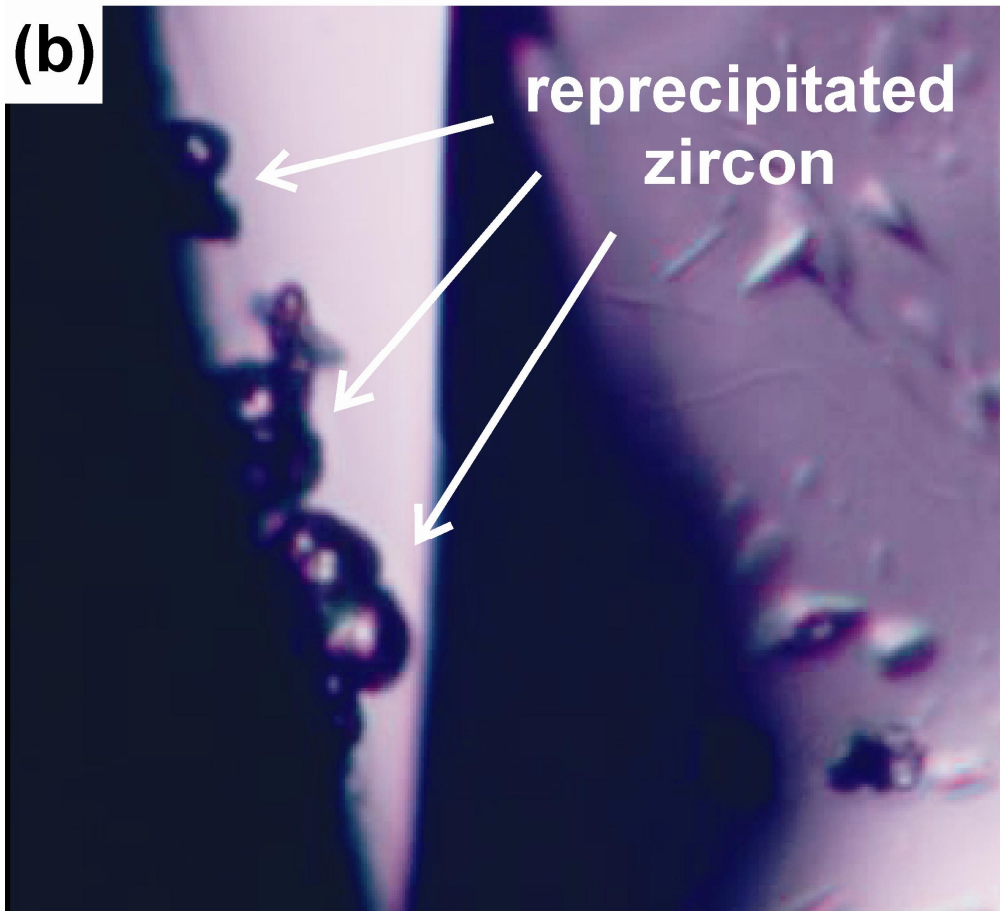


Fig. 4-3. Zircon reprecipitation after long-term experiment. (a) View through the diamond anvil cell containing a large quartz crystal after the run, (b) detailed view of re-precipitated zircon crystals on the gasket wall.

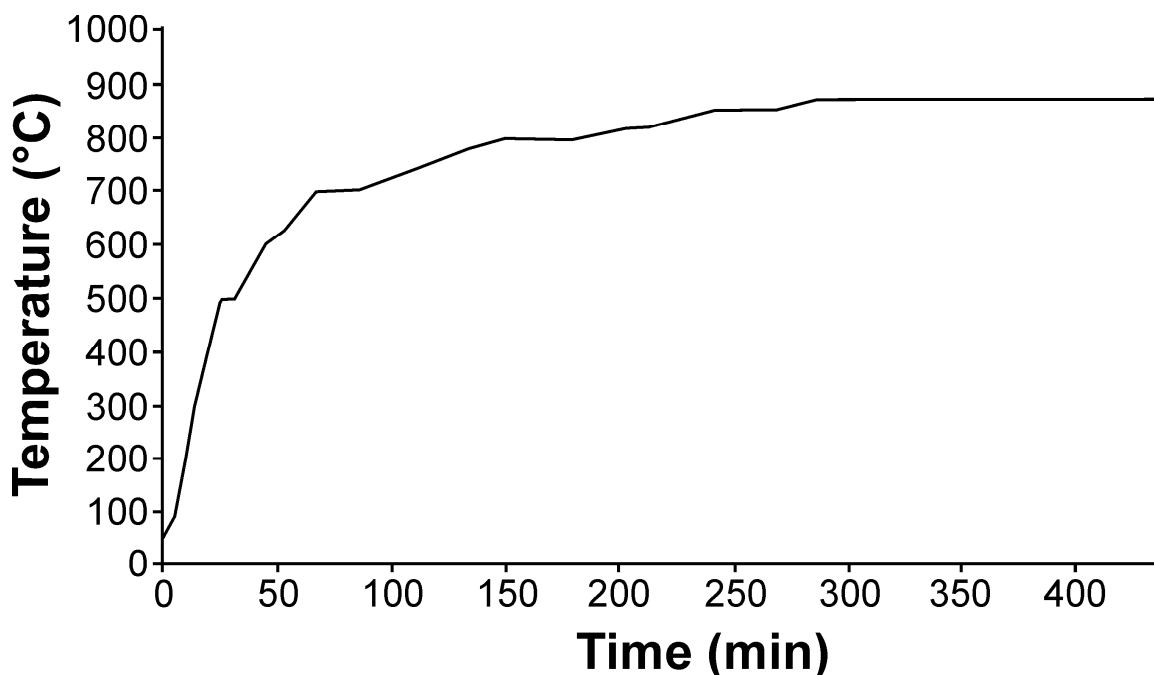


Fig. 4-4. Time vs. temperature path of the long-term experiment.

Zircon solubility measured at 720 °C and 10.00 kbar in the presence of forsterite and enstatite ($a_{\text{qz}} = 0.363$) is 0.45 ± 0.15 ppm Zr (Table 4-1). At the same pressure and temperature, the calculated solubility buffered by quartz is ~ 0.36 ppm Zr. The baddeleyite solubility (in the absence of SiO_2) is 35.5 ± 11.1 ppm Zr at 930 °C and 15.8 kbar (Table 4-1), representing an increase by a factor of ~ 15 compared to zircon solubility at quartz saturation at these conditions. These results demonstrate that the zirconium solubility increases with the decreasing activity of silica, consistent with the lower Gibbs energy of zircon relative to baddeleyite and quartz (Ferry et al. 2002, O'Neill 2006, Newton et al. 2005, 2010).

4.4. Discussion

4.4.1. Evidence for attainment of equilibrium

Several experimental methods have been employed to measure the solubility of very insoluble minerals in aqueous fluids at high temperatures and pressures: (i) crystal weight loss experiments in a piston cylinder apparatus (e.g., Ayers and Watson 1993, Tropper and Manning 2005, Antignano and Manning 2008) or in an internally heated pressure vessel (Rapp et al. 2010), (ii) *in situ* synchrotron-XRF (SXRF) measurements of the Zr content of fluids equilibrated with zircon in the HDAC (Manning et al., 2008), and (iii) direct observation of dissolving mineral grains in the HDAC (Audétat and Keppler 2005, Baier et al. 2008). Compared to early studies the

weight loss technique has been considerably improved by minimizing temperature gradients and discriminating more rigorously between quench-solute and transport crystals (Tropper and Manning 2005, Antignano and Manning 2008). However, between these newer results and the solubility data obtained by other techniques there still remain discrepancies of more than one order of magnitude; for rutile solubility in H₂O see Tropper and Manning (2005), Audétat and Keppler (2005), and Rapp et al. 2010). Audétat and Keppler (2005) argued that the rutile solubility data obtained by weight loss technique may be too high due to mobilization and reprecipitation of the solute in response to small thermal gradients. On the other hand, Tropper and Manning (2005) and Antignano and Manning (2008) argued that the solubilities obtained by *in situ* observations of dissolving mineral grains in the HDAC may be too low due to slow dissolution kinetics. Rutile solubilities determined by SXRF in fluids containing dissolved albite agree with results obtained from weight-loss experiments, but at the same time demonstrate that in dilute fluids the measured concentrations continuously increased with time. The latter was interpreted to result from sluggish reaction, although it is not quite clear why the dissolution should proceed slower in dilute fluids than in more silica-rich fluids. An alternative explanation for this observation is that the increasing amount of Ti detected in the beam path was not due to an increasing amount of Ti in the fluid, but due to reprecipitation of TiO₂ within the sample chamber. Our long-term zircon dissolution experiment demonstrates that substantial amounts of the solid phase, exceeding the equilibrium solubility by more than one order of magnitude, can be dissolved and advected by fluid within several hours. Consequently, experiments of long duration such as those in a piston-cylinder apparatus can be significantly affected by the dissolution and reprecipitation (*cf.* Tropper and Manning 2005). On the other hand, heating rates used in the HDAC experiments do not prevent attainment of equilibrium. First, zircon solubilities determined from synthetic fluid inclusions are within analytical uncertainty identical to those obtained in the HDAC, and, second, *in situ* SXRF studies revealed dissolution rates to be fast for metamict and crystalline zircons, the latter reaching equilibrium within 10-20 minutes at 500 °C (Schmidt et al. 2006, Petitgirard, pers. communication 2009). In view of these observations and the rapid response of zircon dissolution to changes in the heating rate during our HDAC experiments I regard our solubility measurements as representative.

4.4.2. Thermodynamic model for zircon solubility

Zircon dissolution into aqueous fluid is described by the following equilibrium:



where SiO_2 (aq) collectively refers to monomer and oligomer silica species in the fluid (*cf.* Zotov and Keppler 2000, Newton and Manning 2002, 2003). The Zr solubility is thus expected to vary inversely with the activity of silica in the fluid at pressure and temperature of interest. In our first series of experiments, zircon dissolution was buffered by quartz, as follows:



If the activity coefficient of ZrO_2 in the fluid is constant over the pressure, temperature and concentration range studied, the concentration of ZrO_2 in the fluid is directly proportional to equilibrium constant, K .

Mineral solubilities at elevated temperature and pressure are accurately described by a density model (Fournier and Potter 1982, Manning 1994):

$$\log K \approx \log m_{\text{ZrO}_2} = a + \frac{b}{T} + c \log \rho_{\text{H}_2\text{O}} \quad (4-4)$$

which accounts for the temperature dependence and volume of dissolution reaction due to the formation of hydrated species (Dolej- & Manning 2010). This functional form accounts for temperature- and pressure-dependent standard reaction volume and is thus more appropriate and accurate than conventional expansions using constant reaction enthalpy, entropy and volume. The eight zircon solubilities in aqueous fluid at $a_{\text{qz}} = 1$ were fitted by the least squares method yielding: $a = -1.51$, $b = -3800$ and $c = 1.52$. The results are illustrated in Figure 4-5. For practical calculations I provide fit to Zr concentrations in (ppm), c_{Zr} , in the aqueous fluid:

$$\log c_{\text{Zr}} = a + \frac{b}{T} + c \log \rho \quad (4-5)$$

with $a = 3.45$, $b = -3800$, and $c = 1.52$.

4.4.3. Effect of additional solute components

Natural aqueous fluids contain elevated concentrations of chlorine (arising from subducted sea water; Manning 2004) or aluminosilicate solute at high temperature and pressure (Manning 2004, Hack et al. 2007). The effect of silica activity on zirconium solubility was explored by two additional experiments: (i) zircon solubility at the forsterite-enstatite buffer, and (ii) baddeleyite

(ZrO₂) solubility in an SiO₂-free aqueous fluid (Tab. 4-1). The zircon solubility measured at 720 °C and 10.0 kbar in the presence of forsterite and enstatite ($a_{\text{qz}} = 0.363$) is 0.45 ± 0.15 ppm Zr. At the same pressure and temperature, the calculated solubility buffered by quartz is 0.36 ppm Zr. The baddeleyite solubility (in the absence of SiO₂) was found to be 35.5 ± 11.1 ppm Zr at 930 °C and 15.8 kbar and it represents an increase by a factor of 15 over the Zr solubility at $a_{\text{qz}} = 1$ (2.47 ± 0.90 ppm Zr, interpolated experiments at 926-930 °C; Table 4-1). As expected from Eq. (4-2) these experimental results show that the zirconium solubility increases with the decreasing activity of silica, consistent with the zircon stability with respect to baddeleyite and quartz (Ferry et al. 2002, O'Neill 2006, Newton et al. 2005, 2010) and with the absence of Zr-Si complexes in aqueous fluid.

The solubility of Ti and Zr remains the lowest at quartz saturation and it increases as the activity of silica decreases (Antignano and Manning 2008; this study), consistent with the absence of metal-Si complexes. In contrast, the formation of Al-Si complexes (Pokrovski et al. 1996, Beitter et al. 2008) significantly promotes the Al solubility in SiO₂-saturated fluids (Manning 2007, Fig. 4-7). In summary, the solubility of HFSE remain very low, thus such elements cannot be substantially mobilized in the aqueous fluids at elevated temperatures and pressures. Zr concentration in pure water at 1000 °C and pressure of 3 GPa is 8.2 ± 5.2 ppm. Experimental results of mineral-fluid partitioning of Zr at temperature and pressure of the mantle wedge (900-1100 °C, 2-3 GPa, Ayers et al. 1997) shows that rutile and garnet are the two phases that most efficiently incorporate Zr. Instead, the partitioning between clinopyroxene and aqueous fluid is close to 1, and for orthopyroxene and olivine is below unity, showing an incompatible behavior.

The presence of alkali chloride or aluminosilicate may substantially increase the solubility of high field strength elements (Korzhinskaya and Ivanov 1987, Audétat and Keppler 2005, Antignano and Manning 2008). In order to check for the magnitude of this effect I have carried out additional experiments, one using a saline fluid with 15 wt. % NaCl, and the other one containing 4.5 wt. % dissolved albite, both saturated with quartz. In the NaCl-bearing fluid the zircon solubility at 893 °C, 14.4 kbar and $a_{\text{qz}} = 1$ is 4.48 ± 1.49 ppm Zr. This represents a solubility increase by a factor of 3 over the solubility in pure H₂O fluid at the same conditions (1.42 ppm Zr) and thus may imply formation of zirconium-chloride complexes, as suggested by Korzhinskaya and Ivanov (1988) and Aja et al. (1995). Zircon solubility at 690 °C, 12.8 kbar and $a_{\text{qz}} = 1$ in aqueous fluid with 4.5 wt. % albite solute is 1.29 ± 0.21 ppm Zr. This value is about five times higher than the predicted solubility in pure water at the same conditions (0.31 ppm Zr) and therefore suggests some interaction between aluminosilicate anions and Zr in the fluid.

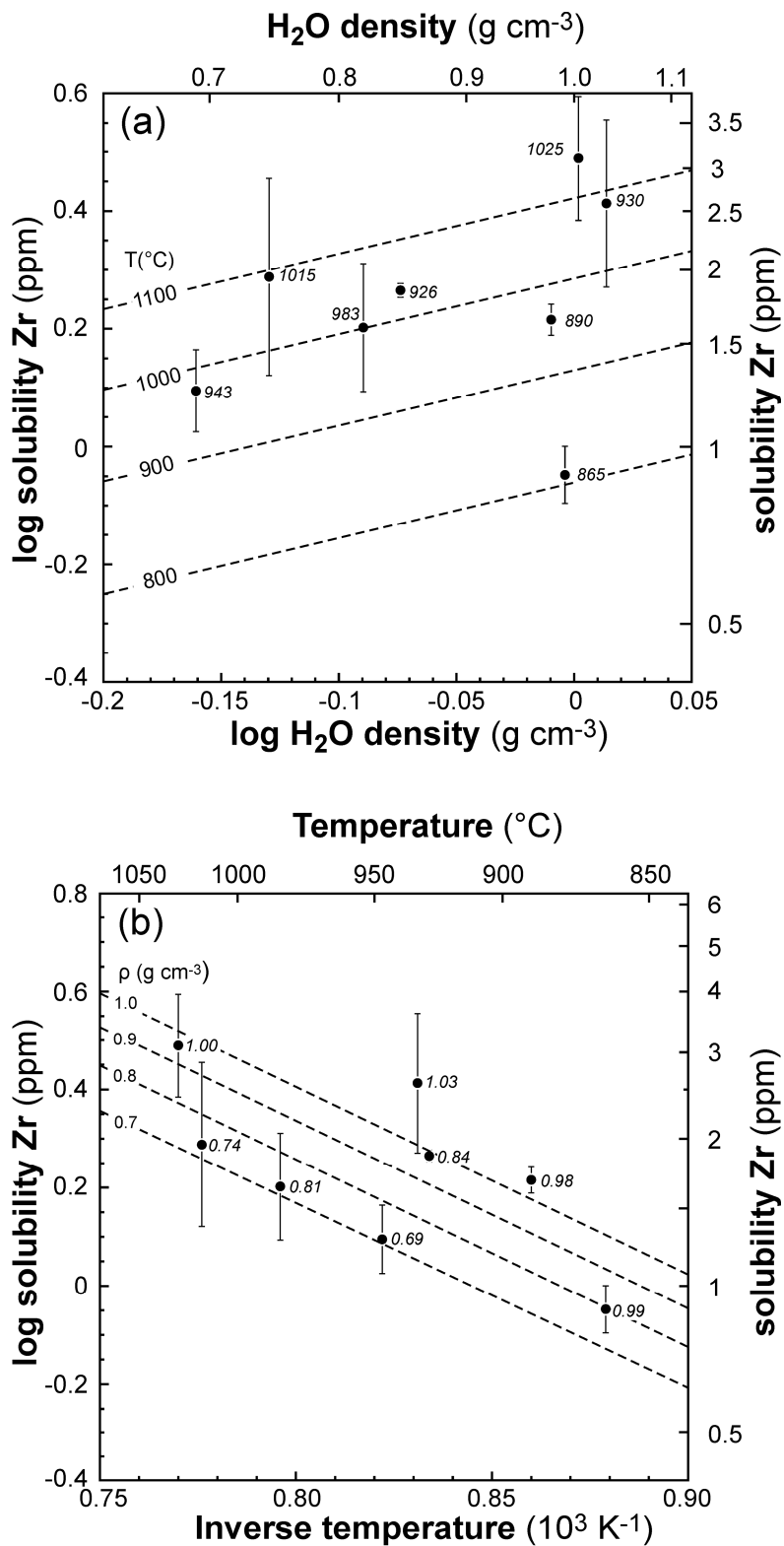


Fig. 4-5. Density model model for Zr solubility in H₂O: (a) log solvent density vs. log solubility plot; (b) inverse temperature vs. log solubility plot. Experimental measurements are shown by solid circles whereas the temperature isopleths and isochores are shown as dashed lines, respectively.

4.4.5. Comparison with other HFSE

In order to compare our zircon solubility data with the behavior other high field strength elements I have also performed an experiment with thorite (ThSiO₄), which is isostructural with

zircon. Thorite solubility at 680 °C, 7.5 kbar and $a_{qz} = 1$ is 1.15 ± 0.57 ppm Th (Table 4-1), in agreement with the solubility of 4.5 ppm Th obtained from fluid inclusions synthesized in a piston cylinder apparatus at 800 °C and 27.5 kbar (Bali et al. 2009). The calculated zircon solubility at 680 °C, 7.5 kbar is 0.23 ppm Zr (Eq. 4-5), hence the solubilities of Th and Zr in quartz-saturated H₂O are comparable.

Our experimental results are in agreement with the generally low solubilities observed for other HFSE (Audétat and Keppler 2005, Antignano and Manning 2008, Baier et al. 2008), although systematic differences among different HFSE emerge. Fig. 4-6 illustrates a monotonous decline in the solubility as ionic radius increases.

The highest solubilities are shown by Ti, Nb and Ta, which are the HFSE with the smallest ionic radius whereas the lowest are shown by Zr and Th, which have the largest ionic radii. This trend is probably not directly related to ionic radius, but to the stabilization of different phases (pure oxides for Si, Al, Ti, mixed oxides for Nb and Ta and silicates for Zr and Th).

4.4.6. Origin of the negative Zr anomalies in arc magmas

The HFSE negative anomaly in arc magmas is thought to be dependent on a very low concentration of such elements in the fluid released from the subducted slab (Audétat and Keppler 2005, Baier et al. 2008, Antignano and Manning 2008). The average Zr content of the primitive upper mantle is estimated at 10.5 ppm Zr (McDonough and Sun 1995). The Zr concentrations in rock-forming minerals are much lower than the whole-rock content, < 0.02 ppm in olivine, 0.06 to 0.139 ppm in orthopyroxene and 4.5 to 45 ppm in clinopyroxene (Garrido et al. 2005, Bea et al. 2006, Francis and Minarik 2008). These phases account for ~ 20 % of the whole-rock Zr budget, with the remainder being hosted by zircon (Liati et al. 2004, Zheng et al. 2006, 2008, Song et al. 2009).

I can, therefore, apply our zircon solubility model to fluids percolating through zircon-bearing peridotites. During melting in the mantle wedge, Zr is strongly partitioned into the melt. Mineral/melt partition coefficients at 1300 °C and 1 atm are: 0.001 for olivine, 0.005 for orthopyroxene, and 0.1 for clinopyroxene (Mallmann et al. 2000).

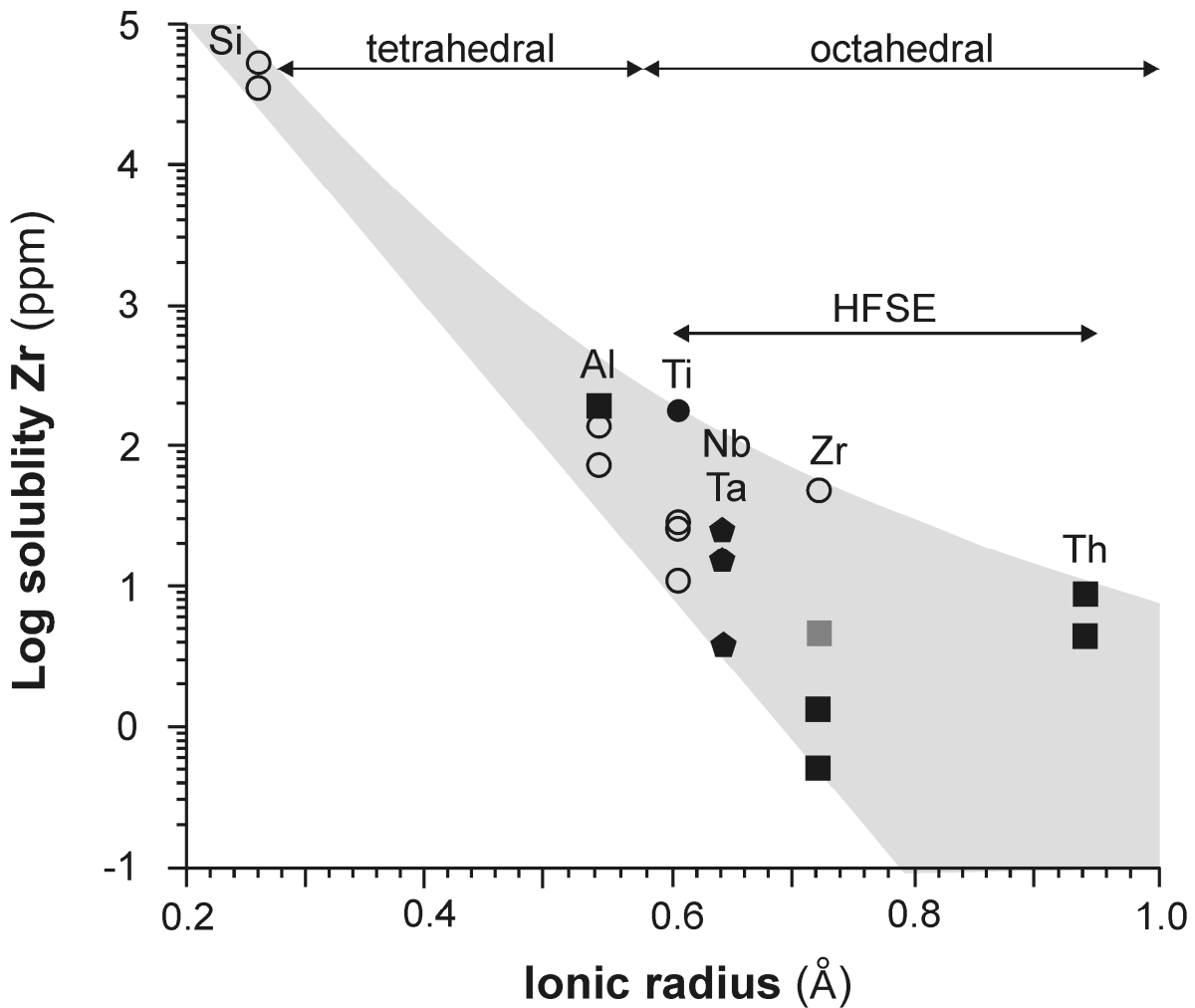


Fig. 4-6. Ionic radius vs. solubility in H₂O: circles indicate solubility of oxides, squares represent silicate solubilities and pentagons are those of tantalates or niobates. Open symbols refer to experiments without silica activity buffer, solid symbols refer to experiments in the presence of quartz or a silicate, gray symbol refers to experiment performed in presence of salt (Manning 1994, 2007, Antignano and Manning 2008, Baier et al. 2008, Bali et al. 2009).

The Zr contents of basaltic arc magmas ranges from 40 to 180 ppm and are believed to reflect variable degrees of partial melting (Thirlwall et al. 1994). This is comparable to the Zr concentrations in primary basalts, from 74 to 100 ppm, (Arevalo and McDonough 2010). The magnitude of element enrichment or depletion in partial melts due to fluxing by slab-derived aqueous fluids can be estimated by mass balance calculations.

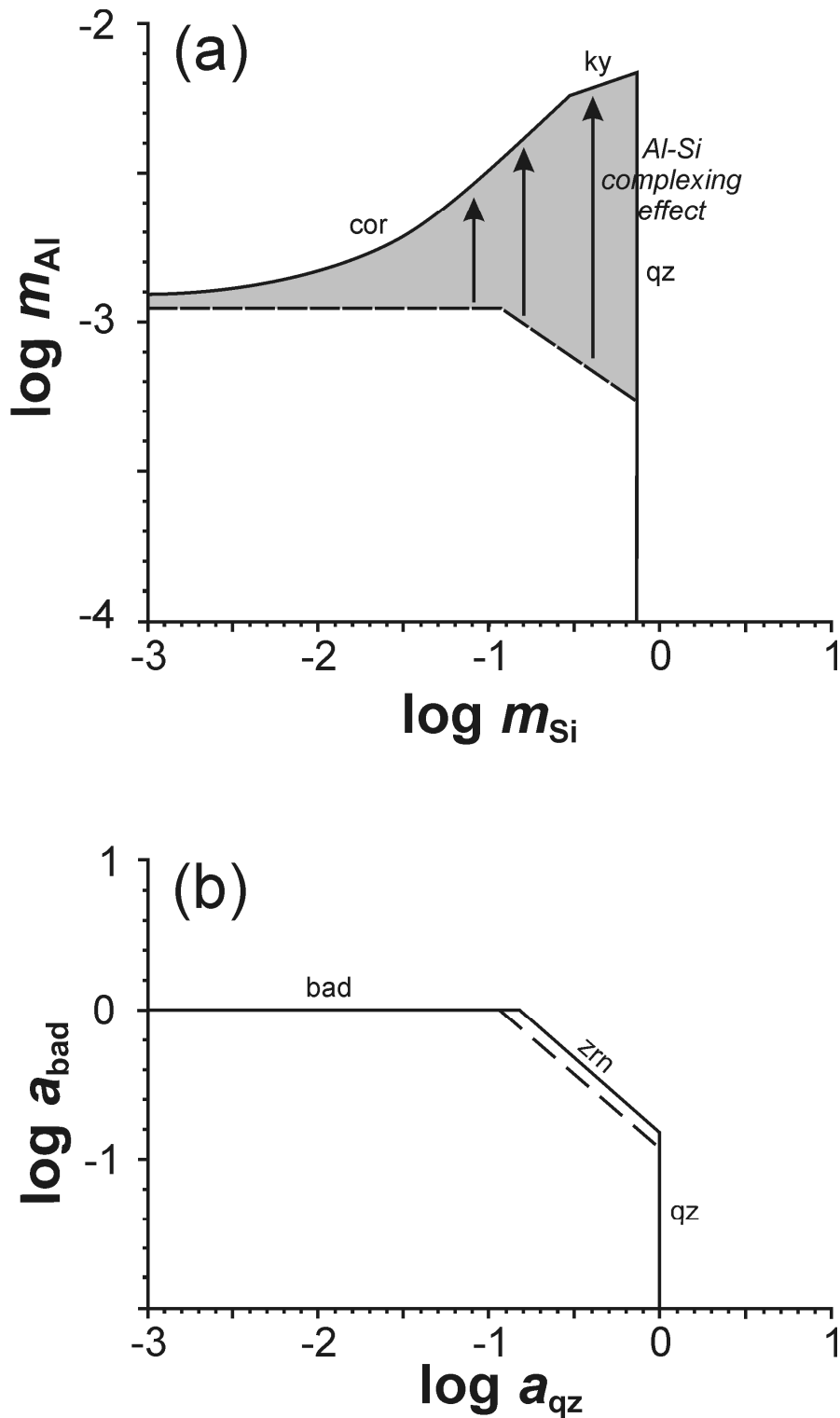


Fig. 4-7. Activity-activity diagrams illustrating the effect of complexing on the enhancement of solubility: (a) $\log m_{\text{Si}}$ vs. $\log m_{\text{Al}}$ plot at 700 °C and 10 kbar (Manning 2007); (b) a_{qz} vs. a_{bad} with zircon saturation surface at 700 °C and 10 kbar (solid line) and 1000 °C and 20 kbar (dashed line). This figure shows the different effect of silica activity on the solubility of Al and Zr. While the solubility of Al is enhanced at high silica activity due to the formation of aluminosilicate species, a similar effect of silica is not observed for zirconium. However, our experiment with albite suggests that the combined presence of Al and Si may indeed significantly enhance Zr solubility, although zircon remains very poorly soluble.

The concentration of constituent i in the melt produced by fluid fluxing of the mantle wedge, c_i^{hl} , is given by:

$$c_i^{hl} = (1 - w) \cdot c_i^{pl} + w \cdot c_i^{fl} \quad (4-6)$$

where c_i^{pl} and c_i^{fl} are the concentrations of i in the primitive melt and aqueous fluid respectively, and w is the mass fraction of H₂O dissolved in the melt. The Zr concentration in the partial melt is initially defined by Rayleigh equilibrium or fractional melting (e.g., Albarède 1995) using mineral/melt partition coefficients (see above), whereas the Zr abundance in the fluid is dictated by solubility of zircon present in peridotite.

Fig. 4-8 illustrates the effect of fluid-assisted vs. fluid-absent partial melting on the Zr, K and Cl content of primitive mantle melts. Due to the low solubility of Zr in the fluid the concentration of Zr in partial melts is virtually the same in both melting regimes. By contrast, the concentrations of the fluid-mobile elements K and Cl, are substantially higher in melts produced by fluid fluxing ($c_i^{fl} \gg c_i^{pl}$) than in melts produced without fluid fluxing. These results illustrate the efficiency of enrichment of magmas by fluid-mobile elements but not so in HFSE, producing the characteristic *relative* depletion in HFSE in natural arc magmas (*cf.* Pearce and Stern 2006).

4.5. Conclusions

I measured zircon solubility in aqueous fluids at 865-1025 °C and 6.22-19.99 kbar using an externally heated hydrothermal diamond anvil cell. The zircon solubility in aqueous fluids is very low, ranging from 1.0-3.3 ppm at $a_{qz} = 1$. The results were fitted to a three-parameter thermodynamic model that allows prediction of Zr solubility over a wide range of pressures and temperatures in the upper mantle. With decreasing activity of quartz, the Zr solubility increases, thus there is an inverse relationship between ZrO₂ and SiO₂ concentrations that rules out the existence of Zr-Si aqueous complexes. Addition of 4.5 wt. % albite to quartz-saturated fluids increases zircon solubility by a factor of five, suggesting some interaction of Zr⁴⁺ with aluminosilicate anions. In contrast, addition of 15 wt. % NaCl to the fluid increases zircon solubility by factor of three, in agreement with the formation of zirconium-chloride complexes suggested by Korzhinskaya and Ivanov (1988) and Aja et al. (1995).

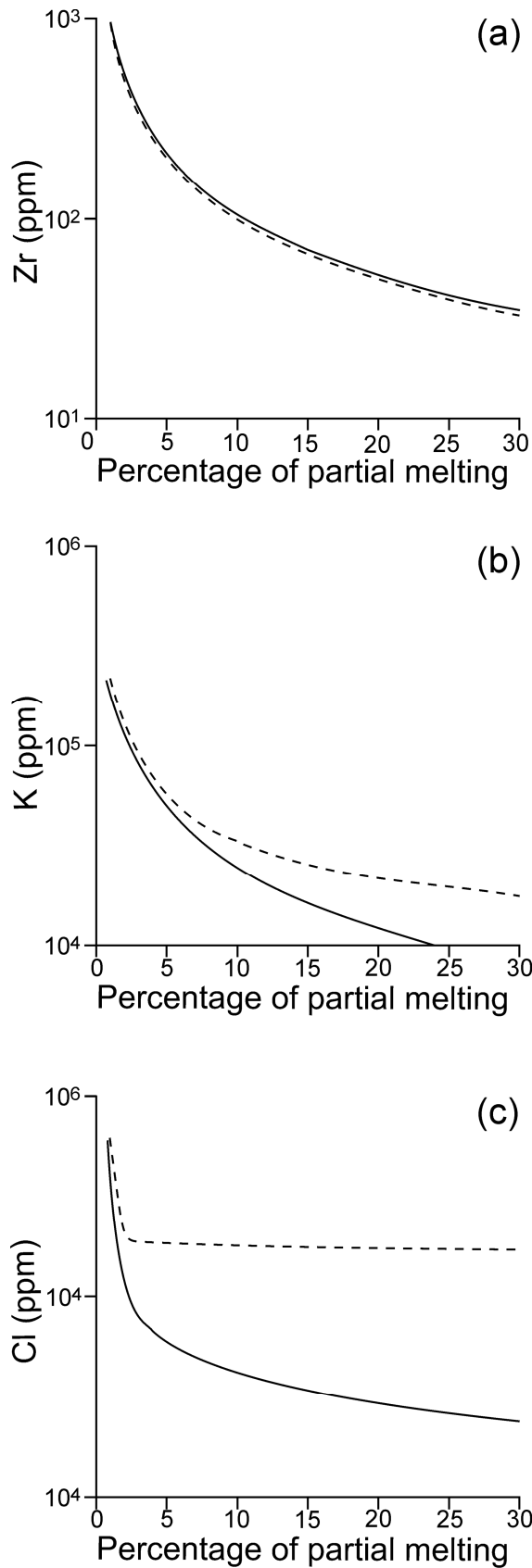


Fig. 4-8. Calculations of the composition of partial mantle melts as a function of the degree of fluid-assisted (stippled line) vs. "dry" (solid line) melting: (a) Zr content (b) K content (c) Cl content. The Zr content of the fluid was determined by Eq. 4-5, whereas the concentrations of K and Cl were taken from the estimated slab to arc flux ratios published by Jarrard (2003).

The solubility of Zr in aqueous fluids is generally similar to that of other HFSE, and a systematic behavior can be recognized as a function of ionic radius. Mass balance calculations demonstrate that the Zr content of slab-derived fluids is too low to produce a detectable enrichment of partial mantle melts produced by fluid fluxing. The relative HFSE depletion observed in arc magmas (e.g., Pearce and Stern 2006) can thus satisfactorily be explained by the low solubility of these elements in slab-derived aqueous fluids.

4.6. References

- Aja S. U., Wood S. A., Williams-Jones A. E. (1995): The aqueous geochemistry and the solubility of some Zr-bearing minerals, *Applied Geochemistry*, 10, 603-620.
- Albaréde F. (1995): Introduction to geochemical modeling, *Cambridge University Press*.
- Antignano A., Manning C. E. (2008): Rutile solubility in H₂O, H₂O-SiO₂, and H₂O-NaAlSi₃O₈ fluids at 0.7-2.0 GPa and 700-1000 °C: implications for mobility of nominally insoluble elements. *Chemical Geology*, 255, 283-293.
- Arevalo R. Jr., McDonough W. F. (2010): Chemical variations and regional diversity observed in MORB, *Chemical Geology*, 271, 70-85.
- Audétat A., Bali E. (2010): A new technique to seal volatile-rich samples into platinum capsules, *European Journal of Mineralogy*, 22, 23-27.
- Audétat A., Keppler H. (2005): Solubility of rutile in subduction zone fluids, as determined by experiments in the hydrothermal diamond anvil cell. *Earth and Planetary Science Letters*, 232, 393-402.
- Ayers J. (1998): Trace element modeling of aqueous fluid-peridotite interaction in the mantle wedge of subduction zones, *Contribution to Mineralogy and Petrology*, 132, 390-404.
- Ayers J. C., Dittmer, S. K., Layne, G. D. (1997) Partitioning of elements between peridotite and H₂O at 2.0-3.0 GPa and 900-1100 degrees C, and application to models of subduction zone processes, *Earth and Planetary Science Letters*, 150, 381-398.
- Ayers J. C., Watson E. B. (1993): Rutile solubility and mobility in supercritical aqueous fluids, *Contribution to Mineralogy and Petrology*, 114, 321– 330.
- Baier J., Audétat A., Keppler H. (2008): The origin of the negative niobium tantalum anomaly in subduction zone magmas, *Earth and Planetary Science Letters*, 267, 290–300.
- Bali E., Audétat A., Keppler H. (2009): Mobility of U and Th in subduction zones fluids ó A synthetic fluid inclusion study. *Geochimica et Cosmochimica Acta*, 73 (Suppl.), A80.
- Bassett W. A., Shen A. H., Buckum M. (1993): A new diamond anvil cell for hydrothermal studies to 2.5 GPa and from 190 °C to 1200 °C. *Review of Scientific Instruments*, 64, 2340–2345.

- Bassett W.A., Shen A.H., Buckum M., Chou I.-M. (1993): Hydrothermal studies in a new diamond anvil cell up to 10 GPa and from 190 °C to 1200 °C. *Pure and Applied Geophysics*, 141, 487– 495.
- Bea F., Montero P., Ortega M. (2006): A LA-ICP-MS evaluation of Zr reservoirs in common crustal rocks: implication for Zr and Hf geochemistry, and zircon forming processes, *Canadian Mineralogist*, 44, 693-714.
- Beitter T., Wagner T., Markl G. (2008): Formation of kyanite-quartz veins of the Alpe Sponda, Central Alps, Switzerland: implication for Al transport during regional metamorphism, *Contributions to Mineralogy and Petrology*, 156, 689-707.
- Bocchio R., De Capitani L., Ottolini L., Cella F. (2000): trace element distribution in eclogites and their clinopyroxene-garnet pair: a case of study from Soazza (Switzerland), *European Journal of Mineralogy*, 12, 147-161.
- Brenan J. M., Shaw H. F., Phinney D. L., Ryerson F. J. (1994): Rutile-aqueous fluid partitioning of Nb, Ta, Hf, Zr, U and Th: implications for high strength element depletions in island-arc basalts, *Earth and Planetary Science Letters*, 128, 327-339.
- Brenan J. M., Shaw H. F., Ryerson F. J., Phinney D. L. (1995) Mineral-aqueous fluid partitioning of trace elements at 900 °C and 2.0 GPa ó Constraints on the trace element chemistry of mantle and deep-crustal fluids, *Geochimica et Cosmochimica Acta*, 59, 3331-3350.
- Dolej- D., Manning C. E. (2010): Thermodynamic model for mineral solubility in aqueous fluids: theory, calibration, and application to model fluid-flow systems, *Geofluids*, 10, 20-40.
- Francis D., Minarik W. (2008): Aluminum-dependent trace element partitioning in clinopyroxene, *Contributions to Mineralogy and Petrology*, 156, 439-451.
- Ferry J. M., Newton R. C., Manning C. E. (2002): Experimental determination of the phase equilibria: rutile + magnesite = geikielite + CO₂ and zircon + 2 magnesite = baddeleyite + 2 CO₂, *American Mineralogist*, 87, 1344-1350.
- Foley S. F., Barth M. G., Jenner G. A. (2000): Rutile/melt partition coefficients for trace elements and an assessment of the influence of rutile on the trace element characteristics of subduction zone magmas, *Geochimica et Cosmochimica Acta*, 64, 933-938.
- Fourier R. O., Potter R. W. II (1982): An equation correlating the solubility of quartz in water from 25° to 900 °C at pressure up to 10,000 bars, *Geochimica et Cosmochimica Acta*, 46, 1969-1973.
- Garrido C. J., López Sánchez-Vizcaíno V., Gomez-Pugnaire M. T., Trommsdorff V., Alard O., Bodinier J.-L., Godard M. (2005): Enrichments of HFSE in chlorite-harzburgite produced by high-pressure dehydration of antigorite-serpentinite: Implication for subduction magmatism, *Geochemistry, Geophysics, Geosystems*, 6, doi:10.1029/2004GC000791.

- Kelemen P. B., Shimizu N., Dunn T. (1993): Relative depletion of niobium in some arc magmas and the continental crust: partitioning of K, Nb, La and Ce during melt/rock reaction in the upper mantle, *Earth and Planetary Science Letters*, 120, 111–134.
- Keppler H. (1996): Constraints from partitioning experiments on the composition of subduction-zone fluids, *Nature*, 380, 237-240.
- Kessel R., Schmidt M. W., Ulmer P., Pettke T. (2005): Trace elements signature of subduction-zone fluids, melts and supercritical liquids at 120-180 km depth, *Nature*, 437, 724-727.
- Korzinskaya V. S., Ivanov I. P. (1988): Experimental study of incongruent solubility of zircon in the system ZrO_2 - SiO_2 - H_2O - HCl at $T = 400$ - 600 °C and $P = 1$ kbar, *Doklady Akademii Nauk SSSR*, 229, 970-973.
- Liati A., Leander F., Gebauer D., Fanning C. M. (2004): The timing of mantle and crustal events in South Namibia, as defined by SHRIMP-dating of zircon domains from a garnet peridotite xenolith of the Gibeon Kimberlite Province, *Journal of African Earth Sciences*, 39, 147-157.
- Mallmann G., O'Neill H. St. C. (2009): The crystal/melt partitioning of V during mantle melting as a function of oxygen fugacity compared with some other elements (Al, P, Ca, Sc, Ti, Cr, Fe, Ga, Y, Zr, and Nb), *Journal of Petrology*, 50, 1765-1794.
- Manning C. E. (1994): The solubility of quartz in H_2O in the lower crust and upper mantle, *Geochimica et Cosmochimica Acta*, 58, 4831-4839.
- Manning C. E. (2004): The chemistry of subduction-zone fluids, *Earth and Planetary Science Letters*, 223, 1-16.
- Manning C. E. (2007): Solubility of corundum + kyanite in H_2O at 700 °C and 10 kbar: evidence for Al-Si complexing at high pressure and temperature, *Geofluids*, 7, 258-269.
- Manning C. E., Wilke M., Schmidt C., Cauzid J. (2008): Rutile solubility in albite- H_2O and $Na_2Si_3O_7$ - H_2O at high temperatures and pressures by in-situ synchrotron radiation micro-XRF, *Earth and Planetary Science Letters*, 272, 730-737.
- McCulloch M. T., Gamble J. A. (1991): Geochemical and geodynamical constraints on subduction zone magmatism, *Earth and Planetary Science Letters*, 102, 358-374.
- McDonough W. F., Sun S.-S. (1995): The composition of the Earth, *Chemical Geology*, 120, 223-253.
- Münker C., Wörner G., Yogodzinski G., Churicova T. (2004): Behavior of high field strength elements in subduction zones: constraints from Kamchatka-Aleutian arc lavas, *Earth and Planetary Science Letters*, 224, 275-293.
- Newton R. C., and Manning C. E. (2000): Quartz solubility in concentrated aqueous NaCl solutions at deep crust-upper mantle metamorphic conditions: 2-15 kbar and 500-900 °C. *Geochimica et Cosmochimica Acta*, 64, 2993-3005.

- Newton R. C., Manning C. E. (2002): Solubility of silica in equilibrium with enstatite, forsterite, and H₂O at deep crust/upper mantle pressures and temperatures and an activity-concentration model for polymerization of aqueous silica, *Geochimica et Cosmochimica Acta*, 66, 4165-4176.
- Newton R. C., Manning, C. E. (2003): Activity coefficient and polymerization of aqueous silica at 800 °C, 12 kbar, from solubility measurements on SiO₂-buffering mineral assemblages, *Contributions to Mineralogy and Petrology*, 146, 135-143.
- Newton R. C., Manning C. E., Hanchar J. M., Colasanti C. V. (2010): Free energy of formation of zircon based on solubility measurements at high temperature and pressure. *American Mineralogist*, 95, 52-58.
- Newton, R. C., Manning, C. E., Hanchar, J. M., Finch, R. J. (2005): Free energy of formation of zircon from aqueous solubility measurements at high temperature and pressure, *Journal of the American Ceramic Society*, 88, 1854-1858.
- O'Neill H. St. C. (2006): Free energy of formation of zircon and hafnon, *American Mineralogist*, 91, 1134-1141.
- Pearce J. A., Stern R. J. (2006): The origin of back-arc basin magmas: trace element and isotope perspectives, *Geophysical Monograph Series, AGU*, 166, 63-86.
- Pearce J. A., Stern R. J., Bloomer S. H., Fryer P. (2005): Geochemical mapping of the Mariana arc-basin system: implication for the nature and distribution of subduction components, *Geochemistry, Geophysics, Geosystems*, 6, Q07006, doi:10.1029/2004GC000895.
- Pokrovski G. S., Schott J., Harrichoury J. C., Sergeev A. S. (1996): The stability of aluminum silicate complexes in acidic solutions from 25 to 150 °C, *Geochimica et Cosmochimica Acta*, 60, 2495-2501.
- Rapp J. F., Klemme S., Butler I. B., Harley S. L. (2010): Extremely high solubility of rutile in chloride and fluoride-bearing metamorphic fluids: An experimental investigation. *Geology*, 38, 323-326.
- Rüpke L. H., Morgan J. P., Hort M., Connolly J. A. D. (2004): Serpentine and the subduction zone water cycle, *Earth and Planetary Science Letters*, 223, 17-34.
- Sassi R., Harte B., Carswell D. A., Yujing H. (2000): Trace element distribution in Central Dabies eclogites, *Contributions to Mineralogy and Petrology*, 139, 298-315.
- Saul A., Wagner W. (1989): A fundamental equation for water covering the range from the melting line to 1273 K at pressures up to 25,000 MPa, *Journal of Physical and Chemical Reference Data*, 18, 1537– 1564.

- Saunders A.D., Tarney J., Weaver S.D. (1980): Transverse geochemical variations across the Antarctic peninsula: implications for the genesis of calc-alkaline magmas. *Earth and Planetary Science Letters*, 46, 344–360.
- Schmidt C., Rickers K., Wirth R., Nasdala L., Hanchar J. M. (2006): Low-temperature Zr mobility: an in-situ synchrotron-radiation XRF study of the effect of radiation damage in zircon on the element release in H₂O + HCl + SiO₂ fluids, *American Mineralogist*, 91, 1211-1215.
- Shen A. H., Bassett W. A., Chou I.-M. (1992): Hydrothermal studies in a diamond anvil cell: pressure determination using the equation of state, in: Y. Syono, M.H. Manghnani (Eds.), *High-pressure Research: Application to Earth and Planetary Sciences*, American Geophysical Union, Washington, pp. 616–68.
- Song S. G., Niu Y. L., Zhang L. F., Bucher K. (2009): The Luliangshan garnet peridotite massif of the Northern Qaidam UHPM belt, NW China – a review of its origin and metamorphic evolution, *Journal of Metamorphic Geology*, 27, 621-638.
- Stalder R., Foley S. F., Brey G. P., Horn I. (1998): Mineral aqueous fluid partitioning of trace elements at 900 °C-1200 °C and 3.0 GPa to 5.7 GPa: new experimental data set for garnet, clinopyroxene and rutile and implications for mantle metasomatism, *Geochimica et Cosmochimica Acta*, 62, 1781-1801.
- Tanaka H. (2000): Simple physical model of liquid water, *Journal of Chemical Physics*, 112, 799-809.
- Thirlwall M. F., Smith T. E., Graham A. M., Theodorou N., Hollings P., Davidson J. P., Arculus R. J. (1994): High field strength element anomalies in arc lavas: source or process? *Journal of Petrology*, 35, 819-838.
- Tropper P., Manning C. E. (2005): Very low solubility of rutile in H₂O at high pressure and temperature, and its implications for Ti mobility in subduction zones. *American Mineralogist*, 90, 502-505.
- Wagner W., Saul A., Pruss A. (1994): International equations for the pressure along the sublimation curve of ordinary water substance, *Journal of Physical and Chemical Reference Data*, 23, 515-525.
- Zheng J. P., Sun M., Griffin W. L., Zhou M. F., Zhao G. C., Robinson P., Tang H. Y., Zhang Z. H. (2008): Age and geochemistry of contrasting peridotite types in the Dabie UHP belt, eastern China: Petrogenetic and geodynamic implications, *Chemical Geology*, 247, 282-304.
- Zheng J. P., Griffin W. L., O'Reilly S. Y., Yang J. S.; Zhang, R. Y. (2006): A refractory mantle protolith in younger continental crust, east-central China: age and composition of zircon in the Sulu ultrahigh-pressure peridotite, *Geology*, 34, 705-508.

Zotov N., Keppler H. (2000): In-situ Raman spectra of dissolved silica species in aqueous fluids to 900 °C and 14 kbar, *American Mineralogist*, 85, 600-603.

5. General conclusions

Release of aqueous fluids from the subducting slab is a characteristic phenomenon and an important geochemical fingerprint of convergent plate boundaries. The fluids are produced by a number of dehydration and decarbonation reactions in metamorphosed oceanic sediments, altered oceanic crust, and serpentinized mantle peridotites. The role of aqueous fluids changes dramatically in relation to the geothermal regime of the slab; the fluid can be a solute-rich aqueous fluid or a hydrous silicate melt. These media differ in their transport properties and play distinct roles in metasomatism or partial melting in the mantle wedge. Halogens and trace elements show variable behavior in subduction zone settings due to their different incorporation mechanisms and partitioning between minerals, silicate melts and aqueous fluids. Consequently, the fluid composition and partitioning mechanisms directly affect the chemical composition of primary arc magmas. In order to better understand how mobility of common ligands and trace elements in aqueous fluids can affect the mantle wedge metasomatism and magma generation, I have investigated the behaviour of chlorine, fluorine and zirconium in aqueous fluids and nominally anhydrous minerals by experiments and molecular dynamic simulations.

Halogens δ fluorine and chlorine δ are incompatible in nominally anhydrous mantle minerals. However, their incorporation at trace level can substantially affect their Earth balance, cycles and fluxes between global geochemical reservoirs. In the oceanic lithosphere, halogens are dissolved in the pore fluid phase and incorporated in hydroxysilicates and -phosphates, which may break down during prograde metamorphism of the slab lithologies. The fate of halogens during metamorphic devolatilization reactions in the slab is, however, poorly understood.

This thesis addresses the following research questions: (1) what is the solubility of fluorine and chlorine in the nominally anhydrous mafic silicates in the upper mantle, (2) what is the energetics and impact on physical properties of fluorine incorporation in forsterite over wide range of temperature and pressure, and (3) what is the solubility of zirconium in aqueous fluids under subduction zone conditions?

I have performed piston-cylinder experiments at 1100 °C and 2.6 GPa to study the partitioning of fluorine and chlorine between forsterite, enstatite, pyrope, minerals of the humite group, and aqueous fluids. Major element and fluorine concentrations in the humite group minerals have been measured by electron microprobe, whereas the fluorine and chlorine abundances in forsterite, enstatite and pyrope were analyzed by the Cameca ims 6f SIMS instrument at the GeoForschungsZentrum Potsdam. In the absence of suitably characterized and

matrix-matched samples necessary for the calibration of the relative secondary ion yields, we have adopted ion implantation for the production of halogen standards. Fluorine can be incorporated in enstatite and pyrope to a maximum of 40 and 50 ppm, respectively. In contrast, forsterite dissolves more than 300 ppm F when equilibrated with an aqueous solution containing 1.6 wt. % F. At higher F concentrations in the system, humite group minerals are stable. Corresponding fluid-mineral partition coefficients for forsterite, enstatite and pyrope is 10^1 - 10^3 . The humite group minerals much more efficiently sequester fluorine from the aqueous solution (approximately by X orders of magnitude) due to its efficient substitution for the OH group in the crystal structure.

Chlorine is by a factor of two to three orders of magnitude more incompatible in nominally anhydrous silicates than fluorine. The chlorine solubility in pyrope, enstatite, and forsterite is less than 0.7 ppm, corresponding to the fluid-mineral partition coefficients of 10^3 - 10^6 . When the halogen solubilities in the mafic minerals are compared to that of hydroxyl, the behavior of F and OH is very similar in forsterite, enstatite and pyrope whereas Cl does not appear to be efficiently incorporated in the aluminosilicate crystal lattice by any common substitution mechanisms. The extreme incompatibility of chlorine in anhydrous minerals suggests that the Cl/H₂O of aqueous fluids or silicate melts can be used as a tracer of fluid-rock interaction and fluid transport styles in the mantle wedge. During percolation of aqueous fluids in the mantle wedge, H₂O and Cl exhibit different solubilities in the mafic phases, thus become decoupled, H₂O is more efficiently transferred from the fluid to the solid phases, and the salinity of the residual fluid phase builds up.

Using the initial salinity of the aqueous fluid released from the slab, estimated from global subduction fluxes of Cl and H₂O, I have formulated a simple mass balance model to predict evolution of the fluid salinity during progressive fluid interaction with a mantle peridotite. Calculations of H₂O and Cl mass balance were performed incrementally to simulate Rayleigh chromatographic exchange, and demonstrate that the rock-fluid ratios on the order of 10^3 are necessary to increase the fluid salinity, that is, the Cl/H₂O ratios, to the highest levels observed in primary arc magmas. Application of the transport theory reveals that this corresponds to a fluid migration path of up to 90 km in the subarc wedge, which is in agreement with pervasive fluid flow and extensive mantle wedge metasomatism.

The study of fluorine solubility in forsterite was extended by means of *ab initio* simulations to a wide range of pressures and temperatures. This approach allows us to better understand the incorporation of fluorine into the forsterite structure at the atomic level, and we retrieved the ground-state energetics and the pressure-volume relationships in order to construct a simple thermodynamic model to calculate solubility of fluorine in forsterite dictated by the humite-group mineral buffers. The incorporation mechanism considered in this work was the substitution of

fluorine for the silicate tetrahedron, $[F_4]^{4-} \leftrightarrow [SiO_4]^{4-}$. In the *ab initio* simulations, we utilized both the local density and general gradient approximations, and calculated the volumetric and thermodynamic properties of forsterite, sellaite (MgF_2), humite-group minerals (clinohumite, humite, chondrodite, norbergite) and of a set of solid solutions along the binary system Mg_2SiO_4 - Mg_2F_4 . The MgF_2 end-member with orthorhombic forsterite structure is by $24.2 \text{ kJ mol}^{-1} \text{ atom}^{-1}$ less stable than sellaite, and the humite-group phases are by 7.3 - $14.0 \text{ kJ mol}^{-1} \text{ atom}^{-1}$ more stable than the corresponding orthorhombic solid solutions in the system Mg_2SiO_4 - Mg_2F_4 . These results indicate that small amounts of fluorine can be dissolved in the forsterite structure, and this effect can be quantified by applying a suitable mixing model to equilibria of the type forsterite + $Mg_2F_4 \leftrightarrow$ humite-group mineral. The ground-state energetic properties revealed that the Mg_2SiO_4 - Mg_2F_4 solid solutions show a strong tendency to ordering at the $Mg_4[SiO_4 F_4]$ composition but only minor deviations from ideal mixing. Equilibrium calculations performed up to $1900 \text{ }^\circ\text{C}$ and 12 GPa indicate that the fluorine solubility in forsterite buffered by the most stable humite-group mineral strongly increases with temperature. At pressure of 2 GPa , the solubility is 0.007 ppm F at temperature of $500 \text{ }^\circ\text{C}$, but it rises to 2.9 wt. \% F at $1900 \text{ }^\circ\text{C}$. The pressure dependence is less pronounced, and the solubility slightly decreases with increasing pressure owing to the smaller unit cell volume of the humite group minerals in comparison with the Mg_2SiO_4 - Mg_2F_4 solid solutions with the orthorhombic forsterite structure.

The aqueous fluids released from the subducting slab and migrating through the mantle wedge experience element exchange with the surrounding lithologies of mantle peridotites and/or silicate melts. Potentially extensive interaction of aqueous fluids with the host rocks allows partitioning of trace elements; large ion lithophile elements, in contrast to high field strength elements, are fluid-mobile and preferentially enter the mantle wedge and its magma source regions. Consequently, the arc magmas have both a crustal or recycled trace-element fingerprint from the crustal slab component, and a mantle wedge signature resulting from the subsequent interaction of the aqueous fluids in the mantle wedge. Remarkably, the depletion in the high field strength elements is characteristic for the arc magmas worldwide, and it is attributed to very low solubility of these elements in the aqueous fluids when they are released from the subducting slab.

I have experimentally investigated the solubility of zirconium, as a representative of the high field strength elements, in aqueous fluids using the hydrothermal diamond anvil cell. Under the silica activity defined by the forsterite-enstatite buffer, zircon is the most stable Zr-bearing solid phase. Therefore, I have measured the zircon solubility in pure and solute-bearing aqueous fluid. Due to the presence of quartz in many eclogites, experiments were buffered by pure quartz, thus defining $a(SiO_2) = 1$. Zircon solubilities in H_2O are very low, ranging from 0.9 to 3.3 ppm Zr at

865-1025 °C and 6.22-19.99 kbar, and they weakly increase with temperature and pressure. When the activity of quartz is decreased to 0.363 (corresponding to the forsterite-enstatite buffer), the zircon solubility increases by a factor of two but still remains too low for any significant Zr transport from the slab to the mantle wedge to occur. These observations are consistent with the stability of zircon with respect to baddeleyite (ZrO_2) and quartz (SiO_2), and they exclude the formation of Zr-Si complexes in the fluid.

The presence of 15 wt. % NaCl in the fluid increases the zircon solubility to 4.5 ppm Zr at $a(\text{SiO}_2) = 1$, and an albitic solute has a similar effect. This behavior is consistent with the formation of zirconium-chloride and sodium zirconate and/or zirconium-aluminosilicate complexes, respectively. By evaluating the published solubilities of Si, Al and the high field strength elements, I demonstrate that their solubilities monotonously decrease with the increasing ionic radius of the cation. Furthermore, Zr, Hf, Ta, and Th all have solubilities that are not enhanced by complexing with silicate solute and thus remain very immobile in subduction zone fluids.

During slab dehydration, the Zr content in the aqueous fluid is predicted to be 1-2 ppm and mass balance calculations imply that the high field strength element concentrations in primary arc melts will slightly decrease due to the dilution effect of the infiltrating fluid. By contrast, mobile lithophile elements are predicted to increase their abundances in the melt by up to one order of magnitude. Thus, my results demonstrate that decoupling of large ion lithophile vs. high field strength elements in the arc magmas is related to different solubilities of these elements in aqueous fluids that migrate from the slab to the magma source regions.

Acknowledgements

All these years that I have spent at the Geoinstitut gave me rich knowledge and experience. I had opportunities to get to know people, to compare their opinions differ from mine, and to learn many things from those I worked or lived with. Sharing my time with people from this and other countries allowed me to consider diversity as a value. It also helped me understand that diverse habits, ways of thinking or behavior of others are neither better nor worse than mine, for they are simply different, and they have to be understood and respected. This finding is as valuable for me as the academic knowledge and experience that I have gained in Bayreuth.

During my Ph.D. studies I have benefitted from experience and advice of many people at the institute. My thanks go to David Dolej-, Nico de Koker, Andreas Audétat, and Professor Hans Keppler. A particular thank-you goes to David, who taught and guided me step by step during the whole Ph.D. project. I was materially supported by the EU Marie Curie network by the "Atomic to Global" fellowship, administered by Catherine McCammon, for the first 2 years and 8 months, and from DFG for the following four months. I am happy to acknowledge the help of institute secretaries ó Lydia Kison-Herzing and Petra Buchert, computer and microprobe technician ó Detlef Krausse as well as the invaluable help of preparators ó Hubert Schulze and Uwe Dittmann and the technician Sven Linhardt. No less important were all the friends with whom I had fun and shared my time.

Un ringraziamento particolare va al mio gruppetto di italiani del BGI, con cui abbiamo discusso di qualunque cosa, dal lavoro alla politica, passando dall'immancabile cucina italiana, sempre con allegria. Il mio grazie dunque va a Davide Novella e a Martha Pamato (grazie mille per tutte la volte che mi avete ospitato a cena in questi anni, è stato davvero un piacere per me), a Vincenzo Stagno e Paola Valenti, a Federica Schiavi, al mio compagno d'ufficio Mattia Giannini, a Valerio Cerantola e Giacomo Pesce, a Micaela Longo, ed anche a Marco Mantovani, Carmen Capalbo, Andrea Fortunati e Giacomo Lo Nigro, che pur avendo trascorso meno tempo con loro mi hanno lasciato comunque un buon ricordo.

I would like to extend my thanks to Julien Chantel, with whom I shared a lot of good time both in and out of Bayreuth, Linda Lerchbaumer, and to Vojtěch (Vojta) Vlček, Alberto Escudero, Shantanu Keshav(ski), Konstantin Glazyrin, Vladislav (Vlady) Aleksandrov and Geertje Ganskow; they are all thanked for the good beer times and fun we had. I appreciate joint dinners with Florent Jochaud and all interesting exchanges of opinions about almost everything.

I also thank to all the people that helped me by talking, explaining, and exchanging opinions. Grazie a Tiziana Boffa Ballaran per avermi aiutato e dato consigli quando avevo dubbi in tutti questi anni. Thanks also to Mainak Mookherjee with whom I had interesting discussions about science and received many good suggestions, to Enikö Bali for her kindness to introduce me to piston cylinder and capsule welding methods. Last but not least I appreciate Gerd Steinle-Neumann who allowed me to use the BGI cluster.

Un ringraziamento particolare va anche a tutti quelli che benché lontani mi hanno aiutato sostenuto e fatto sentire comunque un po' sempre a casa in tutti questi anni. Grazie dunque alla mia famiglia (tutta) ed a quella di Alessandra. Grazie anche al Biste che mi è venuto a trovare, grazie mille anche a Tato, e a tutti quelli che comunque si sono tenuti in contatto con me nonostante sia partito.

Infine un ringraziamento particolare, il più importante, va alla mia fidanzata Alessandra Spingardi, la persona che in tutti i tanti momenti di difficoltà che ho avuto in questi anni mi ha aiutato, ascoltato, capito, corretto, consigliato, calciato, strigliato. Grazie davvero.

Hiermit erkläre ich, dass ich die Arbeit selbständig verfasst und keine anderen als die von mir angegebenen Quellen und Hilfsmittel benutzt habe.

Ferner erkläre ich, dass ich anderweitig mit oder ohne Erfolg nicht versucht habe, diese Dissertation einzureichen. Ich habe keine Doktorprüfung an einer anderen Hochschule endgültig nicht bestanden.

Bayreuth, am 8. März 2011

A handwritten signature in blue ink, consisting of two distinct parts. The first part is a stylized, cursive letter 'D' with a long horizontal stroke extending to the right. The second part is a more complex, cursive signature that starts with a vertical stroke, loops back, and ends with a long horizontal stroke extending to the right.